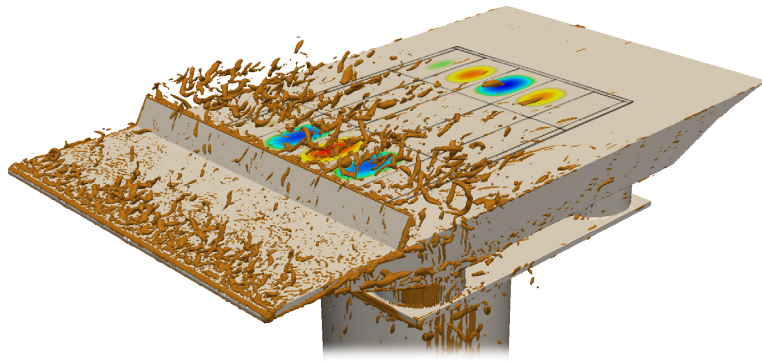# NUMERICAL METHODS FOR LOAD AND RESPONSE PREDICTION FOR USE IN ACOUSTIC FATIGUE

JOHAN NILSSON

Structural Mechanics

Doctoral Thesis

NUMERICAL METHODS FOR LOAD AND RESPONSE PREDICTION FOR USE IN ACOUSTIC FATIGUE

JOHAN NILSSON

Acknowledgements

<div align="right">

Lund, May 2016
Johan Nilsson

</div>

Abstract

Acoustic fatigue can occur in structural elements of an aircraft exposed to very high sound pressures. To deal with acoustic fatigue, mainly empirical methods have been applied and often late in the design phase. Current design guidelines have three main limitations. First, they do not say anything about the load intensities. The load levels can be determined either experimentally or numerically. Experimental testing tends to be expensive and time consuming. It is also desired to deal with acoustic fatigue early in the design phase. Therefore, it is desired to turn to numerical methods to determine the load levels. Second, the design guidelines assume that the spatial distribution of the load is uniform. In other words, the load is assumed to be perfectly in phase over the entire structural element. This assumption limits the accuracy of the response prediction and by extension the fatigue prediction. Third, the design guidelines are limited to a simple, single surface panel with linear response.

In this thesis, both the load and response prediction are performed by numerical methods. The load is determined using Computational Fluid Dynamics (CFD). From the CFD simulations, both the load intensities and the spatial distributions are extracted. This solves the first and second mentioned limitations. The extracted load is used as force input to a Finite Element (FE) simulation of the exposed panel structure. Since complex structures and non-linearities can be handled using the FE-method, it avoids the third mentioned limitation.

Two cases of separated flow are used as model problems for acoustic fatigue in this thesis. In both model problems, the simulations are compared to existing measurements. In Paper A, a ramped backward-facing step is used. The flow over the step induces a load on an aluminium sheet fitted downstream of the step. With the exception of the cut-off, or shedding mode, frequency being overpredicted, the spectral qualities of the load and the load intensities are well captured. The panel response prediction compares reasonably well with the existing measurements. In Paper B, a reduction in a range of low frequencies of the downstream load is observed when the ramped backward-facing step is lined with chevrons or serrations.

The model problem used in Papers C–E is flow over an inclined fence at transonic Mach number and realistic Reynolds number for aircraft operation. A segment with cyclic boundary conditions of the flow setup is simulated in Paper C. This result in well predicted cross-spectra, but an energy concentration in the auto-spectra is not properly resolved. In Paper D, a full three-dimensional simulation of the entire setup is performed and it is concluded that the missing energy concentration in the auto-spectra is properly captured. In Paper E, the response of a realistic aircraft panel structure is simulated using FE random response analysis with the CFD-simulated load as input. The response is found to be sensitive to the cross-spectra of the input load. The strain predictions vary with strain gauge location. However, only one strain gauge is off by more than a factor of two, which appears to be the best one can hope for when using the design guidelines in favourable conditions and with a measured load. Therefore, the main conclusion of this thesis is that the method of using CFD to calculate the load which is to be used as input to an FE response simulation can produce useful results for acoustic fatigue.

Populärvetenskaplig sammanfattning

Akustisk utmattning undersöks främst genom dyra och tidskrävande provflygningar och andra experimentella metoder. Genom att använda numeriska metoder för både last- och vibrationsuppskattningar finns god potential till att spara både tid och resurser vid flygplansutveckling.

Akustisk utmattning är ett problem för flygplansindustrin. Problemet orsakas av mycket höga ljudnivåer vid utsidan av flygplan, rymdraketer och andra liknande farkoster. Jetmotorn är en typisk ljudkälla, men även klaffar, kaviteter (hålighet på utsidan av flygplanet) och strukturer monterade på utsidan av flygplanet kan orsaka höga ljudnivåer. Eftersom ljud i själva verket är pulserande tryck, kan de strukturer som utsätts för höga ljudnivåer börja vibrera. Dessa vibrationer kan orsaka sprickor som sedan växer. Om detta får fortgå obehindrat kan strukturen till sist helt enkelt skaka sönder.

Det är därför av stor vikt att känna till vilka intensiteter och vilka egenskaper denna last har som flygplansstrukturen utsätts för. Traditionellt används främst experimentella metoder för att bestämma detta, såsom mätningar vid provflygningar eller i vindtunnlar. Problemet med dessa metoder är att de är dyra och är möjliga först sent i designprocessen. I den här avhandlingen används istället en numerisk metod som kallas CFD (Computational Fluid Dynamics) för att simulera lastens intensitet och egenskaper. CFD-simuleringar är vanligt förekommande och ett väl etablerat verktyg i andra områden inom flygplansutveckling, men används i mindre utsträckning när man designar för akustisk utmattning.

Det finns flera sätt att bestämma vibrationsnivåerna till en given last när man designar för akustisk utmattning. Man kan använda experimentella metoder (t.ex. högtalare, sirener m.m.). Det finns även handboksmetoder för akustisk utmattning som brukar användas. Dessa handboksmetoder är baserade på några förenklande antaganden som begränsar deras noggrannhet. Om CFD används för att bestämma lastnivåerna och lastegenskaperna kan man istället utnyttja dessa i en numerisk simulering av strukturen som utsätts för lasten med hjälp av finita element metoden. Finita element metoden (FEM) är väl etablerad inom flygindustrin för att bestämma flygplansstrukturers egenskaper. Den kan t.ex. användas tillsammans med handboksmetoderna för akustisk utmattning. Genom att använda CFD för att bestämma lasten och dess egenskaper och applicera dessa direkt på finita element modellen av strukturen behöver man inte göra de förenklingar som handboksmetoderna gör och på så vis uppnå en högre precision i predikteringen av akustisk utmattning.

I den här avhandlingen beräknas lasten med hjälp av CFD och responsen med hjälp av FEM på två olika fall där simuleringarna jämförs med befintliga mätningar. För att CFD-simuleringarna ska stämma väl överens med verkligheten krävs att många detaljer fångas upp på ett riktigt sätt i simuleringen. Det är en utmaning eftersom det skulle krävas för stora datorresurser om man skulle ta med alla detaljer i CFD-simuleringarna. Men resultaten i denna avhandling visar på att det är möjligt att ta fram användbara last- och vibrationsuppskattningar med den här metodiken, vilket är huvudmålet med avhandlingen.

Contents

Paper A
Load and response prediction using numerical methods in acoustic fatigue.
Johan Nilsson, Robert-Zoltán Szász, Per-Erik Austrell, Ephraim J. Gutmark.
Published in the Journal of Aircraft, **53**(2), 406–415, (2016).
doi: 10.2514/1.C033414

Paper B
Passive load control in backward-facing step flow by using chevrons.
Johan Nilsson, Robert-Zoltán Szász, Per-Erik Austrell, Ephraim J. Gutmark.
Accepted for publication in: Segalini, A. (ed.), *Proceedings of the 5th International Conference on Jets, Wakes and Separated Flows (ICJWSF2015)*, (2016).
ISBN: 978-3-319-30600-1

Paper C
Numerical simulation of surface pressure fluctuations in transonic fence-like flows with high Reynolds number.
Johan Nilsson, Robert-Zoltán Szász, Per-Erik Austrell, Delphine Bard.
Published in the International Journal of Heat and Fluid Flow, **58**, 103–119, (2016).
doi: 10.1016/j.ijheatfluidflow.2015.12.008

Paper D
Three-dimensional aspects of fence flow.
Johan Nilsson, Robert-Zoltán Szász.
Submitted for publication.

Paper E
Numerical response simulation of a panel structure exposed to a numerically simulated load from separated flow.
Johan Nilsson, Per-Erik Austrell, Robert-Zoltán Szász.
Submitted for publication.

Part I

Introduction and overview

1 Introduction

ACOUSTIC FATIGUE, also known as sonic fatigue, is a problem for the aircraft industry. Structural elements, such as skin surface panels, on aircraft may be exposed to high intensity sound levels. These high sound levels may cause the structural element to vibrate, simply because sound is pressure fluctuations. This means that the high sound intensities act as a fluctuating force loading on the structural element. The vibration may lead to cracks in the structural element and already existing cracks may grow. If this vibration is allowed to go on unchecked it may eventually lead to failure. The vibrational frequencies involved tend to be in the order of hundreds of Hz. Acoustic fatigue can therefore develop quickly as it does not take a long time before a large number of cycles have passed.

There are several possible sources for this high intensity load. The perhaps most obvious source is noise from the jet engine or the propeller. But there is also the case where geometrical features cause strong loads. These may be control surfaces, flaps and cavities. All these geometrical features include separated flow and periodic vortex shedding as key features.

Acoustic fatigue is a problem in several ways. Obviously, aircraft suffering from failure in flight can have drastic consequences. Keeping cracks under control is therefore important. During maintenance the aircraft can be tested for cracks, but not all parts of the aircraft can easily be tested. Frequent maintenance requirements are undesired for economic reasons.

Traditionally, acoustic fatigue has been dealt with using empirical methods. Design guidelines have been developed and are applied. An example of this is the ESDU design guidelines on acoustic fatigue [1]. The current design guidelines have three main limitations:

1. The load levels at the eigenfrequencies of the panel structure must be known.
2. The load is assumed to be fully in phase over the exposed structure, or in other words, the load is assumed to have a uniform spatial distribution.
3. The design guidelines are limited to a simple surface panel with linear response.

The first limitation can arguably be said to be outside the scope of the design guideline and not being a limitation to the guidelines per se. However, the load levels are often determined experimentally. Finding the load levels experimentally from the use of wind-tunnels or flight

testing is expensive. It is also desired to handle acoustic fatigue early in the design phase before any flight testing can be done. It is much cheaper to deal with an issue early on compared to when the aircraft has gone to flight testing. The second limitation reduces the accuracy of the response prediction of the structure which in turn reduces the accuracy of the fatigue prediction. The response prediction has been shown to improve significantly if a more realistic load distribution is applied [2, 3]. The third limitation restricts the guidelines to certain structures. For example, composite panels can have large non-linear response which is not covered by the design guidelines.

For the reasons mentioned above, it is desired to use numerical simulations to predict acoustic fatigue. When it comes to determining the dynamical properties of the aircraft structures, the Finite Element Method (FEM) has been in heavy use for some time now. This avoids the third limitation with design guidelines given above. However, the determination of the load levels and their spatial and temporal characteristics using numerical methods appears to have been less dealt with. This is the domain of Computational Fluid Dynamics (CFD). Most, if not all, of the typical load sources have been studied with CFD. There are many CFD studies on engine noise, cavities etc. Usually, the concern has been on what noise they make or aspects unrelated to acoustic fatigue. Studying noise sources is an important application of CFD within the subject of acoustic fatigue. In other words, while accurate fatigue predictions are desirable, removing the source is much better. It can also be used to address limitation number one in the list above. However, attempts to study the intensities *and* the spatial distribution of the pressure fluctuations on the exposed surfaces directly as a tool for making fatigue predicition is often not attempted. The scope of the thesis is limited to the important cases of loads caused by separated flows. This excludes all loads that appear in the far field. For separated flows, there are few numerical studies on the surface pressure fluctuations [4, 5]. Those that exist are performed on Reynolds numbers far below realistic ones for aircraft operations. Also, they do not make the step to do a response prediction of the exposed surface.

1.1 AIM AND OBJECTIVE

The general aim of this thesis is to improve the load and response prediction for acoustic fatigue by attempting to use numerical methods in the form of CFD to predict the load. It is desired to capture both the load levels and the spatial distribution of the load as both are important parameters that have good potential to improve the response predictions. Knowledge of what is required of the numerical method to produce an accurate load prediction is naturally sought. It is desired to have the numerical method tested in conditions that are relevant to the aircraft industry.

The numerical method is applied to two model problems dealing with separated flow. The main innovation in this thesis is that CFD is used to directly derive the surface pressure load. A majority of the thesis is therefore spent dealing with CFD analysis. However, the end goal

of this thesis is to produce a response prediction in the exposed structure. In Papers A and E, the calculated load is applied to an FE response simulation of the exposed structure in order to reach this goal.

It should also be mentioned, that while the aim of this thesis is on acoustic fatigue, the work here should be of interest for efforts to reduce the noise inside the cabin as well. The sound pressure levels discussed are high and the vibration of the outer skin surface panels are clearly a transmission path. Although cabin noise reduction is not directly inside the scope of this thesis, it should be noted that this work may be beneficial in other contexts as well.

1.2 OUTLINE

This thesis is organised in two parts. The second part consists of five research papers that have been produced in this project. These papers are preceded by an extended introduction and overview of the work. It also contains a more thorough treatment of topics that are treated in less detail in the papers. Chapter 2 is a literature review on acoustic fatigue. In Chapter 3, the motion of fluids is discussed. This includes a phenomenological discussion of turbulent flow, the numerical treatment as well as an introduction to flow types dealt with in this thesis. In addition, a post-processing technique called Proper Orthogonal Decomposition (POD) is described as well. The FE method used to perform response predictions of the exposed structures is covered in Chapter 4. The FE formulation used in Paper E, random response analysis, is based on stationary stochastic processes. Therefore a brief introduction to such processes are also given in Chapter 4. However, concepts from stationary stochastic processes are used when analysing data throughout the entire thesis. Chapter 5 contains a summary of the appended papers. Finally, a summary of this thesis contributions, some conclusions and suggestions for future work are given in Chapter 6.

2 Acoustic fatigue

I N THE EARLY FIFTIES, acoustic fatigue (also known as sonic fatigue) related incidents increased on new jet engined aircraft. This led to a range of experimental studies at several aircraft companies. Since the failures were frequently located near jet engine exhausts, actual aircraft jet engines were often used to provide realistic acoustic excitation on single panel studies, as well as large parts of aircraft structures. This eventually lead to the development of analytical methods and design guidelines [6, 7]. These methods are described in Section 2.1. Even though the power of the engines kept increasing throughout the sixties and seventies, the sound pressure levels were not. The reason for this is the development of high-bypass turbofan engines in order to reduce engine noise near airports. The lack of increase in pressure levels together with the now established design guidelines reduced interest in research and development on acoustic fatigue. However, the introduction of composites in aircraft skin panels in the mid eighties and nineties spured new interest in the subject. The composite panels can feature large displacements taking the response into the non-linear region, thus creating new challenges [6, 7]. The research related to composite panels is covered in Section 2.2. Two studies giving important attention to the spatial distribution of the load are covered in Section 2.3. Finally, Section 2.4 provides some discussion of the literature on acoustic fatigue and how it relates to the work performed in this thesis.

2.1 ANALYTICAL METHODS AND DESIGN GUIDELINES

The first method for response prediction of an acoustically excited metallic structure was developed by Miles [8]. In his study, the skin panel structure was modelled by a single rectangular thin linear-elastic plate. Furthermore, only the response in the fundamental mode was considered, thus turning the model into a single degree-of-freedom system. The load was assumed to be uniform, or in-phase, over the whole plate with a spectral density $G_p(f_n)$ at the frequency of the fundamental mode f_n. From these assumptions, Miles derived the following expression for the mean square stresses for the plate

$$\overline{\sigma^2(t)} = \frac{\pi}{4\zeta} f_n G_p(f_n) \frac{\sigma_0^2}{F_0^2}, \tag{2.1}$$

where σ_0 is the static stress at the point of interest due to a uniformly distributed force F_0 and ζ is the viscous damping ratio. To estimate the fatigue life of the panel Miles used Miner's cumulative damage hypothesis [9].

Powell [10] took this one step further by considering multiple modes via the normal mode approach. The modes of the plate subjected to the random pressure load were assumed to be uncoupled. This is true if the displacements are small and the structure is lightly damped, as is typically the case for metallic aircraft skin structures. The response can then be given as summation of the responses in each mode. In addition, he also introduced the concept of "joint acceptance", which is a measure of the effectiveness of the pressure field to excite a particular mode.

Later, Clarkson [11] took Powell's work and suggested a simplification of it in order to develop a relatively simple formulation which could be used in the design of aircraft skin panels. Clarkson showed that if it is assumed that the response is dominated by one mode and the excitation pressures at that mode are in-phase over the whole plate, then the result reduces to Miles' equation (2.1), which is still used today as a design tool for structures subjected to random pressure loading. By also assuming that the plate had fully fixed boundary conditions, he proposed a series of steps to be used as a design process.

The IHS ESDU (previously Information Handling Services and Engineering Sciences Data Unit, respectively) provides design guidelines and design data in many different fields such as, aerospace engineering, process engineering and structural engineering. Among these, they provide a series on vibration and acoustic fatigue which includes [1] based on the studies presented in this section. Another design guideline based on the same approach is the AGARD method [12]. Furthermore, there is also an extensive text called "Sonic fatigue design guide for military aircraft" [13] on the subject compiled by the Acoustics & Vibration Associates for the US Air Force. It is the result from a review of over 300 references related to acoustic fatigue containing many tables, charts, nomographs, computer programs and worked examples.

Blevins [14] extended Miles' and Clarkson's method to several modes. He also used the concept of joint acceptance which he used when he studied how different spatial distributions of the acoustical load affected the response of the structure. He did not use an exactly known load distribution but looked at a few different approximations, e.g. a sinusoidal load or a load which has the same spatial distribution as the (mass weighted) structural mode. He compared the latter approximation with AGARD's guidelines for a simple rectangular plate and got almost the same result. To determine the mode shapes and the eigenfrequencies of the plate, which is input to the method, he used the FE-software MSC/NASTRAN. He also compared experimental data from a different plate tested in a Progressive Wave Tube (PWT). A PWT is essentially a very powerful loudspeaker/siren which can deliver very high sound levels, some-
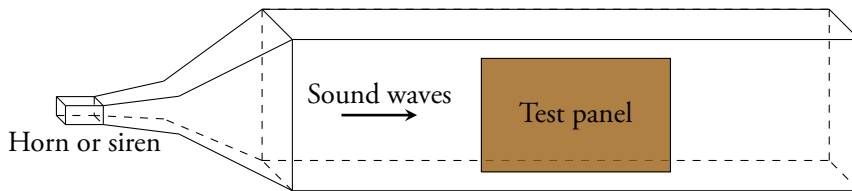
Figure 2.1: Basic layout of a Progressive Wave Tube (PWT) test rig.

times up in the region of 165 dB. The sound is then directed through a tube passing over the sample. A typical setup is illustrated in Figure 2.1. The sample is placed so that the sound waves pass over the surface of the sample which is placed on one side of the tube. Blevins found the results from the model higher than the experimental values, but within the margin of experimental error. While Blevins' work tries to take the spatial distribution of the load into account, it still requires that some spatial properties of the load is known as well as the load intensity and spectral properties.

2.2 NON-LINEAR BEHAVIOUR

The methods in Section 2.1 were developed with metallic structures in mind and not composites being common in aircraft today. One of the first studies on the response of composites was made by White [15]. He compared measurements of the response of an aluminium plate and a plate made of a carbon fibre composite (CFRP — Carbon Fibre Reinforced Plastic) in a PWT. The CFRP panel exhibited a high degree of non-linearity. For very high sound intensities this was also true for the aluminium panel, but the non-linearities were much lower. As an example, the first eigenfrequency increased 100 % when the excitation increased from 130 dB to 154 dB for the CFRP panel, but for the aluminium panel the corresponding change was only 35 %. The methods described in Section 2.1 use the assumption that the panel response is dominated by one or a few modes. The non-linearities present at high excitation levels in the CFRP panel caused only 65 % of the mean square strain to be from the resonance peaks, compared to 90 % for the aluminium plate. Therefore, the methods in Section 2.1 cannot give an accurate prediction of the tested CFRP panel response. In addition to the frequency shift of the resonance peaks, the peaks also broaden. As these two behaviours are typical for increased damping, it was initially suggested that non-linear damping played an important part in the observed non-linearities [16]. However, later it was demonstrated by Reinhall and Miles that the broadening and phase shifts could be observed without any non-linear damping [17]. They found the dominant non-linearity to be the increased in-plane stiffness due to the large deflections as accounted for in the von Kármán theory. This increased stiffness is proportional to the cube of the displacements.

Using FE simulations is one way to treat the described geometric non-linear behaviour. However, the computational resources needed to do this directly for a full model in the time domain

is very large [18]. Therefore, it is desired to use some form of Reduced Order Modelling (ROM) to lessen the computational burden. A comparison of ROM methods to deal with geometrical non-linearities for acoustic fatigue response prediction can be found in [19]. For hypersonic vehicles thermal loads must also be taken into consideration. A good example of this is the case study found in [20]. Thermal loads can create in-plane stresses causing thermal buckling or snap-through. This makes the analysis more complex as fluid-thermal-structure coupling must be considered [21]. A recent review for ROM that also covers thermal loads and has a focus on using commercial FE-software is found in [22].

2.3 STUDIES ON THE IMPACT OF THE SPATIAL DISTRIBUTION

Cunningham and White [23] and Cunningham et al. [3] performed experimental and numerical studies on how doubly curved rectangular composite plates behave in a PWT. This study is given a more detailed coverage as some of their key findings relates to some of the fundamental ideas of this thesis. In their study, they applied single degree-of-freedom models (as described in Section 2.1), Blevins [14] method (see Section 2.1) and an FE-analysis, in order to predict the panel response. The mode that was excited the most in the experiment was chosen for the single degree-of-freedom model, which in neither plate was the fundamental mode. The actual mode shape used was produced in an FE-analysis.

As excitation to the single degree-of-freedom model, three different spatial distributions of the sound pressure field were used. Case 1: Uniform distribution over the whole plate (essentially as Miles [8] and Clarkson [11]). Case 2: The distribution matches that of the excited mode (similar to the assumption tested by Blevins [14]). Case 3: The pressure field forms a sound wave which propagates over the plate with the measured propagation velocity. The different pressure field distributions were applied by computing the joint acceptance. In the first case the response is severely underpredicted. This is due to the fact that a pressure field in phase over the whole plate excites mainly the fundamental mode and excites the higher modes very little, including the one chosen for the model, which gives small strains. They concluded that the problem is not that the wrong mode had been selected, but rather that the actual pressure distribution is very different from the applied pressure distribution. The assumption of uniform pressure distribution is applicable when the acoustical wave length is considerably longer than the plate, which apparently was not the case. In case 2, the response is overpredicted. In this case the pressure distribution gives the joint acceptance equal to 1, which means that the distribution excites the structure at that mode with maximum efficiency. A perfectly matching spatial distribution is in practice unlikely, but maybe case 2 can be seen as a worst case scenario. The approximation of the pressure distribution used in case 3 gave the best prediction and is believed to be a good approximation of the actual one.
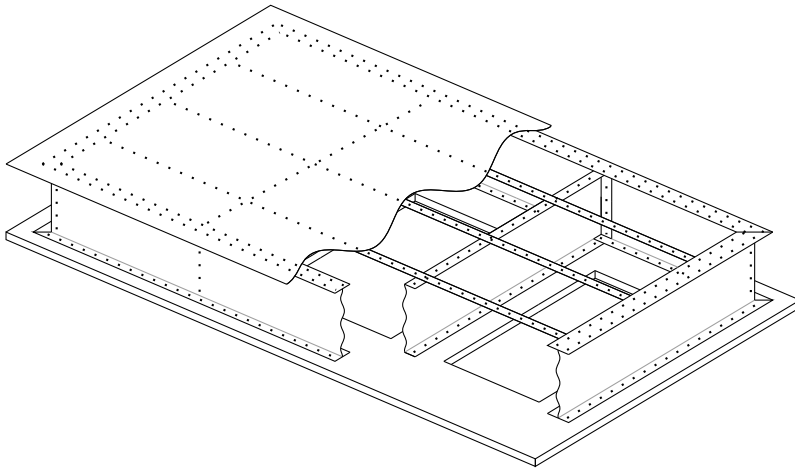
Figure 2.2: Basic panel design.

When Cunningham et al. [3] tried Blevins method [14] they got similar results as the single degree model for the three different load cases. The third method they tried was an FE-analysis with ANSYS. They used a harmonic solution method where the load was once again simulated as a wave propagating across the plate for each frequency. The FEA underpredicted the r.m.s. strains slightly but was most often within 30 % from the measured values. The result can be compared to the design guidelines which are able to predict the strains only to a factor of two compared to measurements [6]. This illustrates that there is a great potential for improvements if the spatial distribution of the load is taken into consideration.

From the September 1st, 1990 to February 28th, 1993 a large EU financed project within the Brite-Euram programme called ACOUFAT, "Acoustic fatigue and related damage tolerance of advanced composite and metallic structures", was carried out. The project involved many of the major European aircraft manufacturers, related contractors, universities and research institutes. Reference [24] contains the final report, which is also published as part of a book [25].

Several different type of activities were carried out in the ACOUFAT project. The first activity was material testing of two metal-alloys and three composite materials. Second, five panel structures of different materials (both metallic and composite) were manufactured. These panels were the subject of modal tests, linearity checks, PWT-testing and FE-modelling. They were designed to be representative of an outer skin-panel of an aircraft. They had a thin upper plate on top of a stringers and ribs arrangement with a thicker lower plate at the bottom for structural rigidity. The lower, thick, plate had cut-outs in each bay to avoid cavity effects and low frequency modes of the total box. Figure 2.2 illustrates the basic design.

The third activity of the ACOUFAT project was a wind-tunnel testing campaign. An aluminium skin panel with a basic design similar to the one shown in Figure 2.2 was flush mounted on a table just downstream of a fence in a wind-tunnel as illustrated in Figure 2.3. As the

Figure 2.3: Test setup of the wind tunnel table.

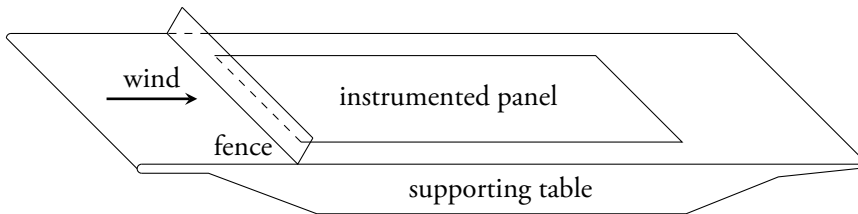flow is deflected by the fence, it separates and induces a pressure load on the panel. This type of flow is discussed in Section 3.2. The load was measured as well as the panel response to the load. The panel structure used in the wind-tunnel testing was then also tested in two different PWT:s for comparison. The excitation spectrum used in the PWT was formed to match the spectrum measured in the wind-tunnel test. The purpose of performing this comparison was to investigate to what extent PWT testing is representative of more realistic flight conditions. In addition, an attempt to model the load analytically was done by Campos [2,26]. He developed a semi-empirical model of the correlation of the acoustic load between different points on the panel. Finally, Campos' model, as well as measured loads from both the wind-tunnel and the PWT measurements, were applied to an FE-model of the panel simulating the response of the panel in order to determine the effectiveness of Campos' model. The details of this part of the ACOUFAT project is found in several reports internal to the project [26–30]. In addition, a journal article by Campos et al. [2] includes the semi-empirical model and its application to the FE-simulation of the panel response, as well as the wind-tunnel and PWT-testing comparison.

The main findings from the wind-tunnel and PWT-testing comparison are related to the spatial correlation of the load and its influence on the panel response. In the PWT measurements, the cross-spectra were found to be high, meaning that the acoustic field was nearly fully in phase over the whole panel. In contrast, the wind-tunnel measurements indicated a much lower cross-spectra between different points on the panel. A second difference was found in the load spectrum in the PWTs. The load spectrum was shaped to match the fairly smooth wind-tunnel spectrum measurements. However, the measured pressure load spectrum on the panel in the PWTs were rather peaky. These peaks were likely caused by standing waves associated with the inner dimensions of the wave tube.

The measured panel response was found to be different in the PWTs compared to the response measuered in the wind-tunnel. In the wind-tunnel, mainly the anti-symmetrical modes were excited with a symmetry line taken at the centre-line in the streamwise direction. The opposite was found in the PWTs; there the symmetrical modes were the ones that were excited. The FE-simulation of the panel response was performed in the frequency domain with the auto-spectra shaped as the wind-tunnel measurements. In order to investigate the influence of the load cross-spectra on the panel response, a parameter study was performed where the normalised cross-spectra was varied between 0 and 1 with the same cross-spectra over the whole panel. For low

values of the cross-spectra, the response was similar to that in the wind-tunnel measurements; mainly anti-symmetrical modes were excited. On the other hand, a high cross-spectra would excite mainly the symmetrical modes. Also, when applying the measured cross-spectra from the wind-tunnel, a similar response to the wind-tunnel measurements appeared.

The analytical, or semi-empirical, model of the spatial correlations of the wind-tunnel load by Campos is described in [2] and [26]. The model uses sophisticated concepts of maths and statistics. It is based on the idea that the turbulent wake (the shear layer) emits sound that may be decomposed into plane waves. These waves may then reflect against the panel surface and against the wake itself. Since the wake is turbulent, it has an irregular shape. This irregularity means that the distance a sound wave emitted from the wake has to travel in order to reach the panel surface differs from different points in time and space. This causes random phase shifts, which are considered in the model as well. The model requires no less than eight parameters to be given. These are:

1. Double reflection coefficient.
2. Excitation frequency (this is a strong tonal frequency found in the wind tunnel load).
3. Longitudinal excitation wavenumber.
4. Transverse excitation wavenumber.
5. Root mean square phase shift.
6. Longitudinal correlation scale.
7. Transversal correlation scale.
8. Correlation time.

The spatial correlation predicted by the model corresponds well to the wind-tunnel measurements on some microphone pairs, and worse on others. Nevertheless, when the model is used as input to the FE-simulation of the panel response, the response is predicted remarkably well.

From the wind-tunnel and PWT comparison, as well as the semi-empirical modelling, the following conclusions were drawn in the ACOUFAT project: PWT testing cannot reproduce the wind-tunnel loads by merely correctly shaping the auto-spectral contents of the load. The panel response in the PWT is different from the response in the wind-tunnel; in the PWT symmetrical modes are excited, while in the wind-tunnel anti-symmetrical modes are excited. This is important since it could lead to different modes of failure in the PWT-testing as opposed to actual flight conditions. From the correlation parameter study using FE-simulations, the conclusion was that the key load parameter determining which modes of the panel that will be excited, is the spatial correlation, i.e. the cross-correlation spectra. As the FE-modelling of the panel response was successful when the correct load characteristics (including cross-correlation spectra) were used, either from measurements or the semi-empirical model, this is not really a new structural phenomenon, but merely a matter of obtaining the right loads.

2.4 DISCUSSION

As the preceding sections of this chapter indicate: a good load specification is essential for a good response prediction of the skin panels. In the early methods covered in Section 2.1, that are still used in up to date design guidelines [1], the main formula used (which is similar to equation (2.1)), relies on the information of the load level ($G_p(f_n)$) at a given frequency (f_n). This must by some means be determined. The great improvements to the response prediction that the consideration of the spatial distribution of the load can give is well illustrated by both the studies by Cunningham et al. [3, 23] and the ACOUFAT project (Section 2.3). Interestingly, the ACOUFAT study finds that when modelling PWT tests numerically, the cross-correlation of the load should be close to one, meaning the load should be considered to be nearly in phase over the whole panel. On the other hand, Cunningham et al. [3] finds that in order to improve the numerical response prediction of a PWT test, one should not consider the load to be in phase, but rather as wave travelling over the panel. There are, however, some differences between the investigations. The ACOUFAT project focused on the difference between PWT testing and the more realistic conditions found in a wind tunnel, rather than seeking to improve the response prediction in a PWT test. Nevertheless, both investigations underline the importance of the spatial distribution of the load.

To use any method described so far in this chapter, the user must know the load levels (and preferably, the spatial distribution of the load as well). The most obvious way is perhaps to make an actual flight test and measure it. While testing for acoustic fatigue in the most realistic conditions should give the best results, it is desired to avoid this for several reasons. First, the flight tests themselves are expensive and time consuming. Instruments must be fitted and a process of proving air-worthiness may need to be performed (as a result of fitting instruments) before the aircraft can even leave the ground. Second, flight testing a complete aircraft is only possible late in the design process. At this stage many design choices may be fixed and changes can be costly. Therefore it is desired to consider acoustic fatigue early in the design process. Wind-tunnel testing is also expensive and time consuming, but clearly an option. Analytical modelling was also investigated by Campos (as described above) [2]. Despite the fact that the FE-simulations predicted the panel response remarkably well when Campos' model was used, it still requires many parameters to be determined by some means. Since the parameters still need to measured or estimated, the approach is considered to have the same issues as the experimental methods.

Rather than using experimental methods to determine the load, it is desired to turn to numerical methods. This is what is attempted in this thesis, via the use of Computational Fluid Dynamics (CFD). Using CFD would make it possible to make load predictions early in the design process and without resorting to the expensive physical testing. From a good CFD simulation, load intensity, as well as spectral characteristics and spatial distribution, can be extracted. The purpose of the CFD simulation would be to simulate the aerodynamical effect that creates the load directly. If the exposed structure is located in the near-field of the aerody-

namical effect, the load can be extracted directly from the CFD simulation. One example of this is the case of separated flow.

In the near field of a transonic flow case, the term acoustic fatigue becomes a bit misleading due to the fact that it becomes difficult to distinguish between acoustic loads and hydrodynamic loads. Thus, it is more suitable to just call these a pressure load. For cases where the exposed structure is located in the far field, it may be needed to simulate the acoustic load source without the domain extending all the way to the exposed surface in order to reduce the computational cost. The load would then have to be transferred to the structure via a wave-propagation method, for example the use of acoustic analogies. This touches the domain of Computational Aero Acoustics (CAA). A good book on CAA, including examples relevant for acoustic fatigue is [31]. In this thesis, only problems where the exposed structure is placed in the near-field are studied. CFD is discussed in more detail in Section 3.3.

A benefit of using a load generated by CFD is that it can be used as input to an FE-simulation of the panel response. Using the FEM to simulate the panel structure enables good response predictions of more complex structures. In contrast, equation (2.1) assumes a single rectangular metallic plate. Also the ESDU [1] design guidelines make similar assumptions. Composite panels can benefit from FE-simulations as their modeshapes and eigenfrequencies may not be as simple to predict as those of a rectangular plate. Also they exhibit non-linear response more frequently, which can be modelled using FEA, see Section 2.2.

3 Fluid dynamics

Fluid dynamics is a vast subject. It appears in many, if not every, part of our lives. Some examples are rivers, windmills, weather, breathing, blood flow, pipe systems, irrigation, sewage, ships, just to name a few. Most electricity is generated by having water or steam flow through a turbine. In this thesis, the field of study is limited to certain types of turbulent airflow around aircraft. First, turbulent flow is introduced in Section 3.1. This is followed by a description of the main properties of certain basic flow types that are important in this thesis in Section 3.2. The numerical methods used to simulate flows in this thesis is then described in Section 3.3. Finally, a post-processing tool called proper orthogonal decomposition is described in Section 3.4.

3.1 TURBULENT FLOW

3.1.1 Turbulent and laminar flow

Most fluid flows encountered in industrial applications are turbulent. The flows studied in this thesis are no exceptions; in fact, the turbulent nature of the flows in this thesis is essential. Turbulent flow is characterised by being chaotic, irregular and random. In contrast, laminar flow is smooth and orderly. Another characteristic for turbulent flow is high Reynolds number, Re, which was introduced by Reynolds (and later named after him) in his classic experiment from 1883 [32]. The Reynolds number is defined as

$$\text{Re} = \frac{UL}{\nu} = \frac{\text{Inertial forces}}{\text{Viscous forces}},$$

where U is a characteristic velocity of the flow, L is a characteristic length of the flow and ν is the kinematic viscosity of the fluid. It is a dimensionless number characterising the ratio between the inertial and the viscous forces of the flow. In Reynolds' experiment, he had water flowing through a straight glass pipe using streaks of dye for visualisation. He found that when the flow was below a certain critical Re, the streak of dye would remain straight and undisturbed; the flow was laminar. Above the critical Re, the dye streak would be disturbed, irregular, random
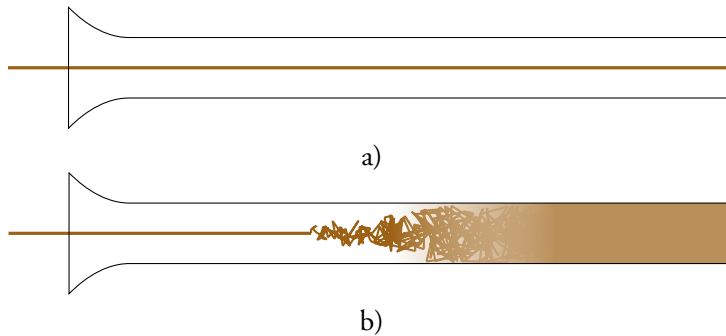
Figure 3.1: Reynolds experiment: a) laminar flow and b) turbulent flow. Sketched after [32].

and chaotic; the flow became turbulent. This is illustrated in Figure 3.1. While the critical Re is different for every specific flow, turbulent flows tend to be characterised by high Re and laminar flows by low Re. In other words, when the inertial forces become too large compared to the viscous forces, the flow becomes turbulent. There are some more features of turbulent flow worth mentioning. First, mixing is much faster in turbulent flow than in laminar flow. Both mass, momentum and heat transfer is enhanced by turbulence. Second, turbulent flows contain a large range of length and time scales (which will be further discussed in Section 3.1.2). Finally, note that turbulence is a property of the flow, not the fluid.

3.1.2 Scales of turbulence and energy cascade

As already mentioned, one of the features of turbulent flow is the large range of length and time scales. This feature is what makes numerical simulation of turbulent flow so difficult and demanding. Therefore some understanding of these disparate length-scales and how they interact according to the energy cascade theory are necessary. Richardson [33], who introduced the important concept of the energy cascade, summarised the process both concisely and poetically with:

> Big whirls have little whirls
> that feed on their velocity,
> and little whirls have lesser whirls
> and so on to viscosity —
> (in the molecular sense).

Turbulence is traditionally considered to be composed of eddies of different sizes. An eddy is a localised turbulent flow structure or motion. They also have a characteristic velocity and time scale dependent on the length scale. Figure 3.2 shows a schematical spectrum for the turbulent kinetic energy as a function of the wave number for a typical homogeneous turbulent flow. The wave number can be interpreted as the inverse of the eddy length scale. The spectrum shown
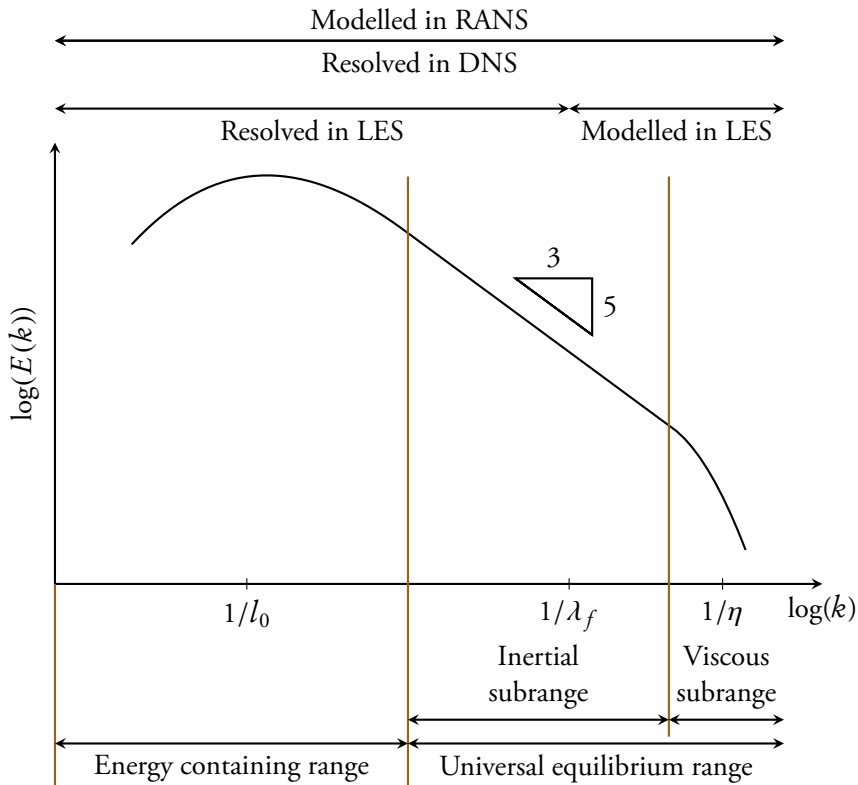
Figure 3.2: Turbulent kinetic energy spectrum $E(k)$ as function of wave number k.

in Figure 3.2 is divided into three zones, each characterised by a lengthscale. These are from the lowest wavenumber to the highest:

1. The energy containing range and the integral length scale l_0.
2. The inertial subrange and the Taylor microscale λ_f.
3. The viscous subrange and the Kolmogorov length scale η.

The integral length scale l_0 is representative for the largest eddies and is of the same order as the characteristic length of the flow, for example the pipe diameter or wing chord length. It contains more energy than the smaller eddies and therefore characterises the energy containing range. The eddies in this region tend to be highly anisotropic. In contrast, the smaller scales can be approximated to be isotropic according to Kolmogorov's hypothesis of local isotropy [34][1] (somewhat reformulated as according to Pope [36]):

> **Kolmogorov's hypothesis of local isotropy.** At sufficiently high Re, the small scale turbulent motions ($l \ll l_0$) are statistically isotropic.

---

[1]An English translation of the original paper in Russian is available as [35].

According to the theory of the energy cascade, large eddies break up into smaller eddies. The small eddies then further break up into even smaller eddies and the process continues until the turbulent kinetic energy of the eddies are dissipated into heat by viscosity. It should be noted that this is true for the process as a whole or on a statistical level. Smaller eddies can combine to larger ones and this is known as backscatter. The length scales where the dissipation dominates is called the viscous subrange which is characterised by the Kolmogorov length scale η. This theory is also based on Kolmogorov's hypotheses [34]:

> **Kolmogorov's first similarity hypothesis.** At sufficiently high Re, the statistics of the small scale motions have a universal form that is uniquely determined by the viscosity ν and the dissipation rate of turbulent kinetic energy ε.

The size range defined by the hypothesis is referred to as the universal equilibrium range which is divided into the inertial subrange and the viscous subrange. In the viscous subrange the flow is dominated by viscous forces as discussed above. In contrast, in the inertial subrange the viscous effects are small and the motions are dominated by inertial effects. The inertial subrange is characterised by the Taylor microscale λ_f and is defined by:

> **Kolmogorov's second similarity hypothesis.** At sufficiently high Re, there is a range of scales l such that $\eta \ll l \ll l_0$ that have a universal form that is uniquely determined by the dissipation rate of turbulent kinetic energy ε and independent of the viscosity ν.

The idea that smaller turbulent scales have a statistically universal and isotropic behaviour as described above, makes it sensible to try to approximate their behaviour by some model rather than spending the resources necessary to resolve all lengthscales completely. This is the basic idea of Large Eddy Simulation (LES) which will be discussed in Section 3.3.2.

3.2 SEPARATING/REATTACHING FLOW

3.2.1 Turbulent boundary layer

At the wall, the velocity of the fluid is exactly zero (or in the case of moving walls, the velocity is the same as that of the wall). This is called no-slip. As a consequence of this, there will be a velocity gradient next to the wall and a boundary layer will form. In Figure 3.3, flow over a flat plate is illustrated. Upstream of the plate the velocity profile is uniform. As the flow comes in contact with the plate, the plate will slow the flow down and a laminar boundary layer will form which is coloured in light blue. If the Reynolds number is sufficiently high, the flow will become turbulent which is illustrated further downstream. Important to note
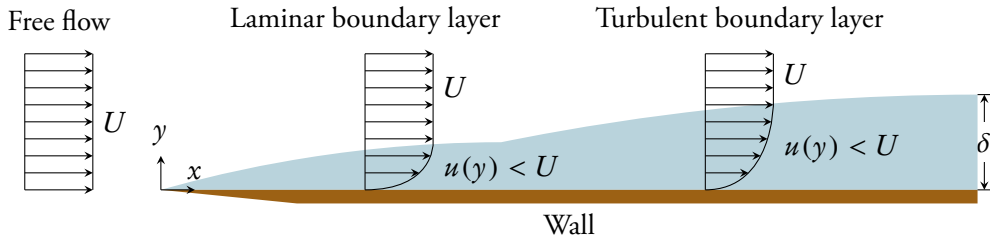
Figure 3.3: Boundary layer over a flat plate. U is the outer velocity and $u(y)$ is velocity in the boundary layer.

is that the boundary layer continues to grow with increasing x. The boundary thickness δ is defined as the distance from the wall where the velocity is 99 % of the external velocity U. An approximate expression for δ in turbulent flows is [37]

$$\delta \approx \frac{0.16x}{\mathrm{Re}_x^{1/7}},$$

where $\mathrm{Re}_x = \rho U x / \mu$ is the local Reynolds number of the flow along the plate surface and x is given in Figure 3.3. The fact that the turbulent boundary layer grows as the flow moves downstream has an important implication for the backward-facing step flow in Papers A and B. This required the implementation of a boundary condition in OpenFOAM which will be described in Section 3.3.6.

3.2.2 Backward-facing step flow

Flow over a backward-facing step is a classical test case for CFD. Despite having a very simple geometry it creates a complex flow. There are numerous experimental and numerical studies on this geometry in the literature. The main features of backward-facing step flow are illustrated in Figure 3.4. Upstream of the step, the flow is attached to the wall with a turbulent boundary layer. As the flow reaches the step edge, the flow separates forming a shear layer. The flow reattaches at some distance downstream. The mean reattachment length x_r is generally within the range $5h < x_r < 8h$ [38] where h is the step height as given in Figure 3.4. The point of reattachment is not fixed but moves in time. Just upstream of x_r is the intensity in the surface pressure fluctuations the highest. The step continues to influence the flow further downstream of the reattachment zone. In terms of surface pressure fluctuations, the distance until regular turbulent boundary layer levels are recovered can be as large as $175h$ [4]. Underneath the shear layer there is a clockwise rotating recirculation bubble (assuming flow from left to right as in Figure 3.4). In addition, there is a smaller counter-clockwise rotating corner eddy at the bottom corner of the step.
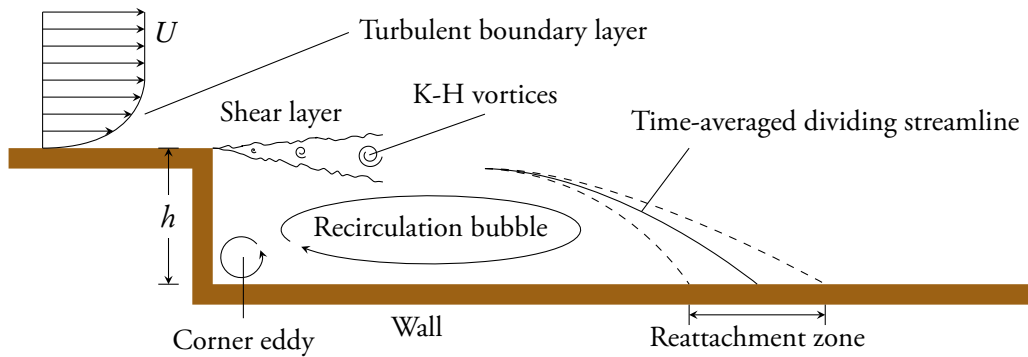
Figure 3.4: Schematic flow over a backward-facing step.

There are two instabilities commonly observed in backward-facing step flow. The first instability causes long spanwise structures known as Kelvin-Helmholtz (K-H) vortices to be shed form the step edge. These structures reduce to the shedding mode via one or more vortex merging processes as described by Hasan [39]. The shedding frequency is typically found to be in the range of $0.6 < \text{St}_{x_r} < 0.8$ where $\text{St}_{x_r} = f x_r / U$, f is the frequency and U is the freestream velocity. There is an important interaction between the turbulent boundary layer and the K-H vortices. The incoming turbulence helps the break up process of the K-H vortices. This reduces the surface pressure fluctuations downstream of the step. This is further discussed in relation to the inlet Boundary Condition (BC) used in Papers A and B in Section 3.3.6. The second instability is the absolute instability of the recirculation bubble. The instability is associated with the flapping motion of the shear layer. The flapping frequency is typically found in the range of $0.12 < \text{St}_{x_r} < 0.18$. It should be noted that there are different opinions about the physical explanation of the phenomenon observed as the flapping frequency. A compilation of shedding and flapping frequencies as well as mean reattachment length of many studies on backward-facing step flow is found in Dandois et al. [38].

The backward-facing step flow is used in Papers A and B with a small variation. The wall that is upstream to the step edge in Figure 3.4 is parallel to the downstream wall. This is not the case in Papers A and B. There, the upstream wall is a ramp with an inclination of 6.3°. The general flow characteristics described in this section remain the same. The ramped backward-facing step is used in order to match the geometry of the measurements used for comparison [40] in Paper A.

3.2.3 Fence flow

Another type of separating flow is fence flow. This type of flow is less studied than the backward-facing step flow, particularly numerically. The typical case of fence flow uses the kind of geometry as illustrated in Figure 3.5c. It consists of a splitter plate with a fence upstream. The
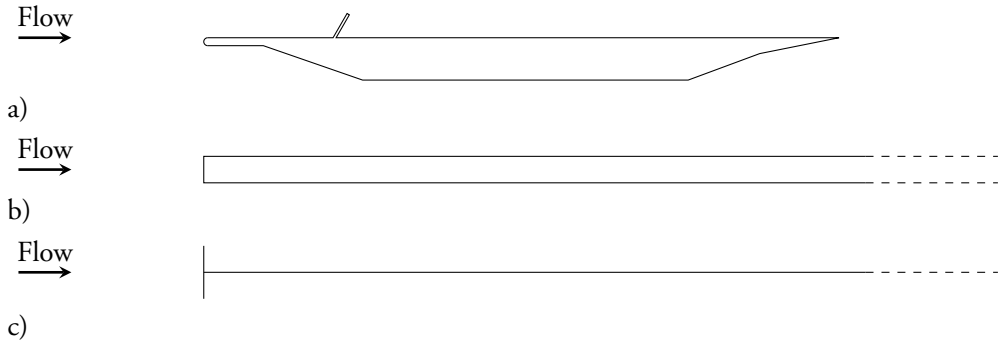
Figure 3.5: The geometry of different fence flow studies. a) is used in ACOUFAT [25], b) is used in Cherry et al. [41] and c) is used in Hudy et al. [42].

general characteristics for fence flow are similar to that of backward-facing step flow, but with some differences. The mean reattachment length tends to be longer and with a larger variation. Values in the range $10h < x_r < 34h$ are found in the literature.

The intensity in the maximum surface pressure fluctuations is more severe in fence flow compared to backward-facing step flow. For the backward facing-step the r.m.s. value of the surface pressure fluctuations p'_{rms} is typically around $p'_{rms}/(0.5\rho U^2) = 0.035$, where ρ is the fluid density and U is the freestream velocity. This can be compared to the experimental study on the typcial fence flow geometry in Figure 3.5c by Hudy et al. [42] which found $p'_{rms}/(0.5\rho U^2) = 0.16$ and the experimental study by Cherry et al. [41] which found $p'_{rms}/(0.5\rho U^2) = 0.125$. However, the study by Cherry et al. [41] used the blunt face splitter plate geometry illustrated in Figure 3.5b. An inclined fence as illustrated in Figure 3.5a is used as a model problem in Papers C–E. This geometry was also used in the ACOUFAT project [25]. The simulations in Paper C–E found the maximum $p'_{rms}/(0.5\rho U^2) = 0.06$ and the measurements in the ACOUFAT project [25] $p'_{rms}/(0.5\rho U^2) = 0.05$. This is far below the values found by Hudy et al. [42] and Cherry et al. [41]. It is suggested in Paper C that this is due to the interaction, or lack thereof, between the incoming turbulence and the shed K-H vortices. For the fence flow geometries in Figures 3.5b and 3.5c, there is no incoming turbulent boundary layer and therefore the strong K-H vortices will have a slower break-up rate. The leading edge in Figures 3.5a does cause some turbulence which may interact with the shed K-H vortices. The pressure fluctuation intensity in Paper C is still higher compared to backward-facing step flow. The reason for this is likely due to the difference in geometry and the thinner boundary layer in the fence flow case. Furthermore, there are three-dimensional effects present from the finite spanwise width of the fence and wind-tunnel test-table in the ACOUFAT measurement [25]. These three-dimensional effects produce a maximum in the p'_{rms} curve further upstream than the shedding mode maximum and are the topic of Paper D.

3.3 NUMERICAL METHODS

The numerical treatment of fluid flow is discussed in this section. In this thesis, the software package OpenFOAM [43–45] is used. It is an open source finite volume based software, released for free under the GNU General Public License. It is written in C++ making heavy use of object oriented programming, templates and operator overloading. This is used to create a syntax for tensor operations and partial differential equations that looks similar to the equations written in mathematical notation, thus facilitating the development of new solvers. It also lends itself to implementation of other extensions such as new turbulence models or boundary conditions. However, the code is poorly documented and the class relationships can be very complex, making the learning curve steep. The lack of extensive documentation does not only apply to the source code itself, but also for general usage. However, since 2014 there is a third party book about OpenFOAM [46]. OpenFOAM does come with some mesh generation and manipulation tools such as a block mesher and a tool that makes an unstructured mesh around a geometry file. However, it does not include any pre-processing Graphical User Interface (GUI) and instead comes with a large set of mesh converters for meshes created by other software. The third party post-processor ParaView is used as OpenFOAM does not contain a post-processor of its own.

There are several different topics that need to be addressed to have a full working numerical method. The governing equations of viscous flow will be stated and some of their properties will be discussed in Section 3.3.1. The high Reynolds numbers of the studied flows in this thesis dictate the use of turbulence modelling which will be discussed in Section 3.3.2. The near wall regions are especially demanding, requiring wall treatment that is discussed in Section 3.3.3. The discretisation methods used in both space and time are discussed in Section 3.3.4. A solver algorithm is needed to produce a solution and this is covered in Section 3.3.5. Finally, custom inlet boundary conditions implemented in OpenFOAM that are used in Papers A and B are described in Section 3.3.6.

3.3.1 Governing equations

Viscous flow is governed by the Navier-Stokes equations which is a system of non-linear partial differential equations. They consist of the continuity equation (3.1), momentum equations (3.2) and the energy equation (3.3) [47]:

$$\frac{\partial \rho}{\partial t} + \nabla \cdot (\rho \mathbf{u}) = 0, \tag{3.1}$$

$$\frac{\partial (\rho \mathbf{u})}{\partial t} + \nabla \cdot (\rho \mathbf{u} \otimes \mathbf{u}) = -\nabla p + \nabla \cdot \boldsymbol{\tau} + \rho \mathbf{b}, \tag{3.2}$$

$$\frac{\partial (\rho e)}{\partial t} + \nabla \cdot (\rho e \mathbf{u}) + \frac{\partial (\rho e_{\mathrm{k}})}{\partial t} + \nabla \cdot (\rho e_{\mathrm{k}} \mathbf{u}) + \nabla \cdot (p \mathbf{u}) = \nabla \cdot (\alpha \nabla e) + \nabla \cdot (\boldsymbol{\tau} \mathbf{u}), \tag{3.3}$$

where $\otimes$ is the outer product, e is the internal energy, e_k is the kinetic energy, α is the thermal diffusivity, $\boldsymbol{\tau}$ are the viscous stresses (a second order tensor), $\mathbf{b}$ are the body forces, ρ, $\mathbf{u}$ and p are the fluid density, velocity and pressure, respectively. No body forces are considered in this thesis, thus $\mathbf{b} = \mathbf{0}$. In addition, the heating effect from viscous dissipation is neglected. This means that the $\nabla \cdot (\boldsymbol{\tau}\mathbf{u})$ term in the energy equation (3.3) is dropped. The system needs to be closed with equations of state. In this thesis with the fluid being air, the ideal gas law is used:

$$e = C_V T, \quad e = h - \frac{p}{\rho}, \quad h = C_p T, \quad C_p - C_V = R, \quad \rho = \frac{p}{RT}, \quad e_k = \frac{\mathbf{u} \cdot \mathbf{u}}{2}, \quad (3.4)$$

where T is the temperature, R is the specific gas constant, h is the enthalpy, and C_V and C_p are the specific heats at constant volume and at constant pressure, respectively.

For Newtonian fluids, the viscous stresses are

$$\boldsymbol{\tau} = \mu \left(2\mathbf{S} - \frac{2}{3}(\nabla \cdot \mathbf{u})\mathbf{I} \right), \quad \mathbf{S} = \frac{1}{2} \left(\nabla\mathbf{u} + (\nabla\mathbf{u})^T \right), \quad (3.5)$$

where μ is the dynamic viscosity, $\mathbf{I}$ is the identity tensor and $\mathbf{S}$ is the rate-of-strain tensor. A Newtonian fluid is a fluid whose viscous stresses are proportional to the shear strain rate. Many common liquids and gases, including the important examples of air and water, can be assumed to be Newtonian. Examples of non-Newtonian fluids are quicksand which stiffens with the increasing shear strain rate while blood and non-drip paint is less resistant at higher shear strain rates. The fluid in this thesis is air, thus the assumption of Newtonian fluid is applied.

If the flow has a Mach number Ma < 0.3 it can with good accuracy be approximated as incompressible flow. In many flows, both ρ and μ can also be approximated as constant. Assume that the flow is incompressible with constant ρ and μ and that the fluid is Newtonian. Then there are only four unknowns $(\mathbf{u}, p)$ and four equations in the continuity equation (3.1) and momentum equations (3.2). This means that the energy equation is not needed for incompressible flow, simplifying the problem. Should one be interested in the thermal effects of the flow, the energy equation (3.3) can of course be included if desired. Thus, the incompressible Navier-Stokes equations with constant ρ and μ for Newtonian fluids and without body forces can be written as:

$$\nabla \cdot \mathbf{u} = 0, \quad (3.6)$$

$$\rho \frac{\partial \mathbf{u}}{\partial t} + \rho \nabla \cdot (\mathbf{u}\otimes\mathbf{u}) = -\nabla p + \mu \nabla^2 \mathbf{u}, \quad (3.7)$$

where the following expression for Newtonian fluids in incompressible flows has been used

$$\boldsymbol{\tau} = \mu \left(\nabla\mathbf{u} + (\nabla\mathbf{u})^T \right) = 2\mu\mathbf{S}.$$

Note that the pressure is missing from the continuity equation (3.6). This means that the continuity equation acts as a constraint to the solution. In addition, this means that there is no independent equation for the pressure.

Due to the low Mach numbers in Papers A and B, the incompressible forumlation of the Navier-Stokes equations in (3.6) and (3.7) are used, with the slight modification that (3.7) is divided by ρ. Because of the higher Mach numbers of the transonic flow in Papers C–E, the full compressible set of Navier-Stokes equations and constitutive relations in (3.1)–(3.5) are needed.

There are only a few special cases where the Navier-Stokes equations have known analytical solutions. In practice, the only realistic way to achieve solutions of the Navier-Stokes equations is to use computer simulations, or more specifically, Computational Fluid Dynamics (CFD).

3.3.2 Turbulence modelling

The large range of length and time scales of turbulent flows is from a computational view problematic. The resolution and accuracy needed to capture all turbulent scales comes at extreme computational costs except for flows with very low Reynolds numbers. To combat this problem, the turbulence is to a varying degree modelled. The main strategies for dealing with turbulence will be outlined here.

Direct Numerical Simulation

The perhaps conceptually easiest strategy is to simply resolve all turbulent scales all the way down to the Kolmogorov scale. This means that no turbulence model is used, see Figure 3.2. This is called Direct Numerical Simulation (DNS) and is only used for very low Reynolds numbers and mainly in the academic world. It requires very high spatial and temporal resolution as well as high order numerical schemes that have a low numerical dissipation. The computational cost is proportional to Re^3. Using DNS is far too computationally expensive for the problems studied in this thesis and will remain so for a long time.

Reynolds Averaged Navier-Stokes

To avoid the high costs of DNS, the effects of turbulence can be modelled. In Reynolds Averaged Navier-Stokes (RANS), temporal (or ensemble) averaging is used. The idea is to lower the ambition from resolving everything to getting the right solution in the statistical sense. Any variable f can be decomposed into two parts, an averaged $\overline{f}$ and a fluctuating f', such that $f = \overline{f} + f'$. Only the $\overline{f}$ part is solved for in RANS. The effect of the fluctuations f' is introduced as an unknown called Reynolds stresses in the equations solving for $\overline{f}$. This is typically done by Boussinesq's hypothesis where a turbulent viscosity is added to the molecular viscosity of the fluid. All scales of turbulence are taken into account for with the addition of the turbulent viscosity (see also Figure 3.2). The models for how this is done can be fairly elaborate.

The common k-ε family uses two additional transport equations for this purpose alone. The RANS type of modelling is the type of modelling that requires the smallest computational resources. However, it also has the worst accuracy for complex flows. A prime example of this are flows with strong streamline curvature, like the ones in this thesis. To capture the turbulence interactions with vortex shedding and vortex breakdown properly is central in this thesis. This makes RANS modelling inadequate.

Large Eddy Simulation

Large Eddy Simulation (LES) uses filtering in space instead of averaging in time. The filtering in LES is performed according to

$$\overline{f} = \int f(x')F_\Delta(x - x')dx',$$

where F_Δ is the LES filter of width Δ. The filtering can be done in physical or spectral space. The idea here is to filter out the small eddies while keeping the large eddies. As already mentioned in Section 3.1.2, the smaller turbulent scales exist in the "universal equilibrium range". As the name implies, their behaviour is expected to be universal. This makes them prime target for modelling. The large eddies on the other hand depend on the geometry and flow characteristics and are not modelled. This is illustrated in Figure 3.2. Ideally, parts of the inertial subrange are resolved to ensure that the modelled eddies are well inside the universal equilibrium range. Only a small fraction of the turbulent kinetic energy resides in the modelled part.

The filtering of the smallest length and time scales reduces the resolution requirements compared to DNS. As the filter width Δ gets smaller, the LES solution should tend to the DNS solution. LES places itself in between RANS and DNS both when it comes to accuracy and computational costs. LES captures more aspects of the flow than RANS, but less than DNS. On the other hand, the computational costs are higher than RANS but smaller than DNS. In this thesis, the accuracy requirements preclude the use of RANS, while the Reynolds numbers make a DNS simulation far too costly to be possible. Therefore, the LES approach is chosen for the turbulence modelling.

In the incompressible case, assuming Newtonian fluid and constant ρ and μ, the filtered versions of equations (3.6) and (3.7) become

$$\nabla \cdot \overline{\mathbf{u}} = 0, \tag{3.8}$$

$$\rho\frac{\partial \overline{\mathbf{u}}}{\partial t} + \rho\nabla \cdot (\overline{\mathbf{u} \otimes \mathbf{u}}) = -\nabla\overline{p} + \mu\nabla^2\overline{\mathbf{u}}, \tag{3.9}$$

where the overbar indicates filtered quantities. Equation (3.9) is different from (3.7) because $\overline{\mathbf{u} \otimes \mathbf{u}} \neq \overline{\mathbf{u}} \otimes \overline{\mathbf{u}}$. The difference is introduced as an unknown term in the form of the sub-grid

stress tensor

$$\boldsymbol{\tau}_{\text{sgs}} = \rho(\overline{\mathbf{u}\otimes\mathbf{u}} - \overline{\mathbf{u}}\otimes\overline{\mathbf{u}}), \tag{3.10}$$

to obtain

$$\rho\frac{\partial\overline{\mathbf{u}}}{\partial t} + \rho\nabla\cdot(\overline{\mathbf{u}}\otimes\overline{\mathbf{u}}) = -\nabla\overline{p} + \mu\nabla^2\overline{\mathbf{u}} - \nabla\cdot\boldsymbol{\tau}_{\text{sgs}}. \tag{3.11}$$

Equations (3.8) and (3.11) are solved as usual with the sub-grid stress tensor (3.10) calculated from an LES-model (or sub-grid stress model). This is necessary as the $\overline{\mathbf{u}\otimes\mathbf{u}}$ term is unknown. The sub-grid stress tensor $\boldsymbol{\tau}_{\text{sgs}}$ can be expanded using the Leonard decomposition as

$$\boldsymbol{\tau}_{\text{sgs}} = \rho(\overline{\mathbf{u}\otimes\mathbf{u}} - \overline{\mathbf{u}}\otimes\overline{\mathbf{u}}) = (\rho\overline{\overline{\mathbf{u}}\otimes\overline{\mathbf{u}}} - \rho\overline{\mathbf{u}}\otimes\overline{\mathbf{u}}) + (\rho\overline{\overline{\mathbf{u}}\otimes\mathbf{u}'} + \rho\overline{\mathbf{u}'\otimes\overline{\mathbf{u}}}) + (\rho\overline{\mathbf{u}'\otimes\mathbf{u}'}) = \mathsf{L} + \mathsf{C} + \mathsf{R},$$

where L is known as the Leonard stress tensor, C is the cross stress and R is the Reynolds stress. The L, C and R terms represent redistribution, backscatter and outscatter, respectively. Note that L can be computed directly from the resolved scales while C and R must be modelled. Or, as an alternative, one can model the entire sub-grid stress tensor $\boldsymbol{\tau}_{\text{sgs}}$ directly.

Just like RANS models, there are many different LES models. There is also the option of using none at all which means that the numerically introduced dissipation is assumed to be similar to the effect of the unresolved scales. This is called implicit LES or ILES. The ideal LES model should have the following qualities: It should represent the effects of redistribution, backscatter and outscatter. Since this thesis does not focus on the fitness of different sub-grid stress models, a full survey of the field of different sub-grid stress models will not be given here. Instead, only the models used in this thesis are described. For a deeper discussion and a comparison of different sub-grid stress models, the interested reader is referred to [48–50].

The sub-grid stress models in this thesis are of the eddy-viscosity type. These models are based on the assumption that the deviatoric part of $\boldsymbol{\tau}_{\text{sgs}}$ is aligned with the deviatoric part of $\overline{\mathbf{S}}$ and the normal stresses are assumed to be isotropic and can therefore be represented with a scalar k called the sub-grid turbulent energy [48]. In other words assume

$$\boldsymbol{\tau}_{\text{sgs}} = \frac{2}{3}k\mathbf{I} + \text{dev}(\boldsymbol{\tau}_{\text{sgs}}) = \frac{2}{3}k\mathbf{I} - 2\mu_{\text{sgs}}\text{dev}(\overline{\mathbf{S}}), \tag{3.12}$$

where $k = 1/2\text{tr}(\boldsymbol{\tau}_{\text{sgs}})$ and μ_{sgs} is the sub-grid viscosity (the so called eddy-viscosity). Different methods can be employed to determine k and μ_{sgs}. In this thesis we deal with a dynamic one equation model (Papers D and E) and the Samgorinsky model (Papers A–C).

One equation eddy model

From the filtered and unfiltered Navier-Stokes equations, an exact transport equation for the sub-grid stresses $\boldsymbol{\tau}_{\text{sgs}}$ can be derived. This transport equation can then be contracted to produce a transport equation for k. If it is assumed that the dissipation can be modelled as $C_\varepsilon\overline{\rho}k^{3/2}/\Delta$

and the diffusive effects can be modelled as $\nabla \cdot (\mu_{\text{eff}} \nabla k)$ where μ_{eff} is $\mu_{\text{eff}} = \mu + \mu_{\text{sgs}}$ (the sum of the molecular and sub-grid viscosity), the following transport equation is produced

$$\frac{\partial \overline{\rho} k}{\partial t} + \nabla \cdot (\overline{\rho}\, \overline{\mathbf{u}} k) = -\overline{\rho} \boldsymbol{\tau}_{\text{sgs}} : \overline{\mathbf{S}} + \nabla \cdot (\mu_{\text{eff}} \nabla k) - \frac{C_\varepsilon \overline{\rho} k^{3/2}}{\Delta}, \tag{3.13}$$

$$\mu_{\text{sgs}} = C_k \sqrt{k} \Delta. \tag{3.14}$$

This is the model of Yoshizawa [51] (see also [49]). The default values of C_k and C_ε in Open-FOAM for compressible flows are $C_k = 0.094$ and $C_\varepsilon = 1.048$. The transport equation (3.13) is solved, using (3.12) and (3.14), together with the filtered Navier-Stokes equations. In this thesis, a dynamic version of the one equation eddy model is used where the constants C_k and C_ε are computed based on the flow field. The method is based on the model of Ghosal [52] (see also [48]):

$$C_k = \frac{\langle \mathbf{L} : \mathbf{N} \rangle}{\langle \mathbf{N} : \mathbf{N} \rangle}, \quad C_\varepsilon = \frac{\langle em \rangle}{\langle mm \rangle},$$

$$K = \frac{1}{2} \left(\widehat{\overline{\mathbf{u}} \cdot \overline{\mathbf{u}}} - \widehat{\overline{\mathbf{u}}} \cdot \widehat{\overline{\mathbf{u}}} \right), \quad \mathbf{L} = \text{dev} \left(\widehat{\overline{\mathbf{u}} \otimes \overline{\mathbf{u}}} - \widehat{\overline{\mathbf{u}}} \otimes \widehat{\overline{\mathbf{u}}} \right),$$

$$\mathbf{N} = \Delta \left(\widehat{\sqrt{k} \text{dev}(\overline{\mathbf{S}})} - 2 \sqrt{K + \hat{k}} \widehat{\text{dev}(\overline{\mathbf{S}})} \right), \quad m = \frac{\left(K + \hat{k} \right)^{3/2}}{2\Delta} - \frac{\widehat{k^{3/2}}}{\Delta},$$

$$e = 2\Delta C_k \left(\widehat{\sqrt{k} \text{dev}(\overline{\mathbf{S}}):\text{dev}(\overline{\mathbf{S}})} - 2 \sqrt{K + \hat{k}} \widehat{\text{dev}(\overline{\mathbf{S}}):\text{dev}(\overline{\mathbf{S}})} \right),$$

where the $\langle \bullet \rangle$ indicates a domain wide average and the hat indicates that the quantity underneath has been filtered by a second LES-filter.

The Smagorinsky model

The first LES model developed is the Smagorinsky model [53] and it is also one of the simplest. In addition to (3.12), it is based on the assumption that the local equilibrium prevails. That is, the production and dissipation of k is equal. In OpenFOAM, the implementation is closely related to the one equation model. Instead of solving (3.12), k is determined by setting the production and dissipation term in (3.13) to be equal, i.e.

$$-\overline{\rho} \boldsymbol{\tau}_{\text{sgs}} : \overline{\mathbf{S}} = \frac{C_\varepsilon \overline{\rho} k^{3/2}}{\Delta} \tag{3.15}$$

together with (3.12) and (3.14). This way the model becomes completely algebraic. The default coefficients in OpenFOAM for compressible simulations (used in Paper C) are $C_k = 0.02$ and $C_\varepsilon = 1.048$.

In the incompressible case, (3.15) reduces to a much simpler expression for k

$$k = 2\frac{C_k}{C_\varepsilon}\Delta^2\overline{\mathbf{S}}{:}\overline{\mathbf{S}}. \tag{3.16}$$

From (3.16) and (3.14) a simple expression can therefore be given for μ_{sgs}:

$$\mu_{\mathrm{sgs}} = \rho C_k \sqrt{\frac{C_k}{C_\varepsilon}}\Delta^2 \sqrt{2\overline{\mathbf{S}}{:}\overline{\mathbf{S}}}. \tag{3.17}$$

For incompressible simulations, the default values for the coefficients (used in Papers A and B) are $C_k = 0.094$ and $C_\varepsilon = 1.048$. It is more common to express the Smagorinsky model with one coefficient instead of the two that is used in OpenFOAM:

$$\mu_{\mathrm{sgs}} = \rho(C_S\Delta)^2 \sqrt{2\overline{\mathbf{S}}{:}\overline{\mathbf{S}}}, \tag{3.18}$$

where C_S is the Smagorinsky constant. By comparing (3.17) and (3.18), we see that the default values in OpenFOAM gives C_S the value of about $C_S \approx 0.1678$ in the incompressible case.

Comparison of the one equation model and the Smagorinsky model

There are two main differences between the one equation model used in this thesis and the Smagorinsky model. First, as shown in the subsection about the Smagorinsky model, the Smagorinsky model assumes local equilibrium, i.e. production and dissipation of k are in balance. The more the flow strays from this assumption, the worse the Smagorinsky model will perform. Local equilibrium is not assumed in the one equation model. Second, the use of a transport equation for k in the one equation model enables it to take account for non-local and history effects. This is not possible in the algebraic Smagorinsky model. Both these differences mean that the one equation model should take more effects into account and therefore should give better predictions in general. However, it comes at a price. The addition of a transport equation adds complexity and computational cost.

3.3.3 Wall treatment

Most flows of practical interest are wall bounded and have some form of turbulent boundary layer. This is a serious issue in LES. The resolution requirement for LES increases in the turbulent boundary layer near walls. The inner layer of the boundary-layer is particularly demanding. According to Piomelli and Balaras [54], at approximately $\mathrm{Re}_L = 10^6$, where L is the integral length scale, 99 % of the cells used to simulate a boundary-layer flow are used to resolve the inner layer whose thickness is only 10 % of the boundary layer. The share of cells needed in the inner layer also increases with Re_L. Expressed differently; the mesh resolution

needed in resolved LES closest to the wall is nearly as fine as DNS [55]. Clearly, resolving the inner layer with LES is not possible for the Reynolds numbers considered in this thesis and some kind of modelling is needed. For a more detailed explanation of the higher near wall resolution requirements in LES, see [54].

The main categories of wall-treatments will be discussed briefly. The only model which will be explained in detail is the one used in this thesis (an equilibrium stress model based on Spalding's law of the wall [56]). The wall-modelling is not used in the simulations with the dynamic one equation model. For a more complete coverage, the interested reader is referred to [57].

Equilibrium stress models

This class of models tries to use an expression to compute the wall shear stress from the local velocity at the first off-the-wall grid point. This is then fed back to the LES simulation. In a way this can be seen as a wall-stress corrector. If the stresses in the boundary layer are assumed to be in equilibrium (average or instantaneous) this means that the boundary layer should follow the logarithmic law of the wall.

$$u^+ = \frac{u}{u_\tau} = \frac{1}{\kappa}\log y^+ + B, \tag{3.19}$$

where u is the velocity parallel to the wall, u^+ is u in wall units, u_τ is the friction velocity or shear velocity, κ is the von Kármán constant, y^+ is the distance y to the wall in wall units ($y^+ = (yu_\tau\rho)/\mu$) and B is a constant. For (3.19) to be applicable, the first grid point must be in the so called log-law region, i.e. far enough from the wall that viscous effects are negligible. To ensure this, the first grid point of the wall should be placed at $y^+ > 30$.

In OpenFOAM, there exists an equilibrium stress model based on the more universal velocity profile, Spalding's law [56]:

$$y^+ = u^+ + \frac{1}{E}\left(e^{\kappa u^+} - 1 - \frac{\kappa u^+}{1!} - \frac{(\kappa u^+)^2}{2!} - \frac{(\kappa u^+)^3}{3!}\right), \tag{3.20}$$

where κ and E are constants with the default values of $\kappa = 0.41$ and $E = 9.8$. The values of y^+ and u^+ are computed by inserting the known values of y and u next to the wall into $y^+ = (yu_\tau\rho)/\mu$ and $u^+ = u/u_\tau$, respectively. Then (3.20) is iterated using the Newton-Raphson method to determine the value of u_τ. The following relations that apply for the wall shear stress τ_w

$$\tau_w = (\mu + \mu_T)\left(\frac{\partial u}{\partial y}\right)_{y=0} = u_\tau^2\rho,$$

is then used to obtain the turbulent viscosity at the wall

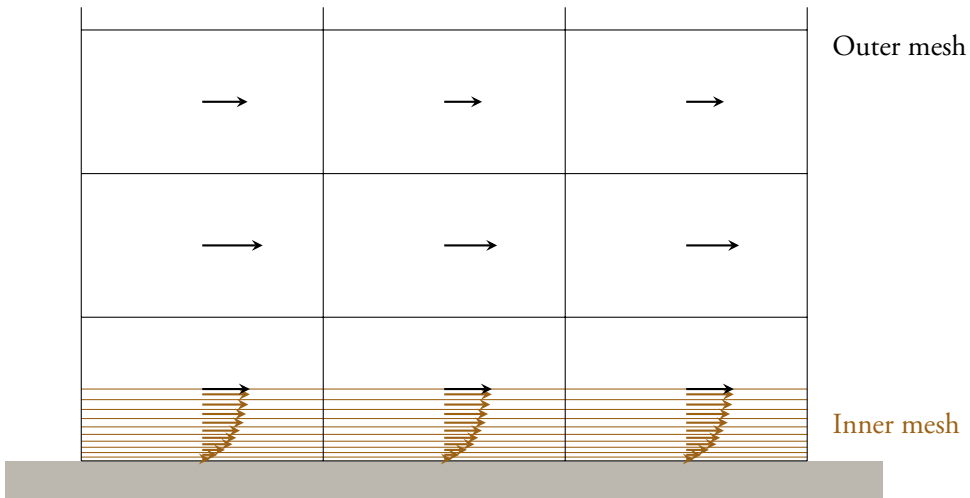$$\mu_T = \frac{u_\tau^2\rho}{\left(\frac{\partial u}{\partial y}\right)_{y=0}} - \mu.$$

Figure 3.6: Inner and outer mesh for the two-layer model.

Using Spalding's law instead of the log-law (3.19) removes the restriction of $y^+ > 30$. This does not force a change of wall-treatment when $y^+ < 30$ which would have been the case if the log-law would have been used.

Two-layer models

In the two-layer models two separate grids are used. There is a coarser outer mesh that takes care of the flow away from the wall, and a mesh inside the cell of the coarse mesh that is closest to the wall. This second mesh is much refined in the wall-normal direction, see Figure 3.6. The standard filtered LES equations are solved on the coarser mesh and simplified transport equations called boundary layer equations are solved in the finer inner mesh. The inner mesh is solved with a no-slip BC next to the wall and with the velocity from the coarser mesh in the upper interface. The wall-stress is then integrated over the finer mesh and is used as BC for the coarser outer mesh. According to [57] the two-layer models only increase the cost of an LES calculation by 20 to 30 % compared to the use of wall functions (equilibrium stress models). The two-layer models have the advantage when compared to equilibrium models of being more accurate in situations where the equilibrium assumptions do not hold. On the other hand, in situations where assumptions of the simplified equations used in the near wall mesh are invalid, the accuracy will suffer. The two-layer models have an obvious drawback. It requires a second mesh that matches the outer mesh along all walls that the model is applied to. Also, dealing with two simulations in one is more complex.

Detached Eddy Simulation

Detached Eddy Simulation (DES) is a hybrid between LES and RANS. Similarly to the two-layer model, the simulation is divided into two parts where LES is used in the outer flow away from the walls and RANS is used near walls. However, in contrast to two-layer models, the same mesh is used forming one single domain. The first DES model was proposed in 1997 by Spalart et al. [58] making it a fairly recent model. The use of RANS in the near wall region is a much more advanced treatment than the other models discussed here, enabling greater accuracy in the near wall region. It also enables the use of RANS quality meshes near the wall. That is, the wall-normal resolution is high, but the streamwise resolution can be much coarser than in LES. It has achieved great success in many areas and there is a very active development of new DES methods. Nevertheless, the DES concept has its disadvantages.

The first DES model [58] uses the Spalart-Allmaras (S-A) one-equation eddy viscosity model [59] as the RANS model. In the LES mode, the S-A model is similar to the Smagorinsky model. The model includes a term d that depends on the distance to the closest wall y_w in the RANS zone and on the largest cell dimension Δ_{DES} in the LES zone. This is achieved by $d = \min(y_w, \Delta_{\mathrm{DES}})$. This also means that the relation between y_w and Δ_{DES} determines if the cell is in the RANS or LES zone. Close to the wall y_w is smaller than Δ_{DES} so the RANS model is chosen and vice versa far from the wall. This means that when the mesh is refined near the wall, the RANS zone will diminish. This is not always good as it is desired that the RANS model takes care of the near wall region. In fact, this can cause so called grid-induced separation where the flow separates due to grid refinement. This is counter-intuitive as one typically likes to be able to improve the solution by refining the grid until grid independence is reached. Here, the solution can actually become worse as the mesh is refined. This has been addressed in several variants, perhaps most notably the Delayed Detached Eddy Simulation (DDES) [60]. Still, the user must be careful with the mesh generation.

Another issue with DES is the log-layer mismatch. The RANS solution does not need to match the LES solution in the interface between the two. This causes a more or less sudden jump in velocity between the regions. Mesh refining appears to only move the point of mismatch. This is discussed in [61] when DES is used as a wall model to channel flow.

The strength of DES is in separated flows, such as the flow around a cylinder. In this case there is a boundary layer mainly on the upstream half of the cylinder. Any vortices formed in this boundary layer will be overpowered by the turbulence from the separation. However, there is an issue highlighted by de Villiers [57] when the vortices formed at separation are affected by the upstream boundary layer. The RANS near wall solution should in theory reduce to a steady RANS solution with no resolved eddies in it. The RANS properties of the boundary layer should be fine; it is just that any resolved turbulence is suppressed. This is not an issue in the cylinder case described above. Clearly, if the wall-attached eddies have a strong effect on the eddies caused by separation, this is an issue. This was determined by de Villiers when applying it to an asymmetric plane diffuser [57]. In Paper A, it is found that the turbulence

in the incoming boundary layer has an important effect on the rate of break-up of the Kelvin-Helmholtz (K-H) vortices shed from the step edge of the backward-facing step. A lack of turbulence in the incoming boundary layer decreases the K-H vortices break-up rate, increasing the pressure fluctuations on the downstream surface. For this reason DES is not very well suited for this kind of problem. For a review on DES methods, see [61].

3.3.4 Numerical discretisation

Within the subject of Computational Fluid Dynamics (CFD) there exist several discretisation strategies. The three main categories are Finite Differences (FD), Finite Volume (FV) and Finite Elements (FE). Finite differences is the oldest of the three. It is often used on Cartesian grids or structured grids that have a high regularity. Exploiting such properties gives fast codes and codes with a small memory footprint. They are simple and allow the use of high order schemes resulting in high accuracy. However, the grid requirements make it difficult to handle complex geometries reducing its flexibility. The combination of high accuracy and low flexibility makes it mainly popular in the academic world for problems with simple geometries.

Despite the popularity of the FE-method in many engineering fields such as solid mechanics and structural dynamics, it has traditionally not been extensively used in fluid mechanics. The FE-method can use high order accuracy and handle arbitrary geometries well. But there are two disadvantages that have held it back. The conservation properties are very important in CFD and FE-methods have traditionally been unable to conserve mass. Also, FE-methods tend to use more computational resources than FV and FD methods due to their higher order nature. It turns out that a lower order method with more grid points is often preferable in CFD. Nevertheless, FE based CFD appears to be on the rise with FE based CFD modules being integrated into large FE software packages for structural analysis.

The FV discretisation is the most common discretisation strategy employed in CFD. The domain is divided into a finite number of control volumes and the discretisation is based on the conservation of quantities in each control volume. The main advantages are that quantities are conserved and that complex geometries can be easily accommodated. However, there is one disadvantage against both FD and FE methods: It is difficult to develop higher order interpolation schemes.

The FV-method is used by OpenFOAM and this thesis. The FV-method implemented in OpenFOAM will now be outlined. The filtered Navier-Stokes equations with the corresponding sub-grid stress models discussed in previous sections result in many different terms that require discretisation. Instead of addressing every term specifically, the following transport equation for the generic variable ϕ (which may be a scalar, vector or tensor) is studied,
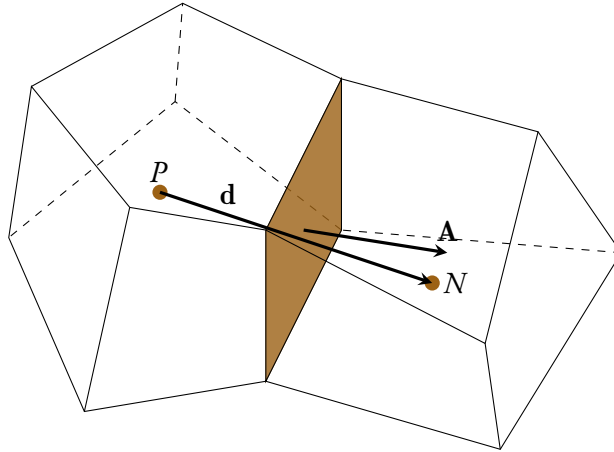
Figure 3.7: Control volume, or cell, for the finite volume discretisation.

$$\underbrace{\frac{\partial}{\partial t} \int_V \rho \phi \mathrm{d}V}_{\text{Time derivative}} + \underbrace{\int_V \nabla \cdot (\rho \mathbf{u} \phi) \mathrm{d}V}_{\text{Convection}} - \underbrace{\int_V \nabla \cdot (\rho \Gamma \nabla \phi) \mathrm{d}V}_{\text{Diffusion}} = 0, \qquad (3.21)$$

where Γ is the diffusivity coefficient.

Spatial discretisation

In the FV-method, the entire computational domain is divided into control volumes, or cells. The cells do not overlap and can have an arbitrary number of faces (sides) as long as the faces are convex, see Figure 3.7. The mesh can be structured or unstructured. The quantities of interest are mainly stored at the cell centre P and are co-located, i.e. all quantities are stored in the same location (as opposed to a staggered formulation). Here, the discretisation of some general terms will be illustrated, for a more complete derivation, see the work by Jasak [45].

In the FV-method, the quantities of interest are integrated over the cell. With ϕ being the variable of interest, this means

$$\int_{V_P} \phi(\mathbf{x}) \mathrm{d}V = \phi_P V_P, \qquad (3.22)$$

where V_P is the cell volume and ϕ_P is ϕ at the cell centre P. For the divergence operator this gives

$$\int_{V_P} \nabla \cdot \phi \mathrm{d}V = \int_{\partial V_P} \phi \cdot \mathrm{d}\mathbf{A} = \sum_f \left(\int_f \phi \cdot \mathrm{d}\mathbf{A} \right) = \sum_f \phi_f \cdot \mathbf{A}, \qquad (3.23)$$
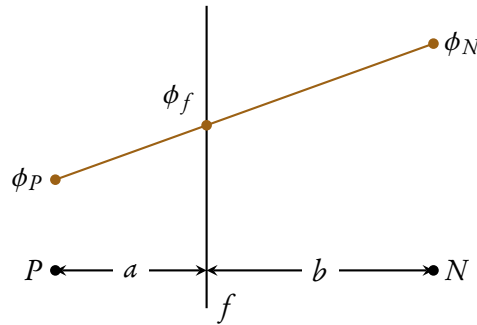
Figure 3.8: Face interpolation.

where $\mathbf{A}$ is the outward pointing surface area vector, f is the (flat) face surface and ϕ_f is the value of ϕ on the surface. The value of ϕ_f needs to be determined from interpolation which will be described later.

Applying (3.22) and (3.23) to the generic convection term in (3.21) gives

$$\int_{V_P} \nabla \cdot (\rho \mathbf{u} \phi) \mathrm{d}V = \sum_f (\rho \mathbf{u} \phi)_f \cdot \mathbf{A} = \sum_f \phi_f (\rho \mathbf{u})_f \cdot \mathbf{A} = \sum_f \phi_f F_f, \tag{3.24}$$

where F_f is the mass flux through the face f, $F_f = (\rho \mathbf{u}_f) \cdot \mathbf{A}$. In the incompressible case where the density is constant, the following condition on the mass flux must be enforced,

$$\sum_f F_f = 0.$$

The term ϕ_f, the value of ϕ at the faces, in equations (3.23) and (3.24) needs to be determined as only the cell centre values are stored. This can be done, for example, via linear interpolation according to

$$\phi_f = \alpha \phi_P + (1 - \alpha) \phi_N,$$

where ϕ_P is the value in the present cell P and ϕ_N is the value in the neighbouring cell N and α is the ratio between the distance from P to f and P to N as given by $\alpha = a/b$ where a and b are defined as illustrated in Figure 3.8. This is known as Central Differencing (CD) and is second order accurate on structured as well as unstructured meshes. There is a serious drawback of the CD scheme, as it can cause unphysical oscillations when the convection term dominates. If the oscillations are severe, the solution may even diverge.

Instead of interpolating the value ϕ_f on both ϕ_P and ϕ_N as is done in CD, Upwind Differencing (UD) only uses the upwind, or upstream, value. This means that the scheme depends on the direction of the flux. The first order UD scheme is

$$\phi_f = \begin{cases} \phi_P & F \geq 0 \\ \phi_N & F < 0 \end{cases}.$$
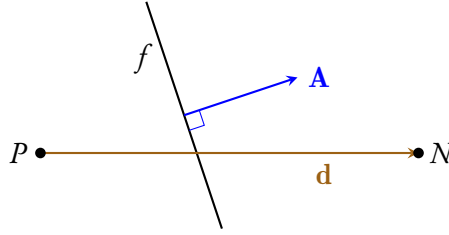
Figure 3.9: A non-orthogonal mesh.

The problem with upwind schemes is that they introduce numerical viscosity into the system. This does increase the stability of the solution compared to the CD schemes, but the stability comes with reduced accuracy. The extra viscosity is undesired as it not only reduces the accuracy but can also dissipate turbulence at a higher rate than what would be physical.

For the important convection of velocity term $\nabla \cdot (\rho \mathbf{u} \otimes \mathbf{u})$, the LUST (Linear-Upwind Stabilised Transport) scheme is used in this thesis. It uses a blend of 75 % CD and 25 % linear-upwind differencing (second order variation of the UD scheme above). The linear-upwind stabilises the CD scheme while maintaining second order behaviour and is particularly successful for LES/DES in external aerodynamics of vehicles according to the OpenFOAM foundation [43]. For the other convection terms in the compressible case, the Gamma scheme is used. The Gamma scheme [62] is a blended scheme where CD is normally used in most of the domain. However, CD can become unbounded. When this occurs, the CD is blended with some UD for stability. In severe unboundedness the scheme uses only UD. There is a parameter that can be specified which affects how much blending should be used and when it should be used. Essentially, this parameter specifies how the scheme should prioritise between accuracy and stability. In this thesis, the parameter is set to maximum stability. For further details, see [62].

For the diffusion term in (3.21), the same basic procedure with (3.22) gives

$$\int_{V_P} \nabla \cdot (\rho \Gamma \nabla \phi) \mathrm{d}V = \sum_f (\rho \Gamma \nabla \phi)_f \cdot \mathbf{A} = \sum_f (\rho \Gamma)_f (\nabla \phi)_f \cdot \mathbf{A}. \qquad (3.25)$$

If the mesh is orthogonal, i.e. the vectors $\mathbf{d}$ and $\mathbf{A}$ in Figure 3.9 are parallel, the face gradient term in (3.25) may be expressed as

$$(\nabla \phi)_f \cdot \mathbf{A} = \frac{\phi_N - \phi_P}{|\mathbf{d}|} |\mathbf{A}|. \qquad (3.26)$$

If the mesh is not orthogonal, which is the norm rather than the exception in real applications, (3.26) needs to be modified to maintain second order accuracy as follows

$$(\nabla \phi)_f \cdot \mathbf{A} = \frac{\phi_N - \phi_P}{|\mathbf{d}|} |\mathbf{A}| + \mathbf{k} \cdot (\nabla \phi)_f,$$

where the second term is the non-orthogonal correction. The differential form, (3.21), of the diffusion term has bounded behaviour. However, boundedness is only preserved on orthogonal meshes as the non-orthogonal correction potentially introduces unboundedness if non-orthogonality is high in the mesh. For severely non-orthogonal meshes, it may therefore be desired to limit or eliminate the correction. There is an additional cost to apply the non-orthogonal correction. In this thesis, the non-orthogonality is applied in Papers B and C, but not in the other papers. The details of the non-orthogonal correction will not be explored here. Instead the interested reader is referred to Jasak [45] which discusses several approaches for the non-orthogonal correction.

To summarise the spatial discretisation, (3.22), (3.24) and (3.25) are plugged into the generic transport equation in (3.21) to obtain

$$\left(\frac{\partial(\rho\phi)}{\partial t}\right)_P V_P + \sum_f \phi_f F_f - \sum_f (\rho\Gamma)_f (\nabla\phi)_f \cdot \mathbf{A} = 0. \tag{3.27}$$

The remaining terms in the governing equations, gradient terms, have in this thesis had CD schemes applied to them.

Time discretisation

As the simulations carried out in this thesis are transient, the spatially discretised generic transport equation in (3.27) needs to be integrated in time as

$$\int_t^{t+\Delta t} \left(\left(\frac{\partial(\rho\phi)}{\partial t}\right)_P V_P + \sum_f \phi_f F_f - \sum_f (\rho\Gamma)_f (\nabla\phi)_f \cdot \mathbf{A} \right) dt = 0, \tag{3.28}$$

where Δt is the length of one time step. Therefore, some time discretisation scheme is needed. In this thesis two approaches are used. In Papers A and B, second order backward differencing is used, while in Papers C–E, a blend of time centred Crank-Nicholson and Euler implicit differencing is used. Both will now be outlined and discussed.

Crank-Nicholson uses the following expressions to calculate the time derivative and time integral of ϕ

$$\left(\frac{\partial(\rho\phi)}{\partial t}\right)_P = \frac{\rho_P^n \phi_P^n - \rho_P^{n-1} \phi_P^{n-1}}{\Delta t}, \tag{3.29}$$

$$\int_t^{t+\Delta t} \phi(t)dt = \frac{1}{2}(\phi^n + \phi^{n-1})\Delta t, \tag{3.30}$$

where $\phi^n = \phi(t + \Delta t)$, or the new time step, and $\phi^{n-1} = \phi(t)$, or the current time step. Inserting (3.29) and (3.30) into (3.28) gives

$$\frac{\rho_P^n \phi_P^n - \rho_P^{n-1} \phi_P^{n-1}}{\Delta t} V_P + \frac{1}{2} \left(\sum_f \phi_f F_f - \sum_f (\rho \Gamma)_f (\nabla \phi)_f \cdot \mathbf{A} \right)^n +$$

$$\frac{1}{2} \left(\sum_f \phi_f F_f - \sum_f (\rho \Gamma)_f (\nabla \phi)_f \cdot \mathbf{A} \right)^{n-1} = 0.$$

This means that the face and cell centred values of ϕ and $\nabla \phi$ as well as the convective and diffusive fluxes for both the current and new times are required. Also, the flux and non-orthogonal correction of the diffusion term must be computed for the new time which means that the Crank-Nicholson scheme requires inner iterations for each time step. The Crank-Nicholson scheme is a second order accurate scheme. The scheme is used in Papers C–E blended with the Euler implicit method outlined below.

The following methods neglect the variation of ϕ_f and $(\nabla \phi)_f$ in time, leaving only the time derivative to be handled by the time discretisation scheme. If (3.29) is used for the time derivative, (3.28) becomes

$$\frac{\rho_P^n \phi_P^n - \rho_P^{n-1} \phi_P^{n-1}}{\Delta t} V_P + \left(\sum_f \phi_f F_f - \sum_f (\rho \Gamma)_f (\nabla \phi)_f \cdot \mathbf{A} \right)^n = 0,$$

which is the Euler implicit method. It is only first order accurate. In Papers C–E, initial tests with the Crank-Nicholson method produced unphysical oscillations. To suppress the oscillations, the Crank-Nicholson scheme was blended with the Euler implicit method.

The time discretisation scheme can be made second order accurate while still neglecting the variation of ϕ_f and $(\nabla \phi)_f$ in time. This is done by raising the order of discretisation used for the time derivative. Backward differencing in time uses

$$\left(\frac{\partial (\rho \phi)}{\partial t} \right)_P = \frac{\frac{3}{2} \rho_P^n \phi_P^n - 2 \rho_P^{n-1} \phi_P^{n-1} + \frac{1}{2} \rho_P^{n-2} \phi_P^{n-2}}{\Delta t},$$

instead of (3.29), turning (3.28) into

$$\frac{\frac{3}{2} \rho_P^n \phi_P^n - 2 \rho_P^{n-1} \phi_P^{n-1} + \frac{1}{2} \rho_P^{n-2} \phi_P^{n-2}}{\Delta t} V_P + \left(\sum_f \phi_f F_f - \sum_f (\rho \Gamma)_f (\nabla \phi)_f \cdot \mathbf{A} \right)^n = 0,$$

This scheme is less computationally expensive than the Crank-Nicholson scheme and has lower memory overhead while both schemes are second order accurate. However, the truncation error is four times larger in the backward differencing scheme [45], so there is a trade-off. The backward differencing scheme is used in Papers A and B.

3.3.5 Solver algorithms

The main solution algorithm used in this thesis is the Pressure Implicit with Splitting of Operators (PISO) algorithm proposed by Issa [63]. The algorithm will only be briefly outlined. The basic idea of the PISO algorithm is that the pressure-velocity system of the Navier-Stokes equations has two complex coupling terms: The non-linear convection term and the linear pressure-velocity coupling. For small time-steps, the pressure velocity coupling should be the stronger of the two. Therefore, a pressure equation is used to perform a few repeated number of pressure corrections without updating the velocities via the momentum equation. For the derivation of the pressure equation and other details, see [45, 57]. For incompressible flow, the PISO algorithm is roughly as follows:

1. Update all derived (turbulent) quantities from the previous values of $\overline{\mathbf{u}}$, F and $\overline{p}$.
2. Solve the discretised momentum equations for the velocity using the previous values for F and $\overline{p}$.
3. Calculate the face fluxes using the new approximate velocity field while maintaining continuity.
4. Solve the pressure equation using the new velocities.
5. If non-orthogonality correction as described in Section 3.3.4 is used, perform the correction here.
6. Correct the approximated velocity field with corrected pressures and repeat from step 3 with the new approximated velocity until the desired number of correction steps have been performed.

For compressible flows, the algorithm is similar. Between step 2 and step 3, the energy equation (3.3) is also solved. In addition, there are density correctors at appropriate points in the algorithm. In Papers C–E, the PIMPLE algorithm is used. The PIMPLE algorithm is a merge of the PISO and the SIMPLE [64] (Semi-Implicit Method for Pressure-Linked Equations) algorithm. The end result is essentially one more layer outside the PISO algorithm described above. The PIMPLE algorithm loops over the PISO algorithm several times. The algorithm can be set to use different convergence criteria on the last and all previous loops (e.g. use a less strict convergence criteria on all but the last loop) and under-relaxation can be used as well. Instead of specifying the number of outer loops manually, the outer loop can be repeated until specified residual levels are reached. The advantage of the PIMPLE algorithm is a higher stability which enables longer time steps but it comes at the price of higher computational cost per time step. If the number of outer loops (the PIMPLE-loops) is set to one, the PIMPLE algorithm reduces to the PISO algorithm.

To solve the linear systems of equations that is the end result of the discussion in Section 3.3, two main strategies were used. In the incompressible simulations in Papers A and B the pressure equation is solved using the Geometric-Algebraic Multi-Grid (GAMG) solver. The idea of the GAMG solver is to generate a quick solution on a mesh with few cells to use as an initial guess
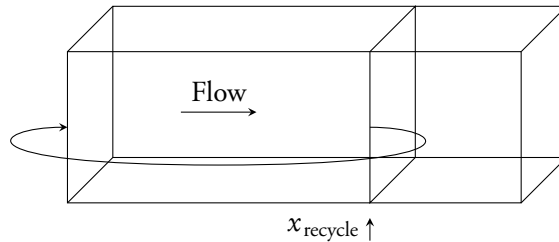
Figure 3.10: Description of the computational domain of the precursor simulation.

on a finer mesh. This reduced the needed total computational cost considerably in Papers A and B. However, the parallel scalability of GAMG was lower, i.e. the maximum number of cores that could be used without diminishing return was lower for the GAMG solver. It was possible to achieve a solution with a shorter wall-time by using more cores with a non-GAMG method, but the total core-hours spent was much larger and it was therefore decided to use the GAMG solver. In the compressible simulations (Papers C–E), using the GAMG method was not beneficial and was therefore not used. The Preconditioned BiConjugate Gradient with the Diagonal Incomplete LU preconditioner (DILUPBiCG) or the so called smooth solver with the Gauss-Seidel smoother were the main methods used when the GAMG method was not in use.

3.3.6 Precursor inlet boundary condition

Papers A and B use a ramped backward-facing step as a model problem. Initially, a prescribed velocity profile taken from the measurements in [40], without any fluctuations was used as inlet BC. This resulted in a laminar boundary layer at the step edge. The interaction between the incoming turbulence in the boundary layer affects the break-up of the K-H vortices shed from the step edge (for the general characteristics of backward-facing step flow, see Section 3.2.2). The lack of turbulence in the boundary layer resulted in an overprediction of the downstream surface pressure fluctuation intensity. While not studying the surface pressure fluctuations specifically, this effect was demonstrated by Aider et al. [65]. They also demonstrated that simple synthetic turbulence-generating inlet BCs are also insufficient as the turbulence tends to not survive long enough distances. Instead, high quality turbulence is needed at the inlet.

A method for generating a high quality turbulent boundary layer of a desired thickness has been developed by Lund et al. [66] and works as follows: An auxiliary simulation, called precursor simulation, is used. The sole purpose of the precursor simulation is to generate the inlet BC for the main simulation. The precursor simulation contains flow over a flat plate. It generates its own inlet BC by mapping the re-scaled velocity field from a point downstream x_{recycle} back to the inlet (of the precursor simulation). This is illustrated in Figure 3.10. Remember that the thickness of the boundary layer δ over a flat plate grows as it travels downstream (see
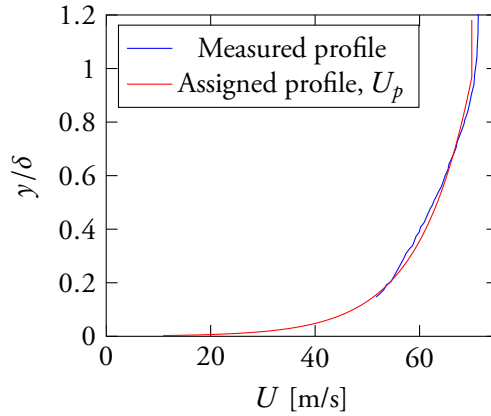
Figure 3.11: Mean streamwise velocity profile used for scaling purposes in the precursor sim-
ulation.

Section 3.2.1). If the velocity is not re-scaled, δ would keep growing as time passed in the
simulation. The purpose of the re-scaling is to keep δ at the desired value.

Unfortunately, when the work on Paper A was carried out, this BC was not implemented in
OpenFOAM. However, there existed a similar BC for channel flow. This BC does not perform
the described scaling as its purpose is to generate a similar BC for fully developed channel flow.
Due to time constraints, only a simplified version of the Lund BC was implemented at first.
The difference compared to the full Lund BC lies in the scaling done when recycling the flow.
In the version implemented by the author an assumed, or prescribed, mean streamwise velocity
profile U_p is used.

$$U_p = A\log(y) + B,$$

where A and B were fitted to the measured mean streamwise velocity profile when there was no
obstacle in the wind tunnel in [40]. Both the measured and the assigned profile U_p is shown
in Figure 3.11.

The scaling is done as

$$u_{\text{scaled}} = \frac{U_p}{\langle u_{\text{recycle}} \rangle} u_{\text{recycle}},$$

where u_{recycle} is the streamwise velocity component sampled at the downstream location x_{recycle}
as indicated in Figure 3.10, $\langle u_{\text{recycle}} \rangle$ is the spanwise mean of u_{recycle} for one row of cells and
u_{scaled} is the scaled result that is recycled back to the inlet of the precursor simulation. Neither
the wall-normal nor the spanwise velocity component is scaled.

This method does not preserve the physical properties of the turbulent boundary-layer to the
same extent as the method developed by Lund et al. [66]. Nevertheless, since the computa-
tional effort to fully resolve the turbulent boundary layer without the aid of wall functions
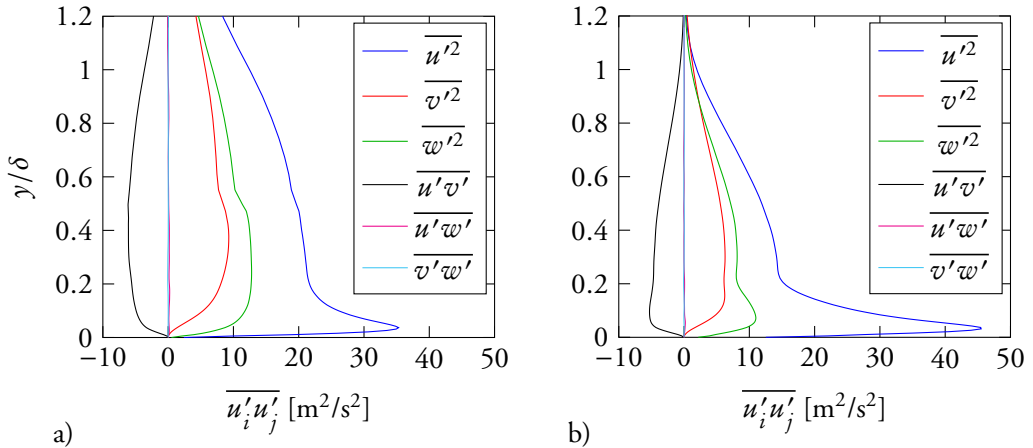
Figure 3.12: Mean Reynolds stress distribution in the inlet BC of the main simulation using a) the simplified Lund (used in Paper A) method and b) the full Lund method (used in Paper B).

would have been too large, it was deemed that this implementation should still provide turbulence in the boundary layer that is realistic enough to create useful results. After the work in Paper A was carried out, another researcher unrelated to this work had implemented the Lund BC in OpenFOAM and kindly provided the implementation for comparison[2]. Instead of spending time to implement the full Lund method a second time, the provided implementation was used in Paper B. The resulting Reynolds stresses of the inlet BC generated by both the simplified and full methods that were used for Papers A and B are given in Figure 3.12. Close to the wall, it appears that the only significant difference is a lower peak value in $\overline{u'^2}$ by about 30 % in the simplified method. Further from the wall the Reynolds stresses in the simplified method decay at a lower rate as the distance to the wall increases. In the full method the Reynolds stresses are small at $y/\delta = 1$ while they are still quite significant in the simplified method. Note that the boundary layer thickness is fixed to the same value in Figure 3.12a and b, i.e. $\delta = 0.99U_\infty$. This is enforced by the BC.

Figure 3.13 gives a comparison between the effects of the two BC methods have on the streamwise distribution on the p_{rms} value downstream of the step in Paper A. It appears that both methods produce similar end results. The insensitivity to the differences in Reynolds stress levels at the inlet as observed in Figure 3.12 is believed to have three main reasons. First, what appears to be most important is that the turbulence has realistic physical structure. This is the result of the work of Aider et al. [65]. The simplified Lund method is capable of creating realistic turbulent structures, albeit at slightly different levels than the full Lund method. The similarities in proportion between the different components between Figures 3.12a and b indic-

---

[2]Joachim Hodara at Georgia Institute of Technology is gratefully acknowledged for sharing his implementation of the Lund inlet BC.
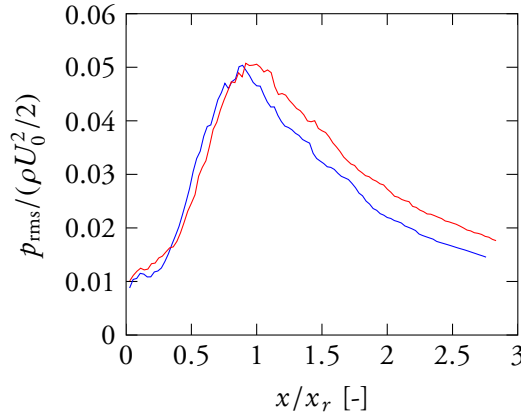
Figure 3.13: Streamwise distribution of r.m.s. fluctuating pressure behind the step in Papers A and B. Curves: (——) is the simplified inlet BC implemented by the author and (——) is the full Lund BC as implemented by Hodara.

ate this. Second, the most important part of the interaction between the turbulent boundary layer and the shear layer downstream of the backward-facing step is between the turbulence in the lower part of the turbulent boundary layer and the shear layer. In the lower part of the boundary layer the difference is only about 30 % in one of the components compared to several times larger at $y/\delta = 1$. Third, due to the geometry with the backward-facing step being located at the end of the ramp, the inlet is placed a fairly long distance ($L_x = 12.5h = 16.67\delta$ where h is the step height and L_x the distance from the inlet to the step) from the step itself. This means that the turbulence has some time to develop to a more physical state inside the main simulation. In summary, for the simulations carried out in Papers A and B, there is no significant effect on the end result depending on whether the simplified or the full Lund method is used in the inlet BC.

3.4 PROPER ORTHOGONAL DECOMPOSITION

The Proper Orthogonal Decomposition (POD) is a post-processing tool that produces a modal decomposition of a given set of data. It was first introduced to the context of turbulent flows by Lumley [67]. In other fields of science, the method is known as Karhunen-Loève decomposition, principal components analysis, singular systems analysis or singular value decomposition [68]. For simplicity, consider some scalar quantity $u(x,t)$ in one dimension that varies with time. Applying the POD-procedure produces a representation of $u(x,t)$ on the following form

$$u(x,t) = \sum_k a_k(t)\phi_k(x), \qquad (3.31)$$

where $\phi_k(x)$ are eigenmodes and $a_k(t)$ are the corresponding time coefficients. The eigenmodes and time coefficients in (3.31) are computed from a series of snapshots of $u(x, t)$. While in this thesis, the snapshots are obtained from numerical simulations, they can equally well come from measurements. The eigenmodes $\phi_k(x)$ are computed such that the quantity

$$\frac{\langle |(u, \phi)|^2 \rangle}{||\phi||^2} \tag{3.32}$$

is maximised. In (3.32) $\langle \cdot \rangle$ denotes ensemble average, $(\cdot, \cdot)$ and $|| \cdot ||$ denotes an appropriate inner product and norm for the $L^2(\Omega_x)$ space where Ω_x is the domain of interest. By applying variational calculus to the maximisation of (3.32), the problem reduces to an eigenvalue problem [68]

$$\int_{\Omega_x} \langle u(x, t) \otimes u(x', t) \rangle \phi(x') \mathrm{d}x' = \lambda \phi(x). \tag{3.33}$$

Equation (3.33) is known as a Fredholm equation of the second kind. The kernel of (3.33) is a form of an ensemble averaged auto-correlation tensor:

$$\langle u(x, t) \otimes u(x', t) \rangle = R(x, x'; t).$$

In the solution of the eigenvalue problem in (3.33), one obtains a set of eigenvalues λ_k each corresponding to an eigenmode $\phi_k(x)$. If $u(x, t)$ is a turbulent velocity field, then the eigenvalues λ_k represent twice the kinetic energy in the corresponding mode $\phi_k(x)$ [68]. The eigenvalues are ordered in descending order $\lambda_k > \lambda_{k+1}$. The POD eigenmodes provide the optimal basis in the sense that energy convergence is more rapid than for any other basis for a given number of modes. This means that the first modes are the most energetic modes which also often are those that identify coherent structures in the flow.

While it is most common in fluid mechanics to apply the POD procedure to the velocity field, the procedure can be applied to any field variable. For example, the POD procedure applied to OH-chemiluminescence signals has revealed flame dynamics in swirling flames in [69, 70]. In Paper D, the POD procedure is applied to both the velocity field and the pressure field. Other examples where the POD procedure has been applied to the pressure field can be found in [71–73].

In Section 4.3 eigenvectors and modes are described for structural dynamics. While they are related, there are some crucial differences. In the modal approach used in structural dynamics, the eigenmodes are computed from the governing equations while the eigenmodes in POD are computed purely from observations of $u(x, t)$. For this reason, the POD eigenmodes are sometimes called empirical eigenmodes. The meaning of the eigenvalues is different. In POD it represents the energy content while in structural dynamics it represents the eigenfrequency. However, the time coefficients of certain POD modes may show a strong periodicity. In particular it is common to have two modes that are coupled as $a_k(t) \approx A_0 \sin(\omega t)$ and $a_{k+1}(t) \approx A_0 \sin(\omega t + \pi/2)$.

The eigenvalue problem (3.33) is of the dimension $N \times N$, where N is the number of discretisation points used to discretise the domain Ω_x. If CFD simulations are used to obtain $u(x, t)$ (as in this thesis), this tends to mean a large N, even if only a 2D-plane is extracted and used as Ω_x. Consequently, solving the eigenvalue problem would become computationally expensive. To reduce the computational expense, Sirovich's method of snapshots [74] is used. This method recasts the problem into the smaller size of $M \times M$, where M is the number of snapshots of $u(x, t)$ that is used. Since it is usually not needed more than in the order of thousands snapshots, M is typically much smaller than N. The recast eigenvalue problem is [75]

$$
\begin{bmatrix} b_{11} & \cdots & b_{1M} \\ \vdots & \ddots & \vdots \\ b_{M1} & \cdots & b_{MM} \end{bmatrix} \begin{bmatrix} c_{11} \\ \vdots \\ c_{M1} \end{bmatrix} = \lambda \begin{bmatrix} c_{11} \\ \vdots \\ c_{M1} \end{bmatrix}, \quad b_{mn} = \int_{\Omega_x} u(x, t_m) u(x, t_n) \mathrm{d}x, \qquad (3.34)
$$

where $u(x, t_n)$ is the n-th snapshot of $u(x, t)$. Let the eigenvectors to (3.34) be $\mathbf{c}^k = \begin{bmatrix} c_1^k \cdots c_M^k \end{bmatrix}^T$ and the eigenvalues λ_k. Then the k-th eigenmode to the original problem is

$$
\phi_k(x) = \frac{1}{\lambda_k M} \begin{bmatrix} c_1^k & \cdots & c_M^k \end{bmatrix} \begin{bmatrix} u(x, t_1) \\ \vdots \\ u(x, t_M) \end{bmatrix}. \qquad (3.35)
$$

For the discretised problem, $u(x, t_n)$ is given at N different locations, $u(x_j, t_n)$ where $j = 1, \cdots, N$. Thus, the discretised version of (3.35) becomes [75]

$$
\begin{bmatrix} \phi_1(x_1) & \cdots & \phi_1(x_N) \\ \vdots & \ddots & \vdots \\ \phi_M(x_1) & \cdots & \phi_M(x_N) \end{bmatrix} = \frac{1}{M} \begin{bmatrix} \frac{c_1^1}{\lambda_1} & \cdots & \frac{c_M^1}{\lambda_1} \\ \vdots & \ddots & \vdots \\ \frac{c_1^M}{\lambda_M} & \cdots & \frac{c_M^M}{\lambda_M} \end{bmatrix} \begin{bmatrix} u(x_1, t_1) & \cdots & u(x_N, t_1) \\ \vdots & \ddots & \vdots \\ u(x_1, t_M) & \cdots & u(x_N, t_M) \end{bmatrix}.
$$

Finally, the time coefficients are then given by

$$
a_k(t_n) = \sum_{j=1}^{N} \phi_k(x_j) u(x_j, t_n).
$$

For further details on POD, the interested reader is referred to [67, 68, 74, 75].

4 Structural response

THIS CHAPTER discusses methods used to predict the vibration of thin panel structures exposed to a pressure load. Simulations of the response are performed in Papers A and E. As the structures simulated in this thesis are thin panel structures, they are suitable objects for thin plate theory, which will be briefly introduced in Section 4.1. This is followed by a very brief description of the finite element method in Section 4.2. The finite element method is the numerical method used in the response simulations. The technique of modal reduction that is used to reduce the computational effort is then described in Section 4.3. The following Section (4.4) covers the random response analysis used in Paper E. Some of the statistical measures described in Section 4.4 are also used in other papers. Finally, there is a section about damping (Section 4.5) and a section that describes the fluid-structure coupling that is used in this thesis (Section 4.6).

4.1 PLATE THEORY

The basic design of an aircraft surface skin panel structure is illustrated in Figure 2.2. The thin outer surface can be made of aluminium or composite material that is attached to an array of stringers and ribs. Figure 2.2 illustrates the flat panel designs used in the ACOUFAT project [25]. As aircraft generally have a cylindrical shape, the skin surface panels of real aircraft are curved. In Paper A, the response of a flat rectangular aluminium sheet attached with many fasteners along its edges is investigated. This sheet represents one bay of the outer skin surface of an aircraft. One of the panel structures from the ACOUFAT project [25] is simulated in Paper E.

The thin sheets forming the skin surface panel structure lends itself very well to the use of plate theory. There are two plate theories that have a wide-spread adoption: the Kirchhoff-Love theory and the Mindlin-Reissner theory. The Kirchhoff-Love theory uses the following assumptions:

1. The plate is thin.
2. The plate is linear-elastic.
3. Deflections and slopes are small.
4. Straight lines normal to the middle surface before deformation remain straight and normal to that surface after deformation.
5. The normal stresses in the direction transverse to the plate can be disregarded.

The equivalent assumptions are made in the Euler-Bernoulli beam theory, which the Kirchhoff-Love plate theory can be seen as an extension of. The Mindlin-Reissner theory is a more complex plate theory that handles thick plates by taking into account the shear deformations through the thickness of the plate. This is done by relaxing assumption four into: Straight lines normal to the middle surface before deformation remain straight. The analogous beam theory to the Mindlin-Reissner plate theory is the Timoshenko beam theory. More on plate theory may be found in [76, 77]. The aluminium sheets in this thesis, as well as many outer skin surfaces on aircraft, are sufficiently thin for the simpler Kirchhoff-Love theory, which is therefore used in Paper A. In Paper E, the choice of plate theory is automatically decided by the software. Furthermore, the deflections in this thesis are small enough to use simple linear plate theory. As discussed in Section 2.2, this is not necessarily true for surface skin panels on aircraft in general.

4.2 FINITE ELEMENT METHOD

In this thesis, Finite Element (FE) formulations of the plate theories are used. The FE software used in Paper A is the in house open-source software package CALFEM [78] which includes a Kirchhoff-Love plate element. The specific element routine used in Paper A, however, is an unpublished routine that extends the published plate element to support a consistent mass matrix and is isoparametric. Since all elements in Paper A has its edges along the coordinate axis and the computational mesh is fine, similar results should be obtained if the published plate element is used together with a lumped mass matrix. In Paper E, the commercial software Abaqus [79] is used. In Abaqus, the model is meshed with a general four-node shell element S4R which automatically determines if the Kirchhoff-Love theory or the Mindlin-Reissner theory is to be used.

It is not necessary to use the FE method in order to use plate theory. The Kirchhoff-Love plate theory can be used to develop simple analytical single degree-of-freedom (SDOF) models and multi degree-of-freedom (MDOF) models directly. This is done and used in the ESDU design guidelines [1]. The FE method was chosen for two reasons. First, the complicated time and spatial distribution of the load extracted from the CFD-simulation can easily be applied to the structure with the FE method. Second, the FE method is a very powerful general tool that can handle complex shapes and materials as well as non-linear response as discussed in Chapter 2.

For the aluminium sheet in Paper A it should be relatively easy to formulate a model that would capture the dynamical properties of the sheet using plate theory directly. For the ACOUFAT panel structure in Paper E this is much more complicated. Since real-life structures tend to be more like the more complicated ACOUFAT panel, it is desired to investigate the structural response with more powerful and general methods.

The FE discretisation produces the following system of equations

$$\mathbf{M}\ddot{\mathbf{a}}(t) + \mathbf{C}\dot{\mathbf{a}}(t) + \mathbf{K}\mathbf{a}(t) = \mathbf{p}(t), \tag{4.1}$$

where $\mathbf{M}$ is the mass matrix, $\mathbf{C}$ is the damping matrix, $\mathbf{K}$ is the stiffness matrix, $\mathbf{a}(t)$ is the nodal displacements vector, $\mathbf{p}(t)$ is the nodal forces from the pressure load and the dot in $\dot{\mathbf{a}}(t)$ indicates time derivative. The derivations and methods used to form these matrices are not covered here as it would take considerable space to present. In particular, the FE-formulation of the plate theory is rather lengthy. The interested reader is instead directed to a textbook on the FE-method such as [80] or [81], the CALFEM manual [78] or the Abaqus manual [79].

4.3 MODAL REDUCTION

If the structure is lightly damped, a reduced order model can be derived as follows. First study the free vibration of the undamped system ($\mathbf{C} = \mathbf{0}, \mathbf{p}(t) = \mathbf{0}$) with n degrees-of-freedom.

$$\mathbf{M}\ddot{\mathbf{a}}(t) + \mathbf{K}\mathbf{a}(t) = \mathbf{0}. \tag{4.2}$$

Assume a solution of the form

$$\mathbf{a}(t) = \boldsymbol{\phi}q(t), \quad q(t) = A\cos(\omega t) + B\sin(\omega t), \tag{4.3}$$

where $\boldsymbol{\phi}$ is a column matrix. This gives

$$\ddot{\mathbf{a}}(t) = -\omega^2\boldsymbol{\phi}q(t) = -\omega^2\mathbf{a}(t). \tag{4.4}$$

Inserting (4.4) into (4.2) gives

$$(\mathbf{K} - \omega^2\mathbf{M})\boldsymbol{\phi}q(t) = \mathbf{0}.$$

If $q(t) = 0$, then $\mathbf{a}(t) = \mathbf{0}$, i.e. no motion. Since this condition is fairly uninteresting, assume $q(t) \neq 0$, which gives

$$(\mathbf{K} - \omega^2\mathbf{M})\boldsymbol{\phi} = \mathbf{0}. \tag{4.5}$$

Once again, disregard $\boldsymbol{\phi} = \mathbf{0}$ as it implies no motion. The remainder has non-trivial solutions when

$$\det(\mathbf{K} - \omega^2\mathbf{M}) = 0. \tag{4.6}$$

Solving the eigenvalue problem (4.6) gives the n eigenfrequencies $\omega_1, \ldots, \omega_n$. If the eigenfrequencies are inserted into (4.5), then the corresponding eigenmodes $\boldsymbol{\phi}_1, \ldots, \boldsymbol{\phi}_n$ can be computed. Consequently, $q_1, \ldots, q_n$ are the modal coordinates. The obtained eigenfrequencies and eigenmodes can be used to transform the original system of equations (4.1) into

$$\tilde{\mathbf{M}}\ddot{\mathbf{q}}(t) + \tilde{\mathbf{C}}\dot{\mathbf{q}}(t) + \tilde{\mathbf{K}}\mathbf{q}(t) = \tilde{\mathbf{p}}(t), \tag{4.7}$$

$$\tilde{\mathbf{M}} = \mathbf{\Phi}^T\mathbf{M}\mathbf{\Phi}, \quad \tilde{\mathbf{C}} = \mathbf{\Phi}^T\mathbf{C}\mathbf{\Phi}, \quad \tilde{\mathbf{K}} = \mathbf{\Phi}^T\mathbf{K}\mathbf{\Phi}, \quad \tilde{\mathbf{p}}(t) = \mathbf{\Phi}^T\mathbf{p}(t).$$

$$\mathbf{a}(t) = \mathbf{\Phi}\mathbf{q}(t), \quad \mathbf{\Phi} = [\boldsymbol{\phi}_1 \cdots \boldsymbol{\phi}_n], \quad \mathbf{q}(t) = [q_1(t) \cdots q_n(t)]^T,$$

The $\tilde{\mathbf{M}}$ and $\tilde{\mathbf{K}}$ matrices are now diagonal. If a diagonal $\tilde{\mathbf{C}}$ is provided as well by the transformation, the system of equations in (4.7) becomes uncoupled. With a diagonal $\tilde{\mathbf{C}}$, the k-th row of (4.7) can be rewritten in standard form

$$\ddot{q}_k(t) + 2\zeta_k\omega_k\dot{q}_k(t) + \omega_k^2 q_k(t) = \frac{p_k(t)}{m_k}, \quad k = 1, \dots, n, \tag{4.8}$$

where ζ_k and m_k is the diagonal element of the k-th row of $\tilde{\mathbf{C}}$ and $\tilde{\mathbf{M}}$, respectively, and p_k is the k-th row of $\tilde{\mathbf{p}}$. ζ_k is known as the modal damping ratio. By inserting all $q_k(t)$ determined using (4.8) into $\mathbf{a}(t) = \mathbf{\Phi}\mathbf{q}(t)$ the physical displacements $\mathbf{a}(t)$ are recovered.

Solving n uncoupled equations is much faster than solving n coupled equations. On the other hand, the eigenfrequencies and the eigenmodes have to be determined first. For many kinds of structures, the response is dominated by just a few modes that have the lowest eigenfrequencies. In such cases, the contributions of only the modes with the lowest frequencies need to be considered, reducing the number of equations in (4.7). This is exploited in this thesis. From here, two different approaches to solve the reduced set of equations are used in this thesis. In Paper A, the reduced set of equations in (4.8) are solved directly using the time-stepping method developed by Newmark [82]. The values of the two parameters used in Newmark's method are $\gamma = 1/2$ and $\beta = 1/4$, which corresponds to the average acceleration method. For a more modern and convenient description of Newmark's method, as well as a more detailed treatment of modal reduction and the dynamics of structures, see [83]. In Paper E, random response analysis, which is a frequency domain formulation, is used instead and this is the topic for Section 4.4.

4.4 RANDOM RESPONSE ANALYSIS

In this thesis, the loads that excite the exposed structures have its origin in turbulent flow. As mentioned in Section 3.1, turbulent flows tend to be irregular, random and chaotic. Therefore, as an alternative to modelling the response to the specific deterministic time series of the load simulated with CFD, one can instead use the CFD simulation to estimate the statistical properties of the load and perform a random response analysis. In this section, the random response analysis method is described. First some important statistical tools used to characterise random processes will be introduced and this is then followed by the random response analysis method.

4.4.1 Random processes

A random process is used to describe measurements or phenomena that are to some degree random or unpredictable. An example of a random process could be time series measurements of wind speed. From a weather forecast or a measurement series taken a moment ago, we may expect a certain mean wind speed and a certain strength in the wind gusts. That is, we know some properties of the random process. However, we cannot know what the actual measured values will be before we perform the measurement. This means that the process can only be characterised in a statistical sense. This section is only an introduction to the subject of stationary random processes. For a more thorough coverage on the subject, see for example [84].

When performing random response analysis, two important assumptions about the process are used. First, the process is assumed to be stationary; the statistical properties of the process must not vary with time. Note that the process itself may vary with time. The process may have a strong periodicity, like the change in day and night temperature, but then the periodicity may not change with time. For pressure loading on the outside skin of an aircraft, this means that an entire flight cycle from take-off to landing is not stationary. However, certain stages of the flight may be. Second, the process is assumed to be ergodic. A process is ergodic if the mean of the statistical properties of several realisations of the same process are the same as the time mean of each realisation. This means that all statistical properties can be accurately estimated from one single realisation of the process.

Here follow a few definitions of statistical measures. The mean value $E[x]$ of a random process $x(t)$ is

$$E[x] = \lim_{T \to \infty} \frac{1}{T} \int_T x(t) \mathrm{d}t,$$

where T is the averaging time. The variance σ_x^2 of $x(t)$ is

$$\sigma_x^2 = E[(x - E[x])^2] = E[x^2] - E[x]^2.$$

In this thesis, the random process in question will often have a zero mean ($E[x] = 0$) or will have its mean subtracted. An example of this is that we will often study the pressure fluctuations by subtracting the mean pressure. When $E[x] = 0$, the variance reduces to the mean square value

$$\sigma_x^2 = E[x^2].$$

As an alternative to the variance, the root-mean-square (r.m.s.) value σ_x is also used which is defined as

$$\sigma_x = \sqrt{\sigma_x^2}.$$

The unit of the r.m.s. value is the same as the unit of $x(t)$, whereas the unit of variance is in the unit of $x^2(t)$.

Assume that $x(t)$ is stationary. Then the auto-correlation function $R_{xx}(\tau)$ is

$$R_{xx}(\tau) = E[x(t)x(t + \tau)] - E[x]^2. \tag{4.9}$$

This function has the following important properties, assuming $x(t)$ is real,

$$R_{xx}(0) = \sigma_x^2, \quad R_{xx}(\tau) = R_{xx}(-\tau), \quad |R_{xx}(\tau)| \le R_{xx}(0).$$

The auto-correlation function is a measure of the similarity between observations taken at different time points separated by the time τ. Note that since $x(t)$ is stationary, $R_{xx}(\tau)$ is independent of t and is therefore a function of the correlation time τ only. If $x(t)$ changes its values slowly with t, $R_{xx}(\tau)$ will decay from its maximum value at $R_{xx}(0)$ slowly and if $x(t)$ changes its value quickly with t, $R_{xx}(\tau)$ will decay from its maximum value at $R_{xx}(0)$ quickly. If there is a strong periodicity in $x(t)$ with the period T_0, $R_{xx}(\tau)$ will be close to $\pm R_{xx}(0)$ when τ is an integer multiple of $T_0/2$.

Similarly to the auto-correlation, the cross-correlation function $R_{xy}(\tau)$ between two stationary processes $x(t)$ and $y(t)$ is defined as

$$R_{xy}(\tau) = E[x(t)y(t + \tau)] - E[x]E[y].$$

As an example, consider a car driving down the road. The vibration in the front axle is $x(t)$ and the rear axle is $y(t)$. This means that $y(t) = x(t + t_0)$ where t_0 is the time for the car to travel the distance between the two axles. Then the cross-correlation function will have a high positive value at $\tau = t_0$.

Normalised auto-correlation and cross-correlation functions are also used. These are given by

$$r_{xx}(\tau) = \frac{R_{xx}(\tau)}{\sigma_x^2}, \quad r_{xy}(\tau) = \frac{R_{xy}(\tau)}{\sigma_x \sigma_y}.$$

This limits the normalised correlation functions to $-1 \le r_{xx}(\tau) \le 1$ and $-1 \le r_{xy}(\tau) \le 1$.

The Power Spectral Density (PSD) S_{xx} of a random process $x(t)$ is the Fourier transform of $R_{xx}(\tau)$

$$S_{xx}(f) = \int_{-\infty}^{\infty} R_{xx}(\tau)e^{-i2\pi f \tau}\mathrm{d}\tau.$$

The PSD gives the frequency content of the random process $x(t)$. For example, the common white noise process contains all frequencies at the same strength ($S_{xx}(f) = S_{xx}(0)$) and is completely uncorrelated between samples. This gives an auto-correlation function that is $R_{xx}(\tau) = \delta(\tau)$ where $\delta(\tau)$ is the Dirac delta function. On the other end, the signal $x(t) = \sin(2\pi f_0 t)$ has a periodic $R_{xx}(\tau)$ and a PSD with only delta spikes at $\pm f_0$: $S_{xx}(f) = \delta(f - f_0) + \delta(f + f_0)$.

Analogous to the cross-correlation function $R_{xy}(\tau)$, the Cross-Power Spectral Density (CPSD) is defined as the Fourier transform of $R_{xy}(\tau)$

$$S_{xy}(f) = \int_{-\infty}^{\infty} R_{xy}(\tau)e^{-i2\pi f \tau}\mathrm{d}\tau.$$

The CPSD is a complex valued function with the properties

$$S_{xy}(f) = S_{yx}^*(f) = S_{yx}(-f),$$

where the star indicates complex conjugate. The CPSD function is also used in the normalised form as given by

$$\check{S}_{xy}(f) = \frac{S_{xy}(f)}{\sqrt{S_{xx}(f)S_{yy}(f)}},$$

thus limiting the magnitude of $\check{S}_{xy}(f)$ to $|\check{S}_{xy}(f)| \leq 1$.

How to obtain a good estimate of $S_{xx}(f)$ (and $S_{xy}(f)$) is not a trivial question. The naive way would perhaps be to take a realisation of the random process in question $x(t)$, sample it at discrete times, compute an estimate of its auto-correlation function $R_{xx}(\tau)$ from the definition in (4.9) and then finally use the Discrete Fourier Transform (DFT) given by

$$\mathcal{G}(f) = \sum_{t=0}^{N-1} g(t)e^{-i2\pi f t}, \tag{4.10}$$

where $g(t)$ is any signal in time sampled at N discrete times. Unfortunately, this would typically give a poor estimate. Also, computing the DFT from its definition (4.10) is very slow. Instead, a Fast Fourier Transform (FFT) algorithm is used. The details of the FFT will not be covered here, instead the interested reader is referred to [85].

Instead of first estimating R_{xx} and then using the FFT, the PSD estimate is based on the periodogram

$$\underline{S_{xx}}(f) = \frac{1}{N}\mathcal{X}(f)\mathcal{X}^*(f), \tag{4.11}$$

where N is the number of samples from the realisation of the process $x(t)$, $\mathcal{X}(f)$ is the Fourier transform of $x(t)$ and the underline indicates that $\underline{S_{xx}}(f)$ is an estimate of $S_{xx}(f)$. It can be shown that this is equivalent of the Fourier transform of a good estimator to $R_{xx}(\tau)$ (see for example [84]).

There are two main problems with the periodogram estimator in (4.11): bias and high variance. Both issues are addressed in Welch's method [86] that is used in this thesis for spectrum estimation. The main points of the algorithm are as follows. The bias is the result of only using a finite sequence of something that in the Fourier transform is assumed to be periodic of infinite length. Since the finite sequence that is sampled is unlikely to be perfectly periodic, there will likely be an unnatural jump from the last sample to the first sample. This jump introduces power at other frequencies that are not present in the true process. To reduce the effect of this jump, a windowing function $w(t)$ is multiplied with the sampled signal $x(t)$. The windowing function reduces the values near the beginning and the end of the signal so the jump gets smaller. This gives the modified periodogram

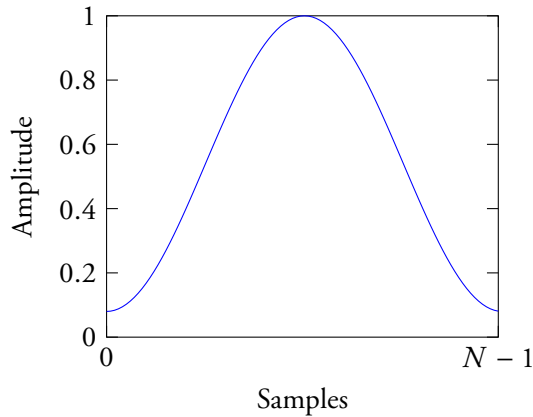$$z(t) = x(t)w(t), \quad \underline{S_{xx}}(f) = \frac{1}{N}\mathcal{Z}(f)\mathcal{Z}^*(f). \tag{4.12}$$

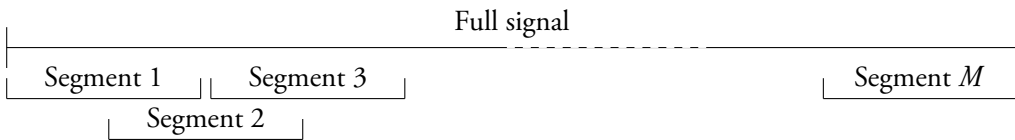**Figure 4.1:** Hamming window for N samples.

Figure 4.2: Illustration of the signal segmentation in Welch's method.

There are many different window functions available with different properties. In this thesis, the Hamming window is typically used. The Hamming window is illustrated in Figure 4.1. The variance issue is dealt with by dividing the sampled signal $x(t)$ into several overlapping segments as illustrated in Figure 4.2. For each segment, the modified periodogram is computed using (4.12) and the resulting $\underline{S_{xx}}(f)$ are averaged over all segments.

4.4.2 Random response

In Paper E, the response of the structure is computed using a random response formulation. The formulation is modal based, which means that the theory presented in Section 4.3 is used. The reduced set of equations (4.8) are solved in the frequency domain. This is done by assuming that the physical, and therefore also the modal projection of the load p_k, is stationary and harmonic

$$p_k = p_{k0}e^{i\omega t}, \tag{4.13}$$

where $\omega = 2\pi f$. This produces a modal response q_k in a similar form

$$q_k = q_{k0}e^{i\omega t}, \quad \dot{q}_k = i\omega q_{k0}e^{i\omega t}, \quad \ddot{q}_k = -\omega^2 q_{k0}e^{i\omega t}. \tag{4.14}$$

Plug in (4.13) and (4.14) into (4.8) to produce

$$(-\omega^2 + i2\zeta_k\omega_k\omega + \omega_k^2)q_{k0} = \frac{p_{k0}}{m_k}.$$

This can be rewritten to

$$q_{k0} = H_k(f)p_{k0}, \quad H_k(f) = \frac{1}{m_k(\omega_k^2 - \omega^2 + i2\zeta_k\omega_k\omega)}, \tag{4.15}$$

where $H_k(f)$ is the complex frequency response function.

In the random response analysis, the loading is defined by the cross-spectral density matrix

$$\mathbf{P}(f) = \begin{bmatrix} P_{11}(f) & P_{12}(f) & \cdots & P_{1n}(f) \\ P_{21}(f) & P_{22}(f) & \cdots & P_{2n}(f) \\ \vdots & \vdots & \ddots & \vdots \\ P_{n1}(f) & P_{n2}(f) & \cdots & P_{nn}(f) \end{bmatrix}, \tag{4.16}$$

where $P_{ab}(f)$ is the CPSD of the load of degrees-of-freedom a and b. This means if the load on all degrees-of-freedom are completely uncorrelated, only the diagonal terms will be present. Similarly to (4.7), $\mathbf{P}(f)$ is projected onto the modes

$$\tilde{\mathbf{P}}(f) = \mathbf{\Phi}^T\mathbf{P}(f)\mathbf{\Phi}.$$

The complex modal response CPSD $\mathbf{Q}(f)$ can then be determined by using the complex frequency response function

$$\mathbf{Q}(f) = \mathbf{H}(f)\tilde{\mathbf{P}}(f)\mathbf{H}^*(f), \quad \mathbf{H}(f) = \begin{bmatrix} H_1(f) & 0 & \cdots & 0 \\ 0 & H_2(f) & \cdots & 0 \\ \vdots & \vdots & \ddots & \vdots \\ 0 & 0 & \cdots & H_m(f) \end{bmatrix},$$

where m is the number of modes included in the analysis. Note that $\mathbf{Q}(f)$ is a matrix like $\tilde{\mathbf{P}}(f)$ which contains the PSDs and CPSDs in generalised coordinates. The response in physical variables can then be computed from

$$\mathbf{A}(f) = \mathbf{\Phi}\mathbf{Q}(f)\mathbf{\Phi}^T = \mathbf{\Phi}\mathbf{H}(f)\mathbf{\Phi}^T\mathbf{P}(f)\mathbf{\Phi}\mathbf{H}^*(f)\mathbf{\Phi}^T.$$

In the $\mathbf{A}(f)$ matrix, the PSD of the response in all degrees-of-freedom and the CPSD of all combinations of the degrees-of-freedom are available. Since the PSD of only a few degrees-of-freedom and none of CPSD combinations are of interest, only those few positions in $\mathbf{A}(f)$ that are desired are actually computed in order to speed up the computation.

The commercial software package Abaqus is used for the random response simulations and more information can be found in its manual [79]. For more information on random response analysis in general, see for example [87].

4.5 DAMPING

The damping of a structure is the effect of energy loss via dissipation. Without damping, a structure that is excited by a load at the resonance frequency would theoretically always reach infinite displacements unless the source of loading was removed. The damping increase stability, both in the physical and the computational world. The sources of the dissipation can be many. For example damping can occur inside the material of the structure due to its microstructure. It can also be caused by friction in joints and due to contact near bolts and screws.

There are accurate and simple ways to obtain the mass **M** and stiffness **K** matrices for many structures. For both the aluminium structures simulated in this thesis, it is enough to know the material properties and the geometry of the sheet. Damping on the other hand, is very difficult to estimate. In this thesis the modal formulation is used. Therefore, one damping value is needed for each of the included modes as demonstrated by (4.8). The first few modes were estimated using the half-power bandwidth method from the pre-existing measurements, while the higher modes were given a fixed value of 1 %.

4.6 FLUID-STRUCTURE COUPLING

The motion of the fluid and the structure is dealt with separately in this thesis. But as a consequence of Newton's third law, the fluid and the structure are coupled; the fluid exerts force on the structure, and vice versa. This is possible to handle with various simulation tools and is called Fluid-Structure Interaction (FSI). In this thesis some of the coupling is neglected. The FE structural response simulation dealt with in this chapter uses the load extracted from the CFD simulation of the flow. The resulting vibration of the structure, however, is not taken into consideration in the simulation of the flow. The flow simulation does take the presence of the rigid structure into consideration by wall BC:s, but not the vibration of the structure. The motivation for this is that the effect on the flow would have been negligible. This means that the problem is only one way coupled. The data from the simulation of the fluid is sent to the simulation of the structure, but not vice versa. The response of the exposed structure are treated in Papers A and E. The response simulations use different methods. For example, in Paper A a time domain method is used while in Paper E a frequency domain method is used. Therefore, there are differences in the coupling procedures.

In Paper A, the coupling method was chosen for simplicity. The reason for this is that the main focus of Paper A is the load prediction rather than investigating different coupling schemes. The pressure load is extracted as the pressure value directly from the CFD-simulation. To avoid the need for an interpolation algorithm, matching meshes are used at the interface of the fluid and the structure domains. For the aluminium sheet in Paper A, this results in a mesh that is finer than it needs to be if one just considers the needs of the structural simulation. This is not an

issue, as the simulation of the structure is still several orders of magnitude less computationally demanding than the simulation of the fluid. As the CFD-software OpenFOAM is a finite volume code, the pressure is given at the cell surface centre. This pressure is assumed to be constant over the whole element and is integrated using the CALFEM element routine to obtain the nodal load vector $\mathbf{p}(t)$ in (4.1). Instead of using a constant load over each element, a more refined interpolation method could have been used. However, the increase in accuracy is deemed to be very small. Also, this would have to be implemented as there is no such implementation presently available in CALFEM.

In Paper E, the panel response is computed using the method given in Section 4.4. The load input from the flow simulation appears in the $\mathbf{P}(f)$ matrix defined in (4.16). Ideally, every exposed degree-of-freedom in $\mathbf{P}(f)$ should have its pressure spectrum and cross-spectrum to all other degrees-of-freedom computed from the CFD simulation. However, the amount of data needed to do this would be vast. Instead, the exposed surface of the panel structure is divided into different sections. There are 64 sections of equal size per bay in an 8 by 8 pattern. Since there are 15 bays arranged in a 5 by 3 pattern, this means there are 960 sections in total. The PSD of the load of each section and the CPSD between each section and all the other sections are computed. Then $\mathbf{P}(f)$ is constructed by table lookup. If both a and b for the component $P_{ab}(f)$ is within the same section, the load is assumed to be fully in phase and the PSD computed for that section is used. If a and b are in different sections, then the corresponding CPSD between those sections are used for $P_{ab}(f)$.

5 Summary of the appended papers

Paper A

This paper investigates the numerical procedure of using CFD for load prediction and then using the predicted load as input to an FE-simulation of the response of an exposed structure. The procedure is tested on a model problem consisting of a thin aluminium sheet that is located downstream of a ramped backward-facing step. The flow past the step induces a load on the aluminium sheet. Transient large eddy simulations are carried out to simulate the load. As inlet BC for the CFD simulations, the simplified Lund method is implemented by the author. The computed load is then used as an input to a response simulation of the aluminium sheet. The paper extends previous studies in mainly three ways. First, it attempts to use the simulated load to provide a response prediction which is not done in previous studies. The load intensities and spectral characteristics are well captured, except that the shedding frequency is overpredicted. The response prediction is reasonably well captured. When the response prediction is seen in the context of design guidelines and other studies where the load is measured, the response prediction can be seen as good. Second, it is a numerical study of the surface pressure fluctuations downstream of a backward-facing step at approximately one order of magnitude higher Reynolds numbers than previous studies. Third, it uses a wall-function for wall treatment. Previous studies on surface pressure fluctuations downstream of a backward-facing step either resolve the turbulent boundary layer in the LES sense or use DES.

The author carried out all simulations, implemented the inlet precursor BC as well as wrote the paper. All other authors assisted in writing the paper as well as giving general supervision of the work. The experimental data used for comparison was provided by E. J. Gutmark.

Paper B

Passive load control in backward-facing step flow by using chevrons.
Johan Nilsson, Robert-Zoltán Szász, Per-Erik Austrell, Ephraim J. Gutmark.
Accepted for publication in: Segalini, A. (ed.), *Proceedings of the 5th International Conference on Jets, Wakes and Separated Flows (ICJWSF2015)*, (2016).
ISBN: 978-3-319-30600-1

The use of chevrons, or serrations, is investigated numerically on the same backward-facing step flow that is studied in Paper A. The aim is that the chevrons should reduce the pressure load on the downstream surface in a similar way that chevrons reduce noise levels in jet nozzles and trailing edge serrations reduce the noise from wing profiles. The serrations are sawtooth-shaped and start at the base of the ramp and gradually grow to the step edge where the height of the serrations is $h/10$. The same CFD methodology is used as in Paper A with one exception: The full Lund method is used as inlet BC instead of the simplified method used in Paper A. Three configurations with chevrons are compared to a baseline configuration without any chevrons. In the vicinity of the mean reattachment point, there is a reduction in low frequency content of the pressure load for two of the three configurations. The general impact of the chevrons on the mean flow is small with a nearly constant reattachment length between the different configurations.

The author carried out all simulations as well as wrote the paper. All other authors assisted in writing the paper as well as giving general supervision of the work.

Paper C

Numerical simulation of surface pressure fluctuations in transonic fence-like flows with high Reynolds number.
Johan Nilsson, Robert-Zoltán Szász, Per-Erik Austrell, Delphine Bard.
Published in the International Journal of Heat and Fluid Flow, **58**, 103–119, (2016).
doi: 10.1016/j.ijheatfluidflow.2015.12.008.

This paper presents large eddy simulations on a transonic test case for acoustic fatigue. The test case is flow past an inclined fence at $\mathrm{Re}_h = 1.6 \cdot 10^6$ and $\mathrm{Ma} = 0.7$ which are realistic operating conditions for an aircraft. The simulations are compared to existing measurements from the ACOUFAT program [25] as well as other sources in the literature on similar flows. Only a segment of the fence flow is modelled using spanwise cyclic BCs. The flow is found to be sensitive in several respects to the geometrical BC imposed. Three different geometrical configurations are therefore investigated. Several aspects of the flow and the pressure load are investigated. Most characteristics of the load are captured. In particular, the cross-spectral densities of the load are captured at a similar level as a semi-empirical model developed by Campos et al. [2].

However, there was a significantly stronger energy concentration around 100 Hz in the pressure spectra in the ACOUFAT measurements [25] compared to the LES simulations performed in the paper. In one of the simulated configurations, a similar concentration appeared, but it was located further downstream compared to the ACOUFAT measurements [25]. The paper is the first numerical study on fence flow to study the surface pressure fluctuations. Also, it performs the study at three orders of magnitude higher Reynolds numbers than previous studies on fence flow as well as at transonic Mach numbers which is not done before.

The author carried out all simulations as well as wrote the paper. All other authors assisted in writing the paper as well as giving general supervision of the work.

Paper D

Three-dimensional aspects of fence flow.
Johan Nilsson, Robert-Zoltán Szász.
Submitted for publication.

In this paper, the same model problem from the ACOUFAT program [25] used for Paper C is once again simulated numerically. This time the entire width of the fence and test-table is simulated compared to only a segment in Paper C. This enables the study of all of the three-dimensional aspects of the flow. The energy concentration at 100 Hz in the pressure spectra that was elusive in Paper C is predicted by the simulations in this paper at the correct frequency and approximately the correct spatial location. By using POD mode decomposition, the three-dimensional nature of the underlying phenomenon is illustrated and it is concluded that the phenomenon cannot be captured in a simulation of only a segment of the fence and test-table. In addition, a second low frequency phenomenon was also illuminated by the POD procedure. The phenomenon appears to be dominated by a movement in the spanwise direction with some resemblance of wake meandering found in the wake of wind turbines. While it is concluded that it cannot be the same mechanism that cause wake meandering behind real wind turbines, it is suggested that it could be a phenomenon similar to the low frequency instability observed by Medici and Alfredsson [88].

The author carried out all simulations as well as wrote the paper. The other author assisted in writing the paper as well as giving general supervision of the work.

Paper E

Numerical response simulation of a panel structure exposed to a numerically simulated load from separated flow.
Johan Nilsson, Per-Erik Austrell, Robert-Zoltán Szász.
Submitted for publication.

The same model problem from the ACOUFAT program [25] used in Papers C and D is also used in this paper. This time the response of the realistic panel structure that is exposed to the load from separated flow downstream of the fence is studied. The load that causes the vibration in the panel structure is extracted from the same set of CFD simulations that is used in Paper D. The main load features, both auto-spectra and cross-spectra compare reasonably well with the ACOUFAT measurements [25]. There is a general overprediction of the load intensity, but not an excessive overprediction. The simulated load is then used as input to a random response simulation using the FEM. When comparing the simulated response to the ACOUFAT measurements [25], the prediction vary with strain gauge location. Several of the strain gauges have a very good prediction, both with respect to which modes are excited and amplitude, but there are also those that are dominated by a different mode compared to the ACOUFAT measurements [25]. The impact of the cross-correlations is investigated by varying the level of correlation artificially. The response is found to be sensitive the correlation level, both with respect to which modes are excited and the amplitude of the excitation.

The author carried out all simulations (including implementing the necessary routines needed to extract the load from the CFD simulations and use it as input to the response simulations) as well as wrote the paper. All other authors assisted in writing the paper as well as giving general supervision of the work.

6 Contributions, conclusions and future work

T HE GENERAL AIM of this thesis is to improve the load and response prediction for acoustic fatigue by using numerical methods in the form of CFD to predict the load. The alternative, experimental measurements, are expensive and time consuming. It is also desired to design for acoustic fatigue early in the design process before any flight testing can be done. Furthermore, current design guidelines have simplifying assumptions limiting their use. Even with favourable conditions and a measured load, they do not achieve a better prediction than a factor of two in the r.m.s. strains [6]. If a detailed load prediction is extracted from CFD, then the well-established tool of the FEM can be used to predict the response without the restrictions from the design guidelines. This idea is tested on two model problems in this thesis. Both are chosen because previous measurements exist on both the flow induced load and the vibrational response of the exposed structure.

6.1 CONTRIBUTIONS

The main innovation or contribution in this thesis can be summarised as:

- Load prediction in separated flows for use in acoustic fatigue is investigated using numerical methods in the form of computational fluid dynamics.

This investigation has resulted in several contributions which are presented in this thesis and are listed below:

- Large eddy simulation of downstream surface pressure fluctuations (i.e. the load) are performed at Reynolds numbers at one to several orders of magnitudes higher than previous numerical studies.
- In Paper E, the load and response simulations are performed at Reynolds and Mach numbers that are realistic for the aircraft industry.

- This thesis extends earlier numerical studies of the load by not just studying the load, but also using the load as input to a response simulation.

- The simulated response compares well enough with existing measurements to be useful predictions.

- The response predictions are achieved without the restrictive and limiting assumptions of design guidelines. Thus being applicable to more complicated structures and to non-linear response.

- This thesis highlights some of the complexities and challenges when trying to compute the downstream surface load using large eddy simulations (in particular, see Paper D).

- It is demonstrated that the large eddy simulations of the load is capable of capturing the cross-spectra of the load. Also, the high importance of the cross-spectra is demonstrated, verifying previous studies.

- The use of serrations along the ramp of a backward-facing step geometry is demonstrated to reduce the load on the downstream surface for a range of frequencies.

6.2 CONCLUSIONS

In Papers A and B, a ramped backward-facing step induces a load on a downstream rectangular aluminium sheet. The Reynolds number is one order of magnitude higher than previous numerical studies on the surface pressure fluctuations downstream of a backward-facing step. This makes the present simulations more realistic than previous studies, although Reynolds and Mach numbers are still lower than realistic conditions for the aircraft industry. In Paper A, important features of the flow and load are predicted with good accuracy. This includes load spectra with the exception of the overpredicted cut-off frequency. It is concluded that the interaction between the turbulence in the turbulent boundary layer and the vortices shed at the step is important for the load intensity on the exposed aluminium sheet. When considering the response prediction in Paper A, it should be noted that the load input is entirely numeric. Considering this, the response prediction is reasonably good. Unfortunately, the existing measurements did not provide any strain data which makes direct comparison with design guidelines and other studies difficult.

In Paper B, a similar flow simulation method as in Paper A is used. The only significant difference is that the full Lund method [66] is used instead of a simplified version of it as inlet BC. In Paper B it is demonstrated that serrations along the ramped backward-facing step can be used to address the issue of acoustic fatigue by reducing the load.

The model problem investigated in Papers C–E is for several reasons more challenging than the model problem in Papers A and B. First, the conditions are realistic for aircraft industry which means higher Reynolds and Mach numbers. It is not possible to use incompressible simulations as in Papers A and B. Second, the exposed structure is more complex and realistic

requiring a more refined model. Third, the flow is more complex. This is highlighted in Paper D, where it is concluded that an important load feature cannot be captured using the quasi 3D method of only simulating a segment with cyclic boundary conditions (which is used in Papers A–C and is common in the literature for similar flow situations). Fourth, the flow conditions were better documented in the model problem used in Papers A and B. The most accurate load prediction in the model problem used in Papers C–E is the result from the fine mesh presented in Paper E. While the load is not as well predicted as in Paper A, the load in Paper E is reasonably well predicted. The mean reattachment length is underpredicted which also contributes to the mismatch in the load. However, the important cross-spectra are well predicted.

The response predictions in Paper E are perhaps the most interesting results of this thesis. After all, the main goal of the numerical load prediction is to create a useful response prediction of the exposed structure. In addition, it is a realistic case, more realistic than the case in Papers A and B both with respect to flow conditions and the exposed structure. The accuracy in the predictions differs between different strain gauges. Some are very accurate, both with respect to which modes are excited and excitation levels, while some are less accurate. The manipulation of the cross-correlation demonstrates the sensitivity to the cross-correlation of the response. That different modes are excited depending on the level of the cross-correlation was already found in the ACOUFAT project [2, 25], but Paper E demonstrates that it can affect the excitation amplitude as well. This highlights the importance of the cross-correlation spectrum.

The predicted r.m.s. strain levels in Paper E are within a factor two on all strain gauges except for one. This is the same accuracy that can be expected from the ESDU design guidelines [1] in favourable conditions and with *known or measured* load intensity. This is important to mention since the response prediction will be much better if we could just apply the correct load. Here the load is simulated and the error in the response includes errors in the load prediction. Another important point is that while the presented method only achieved the same accuracy levels in r.m.s. levels, the method does not have the same limitations that the ESDU design guidelines [1] does. Instead it can handle complex materials and structures as long as it can be modelled using regular FE random response analysis.

6.3 FUTURE WORK

In this thesis, numerical simulations have been carried out and the results have been compared with pre-existing measurements on two model problems. While both sets of measurements have been very useful, they both have their deficiencies. The ramped backward-facing step measurements [40] used in Papers A and B have detailed description of the flow conditions, enabling a good flow and load comparison. However, there were no strain gauges fitted to the aluminium plate making comparison with conventional methods difficult and it was difficult

to determine the properties of the structure from the documentation. For the fence flow measurements in the ACOUFAT project [2, 25] used in Papers C–E, the situation is more or less reversed. There, the exposed structure is well documented with measurements, drawings and simulations and with strain gauges fitted in strategic positions. However, the flow geometry and conditions are not very well described in the measurement reports [25] which makes it difficult to perform numerical simulations of the flow and the load. Therefore, it is suggested that new measurements are performed together, or in direct collaboration, with numerical simulations based on the approach presented in this thesis. This way any gaps or uncertainties from the measurements should be avoided. Ideally, the measurements should include a good flow, load and vibration description of a relevant panel structure at relevant conditions for the aircraft industry.

References

[1] IHS ESDU (2011), *ESDU 72005, The estimation of r.m.s. stress in stiffened skin panels subjected to random acoustic loading.*

[2] Campos, L., Bourgine, A., Bonomi, B. (1999), *Comparison of theory and experiment on aeroacoustic loads and deflections*, Journal of Fluids and Structures **13**(1), 3–35, doi: 10.1006/jfls.1998.0192.

[3] Cunningham, P., Langley, R., White, R. (2003), *Dynamic response of doubly curved honeycomb sandwich panels to random acoustic excitation. Part 2: Theoretical study*, Journal of Sound and Vibration **264**(3), 605–637, doi:10.1016/S0022-460X(02)01211-7.

[4] Ji, M., Wang, M. (2012), *Surface pressure fluctuations on steps immersed in turbulent boundary layers*, Journal of Fluid Mechanics **712**, 471–504, doi:10.1017/jfm.2012.433.

[5] Dietiker, J.F., Hoffmann, K.A. (2009), *Predicting Wall Pressure Fluctuation over a Backward-Facing Step Using Detached Eddy Simulation*, Journal of Aircraft **46**(6), 2115–2120, doi:10.2514/1.43912.

[6] Clarkson, B. (1994), *Review of sonic fatigue technology*, NASA Technical Report CP-4587.

[7] Cunningham, P.R., White, R.G. (2004), *A review of analytical methods for aircraft structures subjected to high-intensity random acoustic loads*, Proceedings of the Institution of Mechanical Engineers, Part G: Journal of Aerospace Engineering **218**(3), 231–242, doi: 10.1243/0954410041872898.

[8] Miles, J.W. (1954), *On Structural Fatigue Under Random Loading*, Journal of the Aeronautical Sciences **21**(11), 753–762, doi:10.2514/8.3199.

[9] Miner, M. (1945), *Cumulative damage in fatigue*, Journal of applied mechanics **12**(3), 159–164.

[10] Powell, A. (1958), *On the Fatigue Failure of Structures due to Vibrations Excited by Random Pressure Fields*, The Journal of the Acoustical Society of America **30**(12), 1130–1135, doi: 10.1121/1.1909481.

[11] Clarkson, B. (1968), *Stresses in skin panels subjected to random acoustic loading*, The Aeronautical Journal of the Royal Aeronautical Society **72**, 1000–1010.

[12] Thompson, A., Lambert, R. (1972), *The estimation RMS stresses in stiffened skin panels subjected to random acoustic loading*, Technical Report Section 5, AGARD-AG-162, Advisory Group for Aerospace Research and Development.

[13] Rudder, F., Plumblee, H. (1975), *Sonic fatigue design guide for military aircraft*, Technical Report AFFDL-TR-74-112, Acoustics and Vibration Associates, Atlanta, Georgia.

[14] Blevins, R. (1989), *An approximate method for sonic fatigue analysis of plates and shells*, Journal of Sound and Vibration **129**(1), 51–71, doi:10.1016/0022-460X(89)90535-X.

[15] White, R. (1978), *A comparison of some statistical properties of the responses of aluminium alloy and cfrp plates to acoustic excitation*, Composites **9**(4), 251–258, doi:10.1016/0010-4361(78)90178-7.

[16] Mei, C., Prasad, C. (1987), *Effects of non-linear damping on random response of beams to acoustic loading*, Journal of Sound and Vibration **117**(1), 173–186, doi:10.1016/0022-460X(87)90443-3.

[17] Reinhall, P., Miles, R. (1989), *Effect of damping and stiffness on the random vibration of non-linear periodic plates*, Journal of Sound and Vibration **132**(1), 33–42, doi:10.1016/0022-460X(89)90868-7.

[18] Green, P., Killey, A. (1997), *Time Domain Dynamic Finite Element Modelling in Acoustic Fatigue Design*, in: Ferguson, N.S., Wolfe, H.F., Mei, C. (eds.), *Proceedings of the Sixth International Conference on Recent Advances in Structural Dynamics*, 1007–1025, University of Southampton.

[19] Hollkamp, J.J., Gordon, R.W., Spottswood, S.M. (2005), *Nonlinear modal models for sonic fatigue response prediction: a comparison of methods*, Journal of Sound and Vibration **284**(3-5), 1145–1163, doi:10.1016/j.jsv.2004.08.036.

[20] Blevins, R., Holehouse, I., Wentz, K. (1993), *Thermoacoustic loads and fatigue of hypersonic vehicle skin panels*, Journal of Sound and Vibration **30**(6), 971–978, doi:10.2514/3.46441.

[21] Miller, B., McNamara, J., Spottswood, S., Culler, A. (2011), *The impact of flow induced loads on snap-through behavior of acoustically excited, thermally buckled panels*, Journal of Sound and Vibration **330**(23), 5736–5752, doi:10.1016/j.jsv.2011.06.028.

[22] Mignolet, M.P., Przekop, A., Rizzi, S.A., Spottswood, S.M. (2013), *A review of indirect/non-intrusive reduced order modeling of nonlinear geometric structures*, Journal of Sound and Vibration **332**(10), 2437–2460, doi:10.1016/j.jsv.2012.10.017.

[23] Cunningham, P., White, R. (2003), *Dynamic response of doubly curved honeycomb sandwich panels to random acoustic excitation. Part 1: Experimental study*, Journal of Sound and Vibration **264**(3), 579–603, doi:10.1016/S0022-460X(02)01210-5.

[24] Tougard, D. (1993), *ACOUFAT: Final technical report*, Document AERO 0025-1079 / Rept 6 / 1, ACOUFAT Project.

[25] Tougard, D. (1995), *Acoustic Fatigue and Related Damage Tolerance of Advanced Composite and Metallic Structures (ACOUFAT)*, in: Hernandez, J. M. M. (ed.), *Advances in Acoustics Technology*, 83–195, Wiley, Chichester, ISBN 0-471-95149-8.

[26] Campos, L. (1991), *On the correlation of acoustic pressures induced by a turbulent wake on a nearby wall*, ACOUFAT Project.

[27] Bourgine, A. (1992), *Wall pressure fluctuations and induced vibrations on a plane panel downstream a flap in transonic mach number range*, Document AERO 0025-1079 / D16 / 1, ACOUFAT Project.

[28] Onera (1991), *Definition of transonic wind tunnel test*, Document AERO 0025-1079 / D6 / 1, ACOUFAT Project.

[29] Bayerdörfer, G. (1992), *Wind tunnel- and progressive wave tube tests to determine loading actions and structural response of a stiffened al-panel*, Document AERO 0025-1079 / D12 / 1, ACOUFAT Project.

[30] *Comparison between calculated and tested results for the aluminium panel inside the wind tunnel and the progressive wave tube*, Document AERO 0025-1079 / D17 / 1, ACOUFAT Project.

[31] Wagner, C., Hüttl, T., Sagaut, P. (2007), *Large-Eddy Simulation for Acoustics*, Cambridge University Press, New York, ISBN 978-0-521-87144-0.

[32] Reynolds, O. (1883), *An Experimental Investigation of the Circumstances Which Determine Whether the Motion of Water Shall Be Direct or Sinuous, and of the Law of Resistance in Parallel Channels*, Philosophical Transactions of the Royal Society of London **174**, 935–982, doi:10.1098/rspl.1883.0018.

[33] Richardson, L. (1922), *Weather Prediction by Numerical Process*, Cambridge University Press.

[34] Kolmogorov, A. (1941), *The Local Structure of Turbulence in Incompressible Viscous Fluid for Very Large Reynolds Numbers*, Doklady Akademii Nauk SSSR **30**, 299–303, in Russian.

[35] Kolmogorov, A. (1991), *The Local Structure of Turbulence in Incompressible Viscous Fluid for Very Large Reynolds Numbers*, Proceedings of the Royal Society of London. Series A: Mathematical and Physical Sciences **434**(1890), 9–13.

[36] Pope, S. (2000), *Turbulent Flows*, Cambridge University Press, ISBN 978-0-521-59886-6, doi:10.1017/CBO9780511840531.

[37] White, F.M. (2008), *Fluid Mechanics*, McGraw-Hill, 6th edn., ISBN 978-0-07-128645-9.

[38] Dandois, J., Garnier, E., Sagaut, P. (2007), *Numerical simulation of active separation control by a synthetic jet*, Journal of Fluid Mechanics **574**, 25–58, doi:10.1017/S0022112006003995.

[39] Hasan, M.A.Z. (1992), *The flow over a backward-facing step under controlled perturbation: laminar separation*, Journal of Fluid Mechanics **238**, 73–96, doi:10.1017/S0022112092001642.

[40] Murugappan, S., Mihaescu, M., Dimicco, R., Gutmark, E., Landmann, A., Treiber, D., Anderson, B. (2007), *Flow-field and Acoustic Interaction behind a Ramped Step*, in: *45th AIAA Aerospace Sciences Meetings and Exhibit, Reno, Nevada*, doi:10.2514/6.2007-1325, AIAA-2007-1325.

[41] Cherry, N.J., Hillier, R., Latour, M.E.M.P. (1984), *Unsteady measurements in a separated and reattaching flow*, Journal of Fluid Mechanics **144**, 13–46, doi:10.1017/S002211208400149X.

[42] Hudy, L.M., Naguib, A.M., Humphreys, W.M. (2003), *Wall-pressure-array measurements beneath a separating/reattaching flow region*, Physics of Fluids **15**(3), 706–717, doi:10.1063/1.1540633.

[43] OpenFOAM Foundation (2012), *OpenFOAM, The Open Source CFD Toolbox User Guide, version 2.1.1*.

[44] Weller, H.G., Tabor, G., Jasak, H., Fureby, C. (1998), *A tensorial approach to computational continuum mechanics using object-oriented techniques*, Computers in Physics **12**(6), 620–631, doi:10.1063/1.168744.

[45] Jasak, H. (1996), *Error analysis and estimation in the finite volume method with applications to fluid flows*, Ph.D. thesis, University of London, Imperial College.

[46] Marić, T., Höpken, J., Mooney, K. (2014), *The OpenFOAM Technology Primer*, sourceflux UG, ISBN 978-3-00-046757-8.

[47] Poinsot, T., Veynante, D. (2001), *Theoretical and Numerical Combustion*, R.T. Edwards, ISBN 1-930217-05-6.

[48] Fureby, C., Tabor, G. (1997), *Mathematical and Physical Constraints on Large-Eddy Simulations*, Theoretical and Computational Fluid Dynamics **9**(2), 85–102, doi:10.1007/s001620050034.

[49] Fureby, C. (1996), *On subgrid scale modeling in large eddy simulations of compressible fluid flow*, Physics of Fluids **8**(5), 1301–1311, doi:10.1063/1.868900.

[50] Fureby, C., Tabor, G., Weller, H.G., Gosman, A.D. (1997), *A comparative study of subgrid scale models in homogeneous isotropic turbulence*, Physics of Fluids **9**(5), 1416–1429, doi: 10.1063/1.869254.

[51] Yoshizawa, A. (1986), *Statistical theory for compressible turbulent shear flows, with the application to subgrid modeling*, Physics of Fluids **29**(7), 2152–2164, doi:10.1063/1. 865552.

[52] Ghosal, S., Lund, T.S., Moin, P., Akselvoll, K. (1995), *A dynamic localization model for large-eddy simulation of turbulent flows*, Journal of Fluid Mechanics **286**(3), 229–255, doi:10.1017/S0022112095000711.

[53] Smagorinsky, J. (1963), *General circulation experiments with the primitive equations: I. The basic experiment*, Monthly Weather Review **91**(3), 99–164, doi:10.1175/ 1520-0493(1963)091<0099:GCEWTP>2.3.CO;2.

[54] Piomelli, U., Balaras, E. (2002), *Wall-Layer Models for Large-Eddy Simulations*, Annual Review of Fluid Mechanics **34**(1), 349–374, doi:10.1146/annurev.fluid.34.082901. 144919.

[55] Cabot, W., Moin, P. (2000), *Approximate Wall Boundary Conditions in the Large-Eddy Simulation of High Reynolds Number Flow*, Flow, Turbulence and Combustion **63**(1-4), 269–291, doi:10.1023/A:1009958917113.

[56] Spalding, D. (1961), *A Single Formula for the "Law of the Wall"*, Journal of Applied Mechanics **28**(3), 455–458, doi:10.1115/1.3641728.

[57] de Villiers, E. (2006), *The Potential of Large Eddy Simulation for the Modeling of Wall Bounded Flows*, Ph.D. thesis, Imperial College of Science, Technology and Medicine, London.

[58] Spalart, P., Jou., W.H., Strelets, M., Allmaras, S. (1997), *Comments on the feasibility of LES for wings, and on a hybrid RANS/LES approach*, in: Liu, C., Liu, Z. (eds.), *Proceedings of the First AFOSR International Conference on DNS/LES*, 137–147, Greyden Press, Columbus.

[59] Spalart, P., Allmaras, S. (1992), *A one-equation turbulence model for aerodynamic flows*, in: *30th Aerospace Sciences Meeting and Exhibit, Reno, Nevada*, doi:10.2514/6.1992-439, AIAA-1992-439.

[60] Spalart, P., Deck, S., Shur, M., Squires, K., Strelets, M., Travin, A. (2006), *A New Version of Detached-eddy Simulation, Resistant to Ambiguous Grid Densities*, Theoretical and Computational Fluid Dynamics **20**(3), 181–195, doi:10.1007/s00162-006-0015-0.

[61] Spalart, P.R. (2009), *Detached-Eddy Simulation*, Annual Review of Fluid Mechanics **41**(1), 181–202, doi:10.1146/annurev.fluid.010908.165130.

[62] Jasak, H., Weller, H., Gosman, A. (1999), *High resolution NVD differencing scheme for arbitrarily unstructured meshes*, International Journal for Numerical Methods in Fluids **31**(2), 431–449, doi:10.1002/(SICI)1097-0363(19990930)31:2<431::AID-FLD884>3.0.CO;2-T.

[63] Issa, R. (1986), *Solution of the implicitly discretised fluid flow equations by operator-splitting*, Journal of Computational Physics **62**(1), 40–65, doi:10.1016/0021-9991(86)90099-9.

[64] Patankar, S., Spalding, D. (1972), *A calculation procedure for heat, mass and momentum transfer in three-dimensional parabolic flows*, International Journal of Heat and Mass Transfer **15**(10), 1787–1806, doi:10.1016/0017-9310(72)90054-3.

[65] Aider, J.L., Danet, A., Lesieur, M. (2007), *Large-eddy simulation applied to study the influence of upstream conditions on the time-dependant and averaged characteristics of a backward-facing step flow*, Journal of Turbulence **8**(N51), doi:10.1080/14685240701701000.

[66] Lund, T.S., Wu, X., Squires, K.D. (1998), *Generation of Turbulent Inflow Data for Spatially-Developing Boundary Layer Simulations*, Journal of Computational Physics **140**(2), 233–258, doi:10.1006/jcph.1998.5882.

[67] Lumley, J.L. (1967), *The structure of inhomogeneous turbulent flows*, in: Yaglom, A.M., Tatarsky, V.I. (eds.), *Atmospheric turbulence and radio wave propagation*, 166–178, Nauka, Moscow.

[68] Holmes, P., Lumley, J.L., Berkooz, G. (1996), *Turbulence, coherent structures, dynamical systems and symmetry*, Cambridge University Press, ISBN 978-0-521-55142-7.

[69] Duwig, C., Iudiciani, P. (2009), *Extended Proper Orthogonal Decomposition for Analysis of Unsteady Flames*, Flow, Turbulence and Combustion **84**(1), 25–47, doi:10.1007/s10494-009-9210-6.

[70] Iudiciani, P., Duwig, C., Hosseini, S., Szasz, R., Fuchs, L., Gutmark, E., Lantz, A., Collin, R., Aldén, M. (2010), *Proper Orthogonal Decomposition for Experimental Investigation of Swirling Flame Instabilities*, in: *48th AIAA Aerospace Sciences Meeting Including the New Horizons Forum and Aerospace Exposition*, doi:10.2514/6.2010-584, AIAA-2010-584.

[71] Arndt, R.E.A., Long, D.F., Glauser, M.N. (1997), *The proper orthogonal decomposition of pressure fluctuations surrounding a turbulent jet*, Journal of Fluid Mechanics **340**, 1–33, doi:10.1017/S0022112097005089.

[72] Picard, C., Delville, J. (2000), *Pressure velocity coupling in a subsonic round jet*, International Journal of Heat and Fluid Flow **21**(3), 359–364, doi:10.1016/S0142-727X(00)00021-7.

[73] Zhang, Y., Yim, S.C. (2015), *Proper Orthogonal Decomposition of Pressure Field in Sloshing Impact*, Journal of Engineering Mechanics **141**(9), doi:10.1061/(ASCE)EM.1943-7889. 0000924.

[74] Sirovich, L. (1987), *Turbulence and the dynamics of coherent structures. Part I: Coherent structures*, Quarterly of Applied Mathematics **45**(3), 561–571.

[75] Smith, T.R., Moehlis, J., Holmes, P. (2005), *Low-Dimensional Modelling of Turbulence Using the Proper Orthogonal Decomposition: A Tutorial*, Nonlinear Dynamics **41**(1), 275–307, doi:10.1007/s11071-005-2823-y.

[76] Timoshenko, S., Woinowsky-Krieger, S. (1959), *Theory of plates and shells*, McGraw-Hill, New York, 2nd edn., ISBN 0-07-064779-8.

[77] Pilkey, W. (1994), *Formulas for Stress, Strain, and Structural Matrices*, John Wiley & Sons, Inc., ISBN 0-471-52746-7.

[78] Austrell, P.E., Dahlblom, O., Lindemann, J., Olsson, A., Olsson, K.G., Persson, K., Petersson, H., Ristinmaa, M., Sandberg, G., Wernberg, P.A. (2004), *CALFEM — A Finite Element Toolbox version 3.4*, Studentlitteratur, ISBN 91-8855823-1.

[79] Dassault Systèmes (2013), *Abaqus theory manual*, version 6.13.

[80] Ottosen, N., Petersson, H. (1992), *Introduction to the Finite Element Method*, Prentice Hall International, ISBN 0-13-473877-2.

[81] Bathe, K.J. (2006), *Finite Element Procedures*, Klaus-Jürgen Bathe, Cambridge, MA, ISBN 978-0-9790049-0-2.

[82] Newmark, N.M. (1959), *A Method of Computation for Structural Dynamics*, Journal of the Engineering Mechanics Division **85**(3), 67–94.

[83] Chopra, A. (2007), *Dynamics of structures: Theory and applications to earthquake engineering*, Prentice Hall, Upper Saddle River, NJ, 3rd edn., ISBN 0-13-156174-X.

[84] Lindgren, G., Rootzén, H., Sandsten, M. (2013), *Stationary stochastic processes for scientists and engineers*, CRC Press, ISBN 978-1-4665-8618-5.

[85] Proakis, J.G., Manolakis, D.G. (2006), *Digital Signal Processing*, Prentice Hall, 4th edn., ISBN 0-13-187374-1.

[86] Welch, P.D. (1967), *The use of fast Fourier transform for the estimation of power spectra: A method based on time averaging over short, modified periodograms*, IEEE Transactions on Audio and Electroacoustics **AU-15**(2), 70–73, doi:10.1109/TAU.1967.1161901.

[87] Clough, R., Penzien, J. (2003), *Dynamics of structures*, McGraw-Hill, 3rd edn., ISBN 0-923907-50-5.

[88] Medici, D., Alfredsson, P.H. (2006), *Measurements on a wind turbine wake: 3D effects and bluff body vortex shedding*, Wind Energy **9**(3), 219–236, doi:10.1002/we.156.

Part II

Appended publications

Paper A
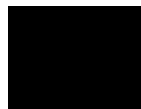
Load and response prediction using numerical methods in acoustic fatigue

Johan Nilsson,[*] Robert-Zoltán Szász,[†] Per-Erik Austrell[*] and Ephraim J. Gutmark[‡]

Abstract

A numerical procedure for load and response prediction in the context of acoustic fatigue is investigated on a model problem. Contrary to design guidelines, where the load need to be specified (e.g. based on experiments), the procedure used herein consists of simulating the load with computational fluid dynamics and then using the simulated load as a load input to a finite element simulation of the exposed structure. The model problem studied is a ramped backward-facing step with a thin aluminum panel fitted downstream of the step, parallel to the flow. The vortices generated in the wake of the step impose a time varying load on the aluminum panel. The numerical results on the load and response are compared to experimental results. The load is simulated with large-eddy simulations with a wall function. The mean reattachment length, load intensity and spectrum compares well with the measurements with the exception of a somewhat overpredicted cut-off frequency. The panel response prediction compares reasonably well with the measurements indicating that there is good potential for the proposed procedure to be used for load and response prediction in the context of acoustic fatigue analysis.

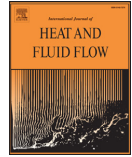[*]Division of Structural Mechanics, Lund University, PO Box 118, SE-221 00, Lund, Sweden.

[†]Division of Fluid Mechanics, Lund University, PO Box 118, SE-221 00, Lund, Sweden.

[‡]Department of Aerospace Engineering and Engineering Mechanics, University of Cincinnati, PO Box 210070, Cincinnati, OH 45221-0070, USA.

Paper B

Passive load control in backward-facing step flow by using chevrons

Johan Nilsson,[*] Robert-Zoltán Szász,[†] Per-Erik Austrell[*] and Ephraim J. Gutmark[‡]

Abstract

The ability of chevrons at the top edge of a backward-facing step to reduce downstream surface pressure fluctuations is investigated numerically. Three different chevron configurations are compared against a baseline case without chevrons. Low frequency reduction in the surface pressure fluctuations is observed for two of the configurations. The chevrons do not appear to have a significant effect on the flow as the mean reattachment length for all configurations is nearly constant and there is only a small increase in streamwise turbulence for one configuration with the other configurations unchanged.

---

[*]Division of Structural Mechanics, Lund University, PO Box 118, SE-221 00, Lund, Sweden.

[†]Division of Fluid Mechanics, Lund University, PO Box 118, SE-221 00, Lund, Sweden.

[‡]Department of Aerospace Engineering and Engineering Mechanics, University of Cincinnati, PO Box 210070, Cincinnati, OH 45221-0070, USA.

Paper C

Numerical simulation of surface pressure fluctuations in transonic fence-like flows with high Reynolds number

Johan Nilsson [a,*], Robert-Zoltán Szász [b], Per-Erik Austrell [a], Delphine Bard [c]

[a] Division of Structural Mechanics, Lund University, PO Box 118, Lund SE-221 00, Sweden
[b] Division of Fluid Mechanics, Lund University, PO Box 118, Lund SE-221 00, Sweden
[c] Division of Engineering Acoustics, Lund University, PO Box 118, Lund SE-221 00, Sweden

A R T I C L E   I N F O

A B S T R A C T

Surface pressure fluctuations downstream of an inclined fence are investigated with compressible, large-eddy simulations with wall-treatment. The simulations are performed at $\mathrm{Re}_h = 1.6 \cdot 10^6$ and transonic Mach numbers, which are realistic operating conditions in the aircraft industry. Simulation results are compared with existing measurements. Three different configurations are simulated to investigate the sensitivity to geometrical effects. Simulated cross-correlation spectra agreement with measurements appears to be on the level required for a good response prediction of an aircraft skin surface panel placed downstream of the fence. Root-mean-square pressure fluctuation levels are found to be closer to backward-facing step flow than standard fence flow. The effect of a leading edge upstream of the fence is shown to influence the spectral characteristics of the pressure load downstream of the fence. Correlation lengths and the propagation of pressure disturbances are investigated with auto and cross-correlation maps, phase angle analysis of the cross spectrum and frequency–wave-number spectra.

© 2016 Elsevier Inc. All rights reserved.

1. Introduction

Separating/reattaching flows are common in many technical applications. In the reattachment region such flows produce large pressure fluctuations on the underlying surface. These pressure fluctuations can, in addition to noise, cause significant vibrations which could ultimately lead to fatigue and failure. This is an issue for example for the aircraft and aerospace industry.

There are many studies on separated flows in the literature and it is common to study simple geometries where the separation point is fixed. One example of such a geometry is the backward-facing step, for which there are both experimental (see for example Camussi et al., 2006; Efimtsov et al., 2000; Farabee and Casarella, 1984; Heenan and Morrison, 1998), and numerical (see for example Aider et al., 2007; Dandois et al., 2007; Ji and Wang, 2012; Nilsson et al., 2015) studies, just to mention a few. Another example of a simple geometry with separated flow is where a fence is mounted perpendicular to the downstream surface. Experimental studies on fence flow include Hudy et al. (2003), Castro and Haque (1987) and Ruderich and Fernholz (1986), as well as Cherry et al. (1984) with the difference that their study uses a blunt-face splitter plate instead. To our knowledge, there are not so many

numerical studies on fence flow, but there is that of Orellano and Wengle (2001), di Mare and Jones (2003) and Pascarelli et al. (2001). Orellano and Wengle (2001) studied the flow past a fence without a solid upper boundary with a Reynolds number based on fence height h at $\mathrm{Re}_h = 3000$. They found that applying periodic blowing/suction upstream of the fence at a frequency near the 'shedding frequency' discussed below, would reduce the mean reattachment length. The study by di Mare and Jones (2003) uses a swept fence (i.e. the fence is not orthogonal to the freestream velocity, but orthogonal to the bottom wall) at $\mathrm{Re}_h = 3900$. Finally, the study by Pascarelli et al. (2001) is a fence-channel flow study at $\mathrm{Re}_h = 5600$. The blockage effect is significant in their study as the fence blocks half the channel height. Neither of the computational studies investigated surface pressure fluctuations.

Both the backward-facing step and the fence flow share several common characteristics. For both types of flow, the intensity of the pressure fluctuations on the downstream wall has a maximum near, or just upstream, of the mean reattachment point x_r (for the backward-facing step flow, see Camussi et al., 2006; Farabee and Casarella, 1984; Ji and Wang, 2012, for fence flows see Cherry et al., 1984; Hudy et al., 2003). However, the maximum level of the pressure fluctuations $C_{p'} = p'_{\mathrm{rms}}/0.5\rho U_\infty^2$ are different. The typical value found in studies on the backward-facing step is around $C_{p'} = 0.035$ (Camussi et al., 2006; Farabee and Casarella, 1984; Ji and Wang, 2012), while for fence flows

* Corresponding author. Tel.: +46 462227404.
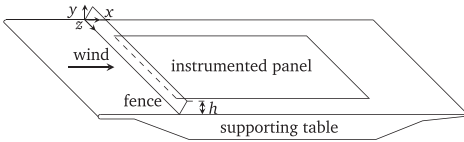*E-mail address:* Johan.Nilsson@construction.lth.se (J. Nilsson).

Fig. 1. Test setup used in the ACOUFAT project (Tougard, 1995).

Cherry et al. (1984) finds about $C_{p'} = 0.16$ and Hudy et al. (2003) finds about $C_{p'} = 0.125$.

There are two instabilities commonly observed in separated flows which can be seen in the pressure spectrum on the surface downstream of the flow separating feature. The first instability is the Kelvin–Helmholtz (K–H) instability which generates long spanwise structures. These structures reduce to the shedding mode via one or more vortex merging processes as described by Hasan (1992). The shedding frequency is typically found to be in the range of $0.6 < \mathrm{St}_{x_r} < 0.8$, where $\mathrm{St}_{x_r} = fx_r/U_\infty$, f is the frequency, x_r is the mean reattachment length and U_∞ is the freestream velocity. Dandois et al. (2007) provide a good compilation of the shedding frequency for many studies on the backward-facing step and fence flow (see Table 1 in their work). The second instability is the absolute instability of the recirculation bubble. The instability is associated with the flapping motion of the shear layer. The flapping frequency is typically found in the range of $0.12 < \mathrm{St}_{x_r} < 0.18$, once again see Table 1 in Dandois et al. (2007) for a large number of examples.

The present study is a numerical study on fence flow with the fence mounted at 60° incidence. The flow geometry is illustrated in Fig. 1 and is chosen to match that of a wind-tunnel experiment performed in the BRITE-EURAM programme 'Acoustic fatigue and related damage tolerance of advanced composite and metallic structures' (ACOUFAT) (Tougard, 1995). Those measurements are used as comparison for the numerical results. This particular experiment was also studied by Campos et al. (1999). In their work, they studied the importance of the cross-correlation spectra between two spatial points of the pressure load for the response prediction of a flexible panel structure mounted on the surface downstream of the fence. They used a frequency domain finite element formulation that used the power spectral densities and cross-spectral densities as input. They found that the response prediction was sensitive to the cross-correlation spectra. Different modes were excited depending on whether the cross-correlation was high or low. Campos et al. (1999) also developed a 'semi-empirical' model for the cross-correlation spectra. The simulated response produced when using Campos' model for the cross-correlation spectra is remarkably close to the measured response, even though the cross-correlation spectra themselves did not match the measurements to the same extent. They suggested that the local discrepancies in their model may be outweighed by an adequate global match. There were also comparisons between the response of the same panel structure exposed to the loads from the wind-tunnel experiment and when exposed to the load from a Progressive Wave Tube (PWT). Once again, different modes were excited and it was attributed to the different cross-correlation spectra, of the load (Campos et al., 1999; Tougard, 1995). The 'semi-empirical' model developed by Campos et al. (1999) required no less than eight parameters that were taken from the wind-tunnel measurements. Here, we evaluate a much more generic numerical method for the study of the load on the downstream panel surface. Although computationally more demanding, it has the advantage of offering more details and avoids the need for obtaining semi-empirical model constants from expensive experiments.

Cunningham et al. (2003) studied the response of doubly curved composite panels in a PWT numerically and experimentally.

When modelling the PWT loading numerically they, like Campos et al. (1999), used a frequency domain FE formulation and applied the spectra measured in the PWT. They tested the conventional methods of assuming that the load is in phase over the entire panel surface against modelling the load as waves traveling over the exposed panel. The latter was accomplished by setting the phase of the complex valued load by using analytical expressions. They concluded that taking this phase information into account significantly improved the response prediction. In comparison to the study by Campos et al. (1999), they more or less reached the same conclusion. The difference is that Cunningham et al. (2003) had a less complicated load and could use simple analytical expressions to set the phase relations, while Campos et al. (1999) had a more complicated phase load and used the full cross-correlation spectra instead.

The present simulations are performed on three different geometrical configurations in order to study the sensitivity of different boundary conditions (BCs). They have varying level of complexity with additional geometrical features being added for each successive configuration. Details of the configurations are found in Section 3.2. In addition to the reference experiments in the ACOUFAT programme (Tougard, 1995), the simulation results are also compared to other sources in the literature on fence flow and occasionally also to studies on backward-facing step flow. This study is performed at a Reynolds number of $\mathrm{Re}_h = 1.6 \cdot 10^6$, which is three orders of magnitude larger than the previous numerical studies on fence flow. Also, the present simulations are compressible as they take place at transonic Mach number, $\mathrm{Ma}_\infty = 0.7$. All previous numerical studies on fence flow have been incompressible (di Mare and Jones, 2003; Orellano and Wengle, 2001; Pascarelli et al., 2001). The present conditions are much more realistic for the aircraft and aerospace industry and it is important to have numerical methods applied to realistic conditions as well. To assess the quality of the results, various statistics of the surface pressure are computed and compared to data from the literature. Besides average and r.m.s. pressure, spectral densities and auto-correlations are discussed. Relations between frequency and convection of the pressure disturbances are investigated by two point statistics such as cross-correlations, cross-spectral analysis and two dimensional frequency–wave-number spectra. To obtain a better insight in the flow dynamics, the average velocity field and the turbulence intensities are discussed as well. Large-scale structures are visualised using the Q-criterion.

2. Model problem

In this work a model problem that was originally studied in the BRITE-EURAM program 'Acoustic fatigue and related damage tolerance of advanced composite and metallic structures' (ACOUFAT) (Tougard, 1995) is revisited. Among the numerous tests and measurements performed in the program, the wind tunnel experiment of a simple fence (called flap in the original report) located upstream of a panel structure, is used as comparison for this work. The geometry is illustrated by Fig. 1. The flow was transonic with a Reynolds number based on fence height h of $\mathrm{Re}_h = 1.6 \cdot 10^6$ and a freestream Mach number of $\mathrm{Ma}_\infty = 0.7$. The fence height is defined in Fig. 1. Both the fence and the measurement plate were mounted on a table that was dynamically decoupled from the wind tunnel. The wind tunnel used was the Onera Modane S1 tunnel, which has a circular cross-section with a diameter of 8 m (92h) and a stagnation pressure of 0.9 bar. The size of the wind tunnel relative the fence and the table make the blockage effects small. The table was also raised away from the wind tunnel floor to avoid the wind tunnel boundary layer. The fence, which covered the whole width of the table, measured 15.0h in the spanwise direction and was mounted at 60° incidence. The measurement

panel downstream of the fence measured 14.5h in the streamwise direction and 9.9h in the spanwise direction. Also, the distance between the fence mounting on the table and the measurement panel was h. The panel was instrumented with microphones acting as pressure transducers and static pressure sensors. The microphones (1/8 in Brüel & Kjær) were placed in cylindrical holes of the thick plate with the membrane just below the surface of plate. Flush mounted above the microphones, there was a thin grid to protect the membrane and to avoid any surface discontinuity. The distance between the membrane and the grid was small enough to prevent any Helmholtz resonator effects.

3. Numerical method

3.1. Solver and discretisation

To perform the CFD simulations, the finite-volume based open source software library OpenFOAM is used (OpenFOAM Foundation, 2012). The chosen solver is sonicFoam which uses the PISO algorithm to solve the compressible Navier–Stokes equations. For turbulence modelling, Large Eddy Simulation (LES) is used with the compressible Smagorinsky model. In OpenFOAM the compressible Smagorinsky model is implemented following Fureby (1996): assume that the subgrid stress tensor **B** is

$$\mathbf{B} = \frac{2}{3}k_{sgs}\mathbf{I} - 2\frac{\mu_{sgs}}{\rho}\mathrm{dev}(\mathbf{D}),$$

where $\mathrm{dev}(\mathbf{D})$ is the deviatoric part of the rate of strain tensor **D**, **I** is the identity tensor, k_{sgs} is the subgrid kinetic energy, μ_{sgs} is the subgrid viscosity and ρ is the fluid density. Then local equilibrium is assumed, i.e. the production of k_{sgs} equals the dissipation of k_{sgs}. This gives the following expression that is used to compute k_{sgs}:

$$\rho\mathbf{D}:\mathbf{B} + \frac{C_e\rho k_{sgs}^{3/2}}{\Delta} = 0,$$

together with

$$\mu_{sgs} = C_k\rho\Delta\sqrt{k_{sgs}}.$$

The default values in OpenFOAM of the two constants $C_k = 0.02$ and $C_e = 1.048$ are used.

As the computational cost to directly treat the boundary layer near solid walls with LES would become prohibitively expensive, some kind of wall treatment is necessary. A wall-function is used to determine the subgrid viscosity μ_{sgs} at the wall together with a no-slip BC. The wall-function is an equilibrium stress model, based on Spalding's law of the wall (Spalding, 1961)

$$y^+ = u^+ + \frac{1}{E}\left(e^{\kappa u^+} - 1 - \frac{\kappa u^+}{1!} - \frac{(\kappa u^+)^2}{2!} - \frac{(\kappa u^+)^3}{3!}\right), \tag{1}$$

where κ and E are constants with the values of $\kappa = 0.41$ and $E = 9.8$ and y^+ and u^+ are the distance to the wall and the velocity next to the wall in wall units, respectively. They are given by $y^+ = (yu_\tau\rho)/\mu$ and $u^+ = u/u_\tau$. Eq. (1) is iterated using the Newton–Raphson method to determine the value of u_τ. Then the following relation for the wall shear stress τ_w is used to determine μ_{sgs}

$$\tau_w = (\mu + \mu_{sgs})\left(\frac{\partial u}{\partial y}\right)_{y=0} = u_\tau^2\rho.$$

Since Spalding's law of the wall provides a good approximation in of the boundary layer in the viscous, buffer and log-law layers of the boundary layer, there is no requirement that $y^+ > 30$ holds for the first of-the-wall grid point which is the case for equilibrium stress models that are based on the log-law.

For the convective term in the momentum equations, the Linear-Upwind Stabilised Transport (LUST) scheme is used. It is a

second order discretisation scheme with upwind blending for stability, while still maintaining second order behaviour (OpenFOAM Foundation, 2012). For the other convection terms the Gamma scheme (Jasak et al., 1999) is used with the user specified coefficient in the scheme set to maximum stability. For all other terms, the spatial discretisation schemes are second order central differencing. The time discretisation scheme is Crank-Nicolson. In order to suppress spurious oscillations the Crank–Nicolson scheme is blended with a first order scheme together with a short time step, $\Delta t = 1 \cdot 10^{-6}$. The velocity is specified at the inlet without any perturbations ($U_\infty = 240$ m/s, Ma = 0.7). The simulations ran for many time steps until statistical quantities such as mean and r.m.s. values no longer appear to change. Then, each simulation ran for 10^6 number of iterations where the presented data was sampled, i.e. the simulated time was one second.

To reduce the size and complexity of the CFD model, a quasi 3D model is used with cyclic boundary conditions (BCs) on the sides and only modelling a section of the fence and the plate. This means that the model can be considered to consist of an infinitely wide table and fence. The simulated model is 4.6h wide, and the total streamwise length of the table is 27.7h long. In the ACOUFAT measurements (Tougard, 1995) it was indicated that the 3D effects of the flow coming in from the sides of the table and the vortices from the fence corners were not significant when studying measurements from microphones that are far away from the side edges of the table. Therefore it is believed that comparisons between the ACOUFAT measurements (Tougard, 1995) near the centre line of the table and an infinitely wide model should still be useful.

3.2. Simulation configurations

Three different configurations using different BCs are tested. They will be referred to as cases A, B and C as illustrated in Fig. 2. Case A is the simplest of the configurations. It uses slip BC upstream of the plate and no-slip downstream of the leading edge of the table. The table does not end, instead the no-slip BC is used throughout the remainder of the domain. Case B tries to capture the effect of the leading edge more accurately. The actual thickness of the leading edge and the rounded geometry are present. Also the flow can pass underneath the table. The distance from the table underside to the wind tunnel floor is the same as from the leading edge underside to the wind tunnel floor in the measurements that are used for comparison (Tougard, 1995). However, the BC underneath the table is simple slip BC and the geometry and mesh detail is low in this region. The motivation for this is that the flow underneath the table itself is of minor importance in this study as long as the flow can pass. Finally, case C tries to capture more of the experimental geometry used for comparison than the other two cases. In addition to the leading edge present in case B, the whole table is present. All sides of the table use noslip BC while the wind tunnel floor still uses slip BC. The table geometry matches the one used in the experiment, with one difference: The supporting pillar has been removed. The fact that the floor underside causes a contraction against the wind tunnel floor should cause a larger portion of the flow to be pushed to the top side of the table than in configuration B. This is captured by having the actual table geometry. In the experiment, the flow has to go around the supporting pillar as well. Due to the use of cyclic BC an equivalent geometry cannot be employed without modelling the entire structure in the spanwise direction as well a large part of the wind tunnel width. This has not been done due to the computational costs involved. This means that the pressure build-up underneath the table would likely be larger if the same flat wind tunnel floor would be used together with the cyclic spanwise BC. The
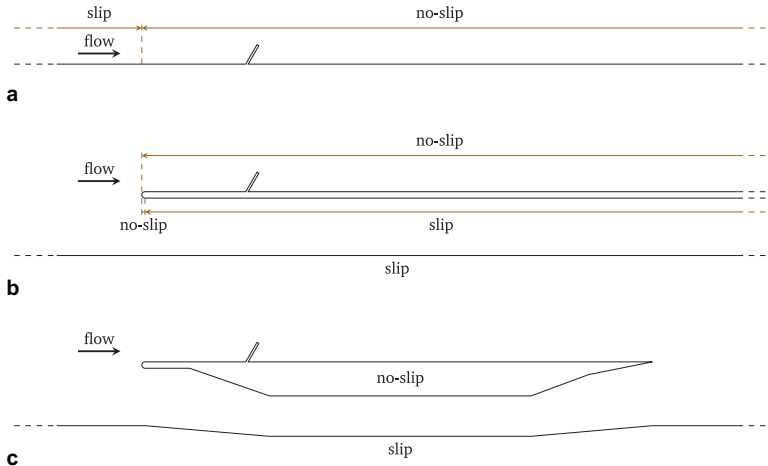
Fig. 2. The different boundary conditions tested. (a), (b) and (c) correspond to cases A, B and C, respectively.
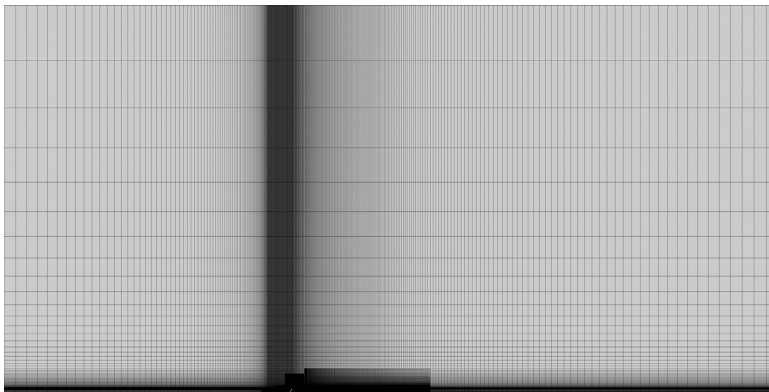

Fig. 3. Computational mesh.

reason for this being that the flow cannot flow around the obstacle in the spanwise direction. In an attempt to balance this effect, the wind tunnel floor was lowered underneath the table, as illustrated in Fig. 2. Thus, the distance between the table and the wind tunnel floor at its narrowest section is increased by 36%. However, there is still a pressure build-up underneath the table in the simulations.

3.3. Computational mesh

To ensure that the proximity to the domain boundaries does not have any significant undesired effects, the inlet was placed 69h upstream of the fence, the outlet 115h downstream of the fence and the ceiling 92h above the plate. The computational mesh is, to the extent possible, identical in all configurations. Obviously, the different configurations have different geometry which gives different computational domains, but in the regions where the geometry is the same, the mesh is also the same. In particular, the mesh around and downstream of the fence is identical in all configurations. Cells are clustered near walls and on the upper side of the table. The number of cells are 8.6, 9.0 and 13.4 million cells for

cases A, B and C, respectively. Fig. 3 illustrates the computational mesh for case A.

A mesh independence study was performed on case A. Three different meshes were tested with each successive mesh being refined equally in all directions. The coarse, medium and fine mesh had 2.6, 8.6 and 29.0 million cells, respectively. It was not possible to achieve mesh independent results in all aspects. The mean reattachment length x_r varied with the mesh density. The values for x_r are 16h, 19h and 22h for the coarse, medium and fine meshes, respectively. However, the results become essentially mesh independent if x_r is used for normalisation. In Fig. 4, the mean pressure $\bar{p}$ and the $C_{p'} = p'_{\text{rms}}/0.5\rho U_\infty^2$ value for the three meshes are plotted with the streamwise coordinate x normalised by x_r. While the convergence is not complete, it was deemed to be sufficient with the medium mesh as the fine mesh would have been too computationally demanding in relation to its benefit. All other results presented in this work use the medium mesh. However, there was only a small difference between the coarse mesh and the medium mesh in all of the presented results due to the normalisation with x_r (with the exception of x_r itself). The results on $C_{p'}$ are discussed in Section 4.4.
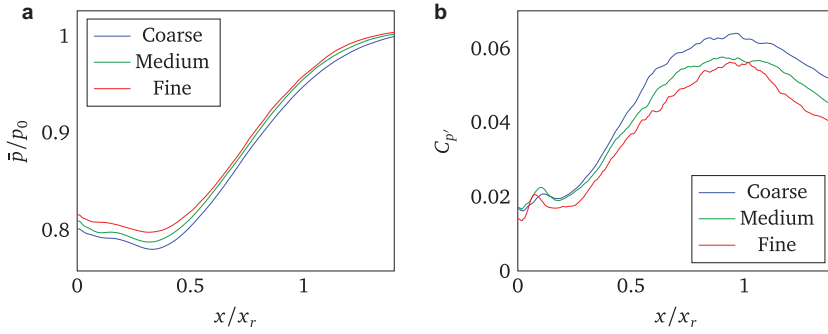
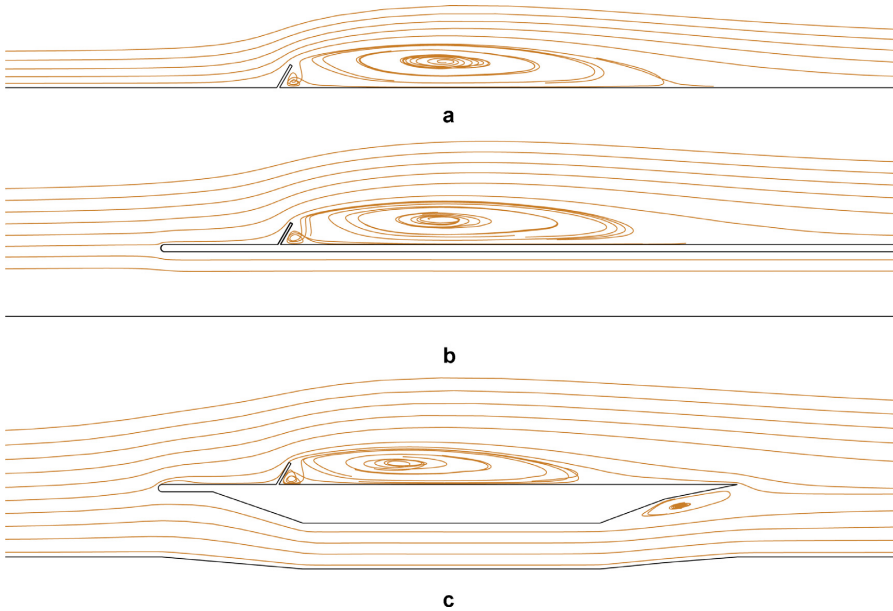**Fig. 4.** Mesh independence study. p_0 is the pressure set at the outlet.

Fig. 5. Mean streamlines. Cases A, B and C correspond to (a), (b) and (c), respectively.

The following values of y^+ are for the medium mesh. In the recirculation bubble, the largest near wall velocities are in the middle with maximum mean y^+ values at $y^+ \approx 100$ for all configurations. From the middle of the recirculation bubble the y^+ values decrease in both the upstream and downstream directions as the near wall velocity decreases. When the sign of the velocity changes near the fence and reattachment, the y^+ values are low. Downstream of the reattachment point, the y^+ values once again increase and exceed $y^+ \approx 100$ at $x \approx 1.35x_r$. The only presented results in this work beyond $x = 1.4x_r$ concerns case C where the flow has passed the downstream edge of the structure at $x = 1.4x_r$.

4. Results

4.1. Mean streamlines and velocities

Fig. 5 shows the mean streamlines for all three cases in the present simulations. The main feature is the recirculation bubble

downstream of the fence. Also, just next to the fence corner is a small secondary recirculation bubble rotating in the opposite direction of the main recirculation bubble. The only noticeable difference in the mean streamlines between cases A and B, apart from the obvious fact that the streamlines can go below the table in case B, is that the incoming streamlines appears to turn upwards a bit earlier in case B than in case A. It appears that the presence of the leading edge pushes the flow higher. Case C, similarly to case B, also permits the flow to go underneath the table, but the chosen geometrical configuration turns the table structure and the contraction underneath to a much larger extent into an obstacle than in case B. This causes more of the flow to be diverted to the upper side of the table. Hence, the streamlines going above the table have a steeper slope compared to case B. This effectively increases the angle of attack of the table leading edge, even causing a small zone of separation just downstream of the table leading edge. Near the downstream edge of the table in case C there is also a recirculation bubble on the underside of the table.
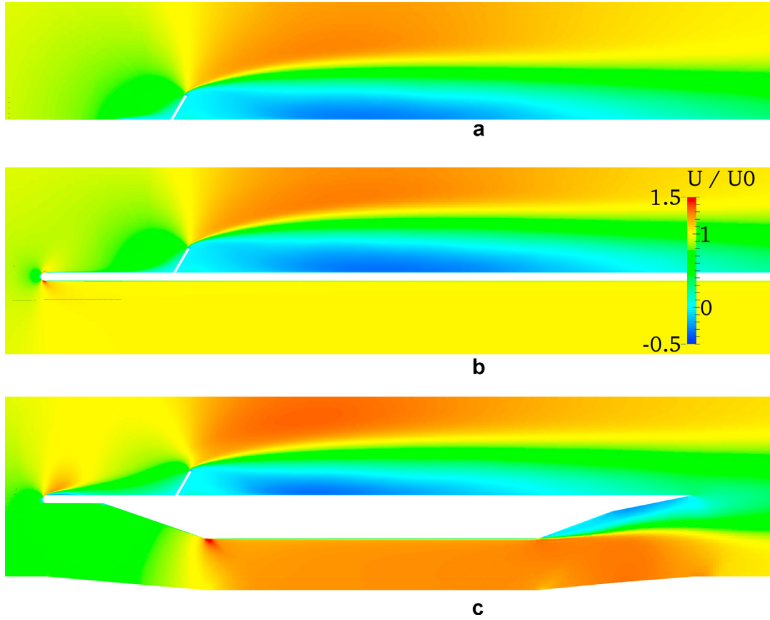
Fig. 6. Mean streamwise velocity normalised by the freestream velocity. Cases A, B and C correspond to (a), (b) and (c), respectively.
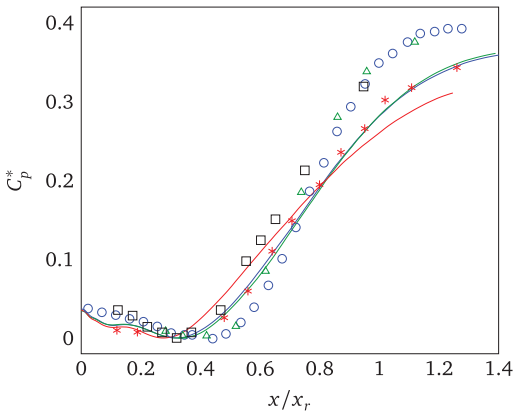

Fig. 7. Streamwise C_p^* distribution. Curves: ——, case A; ——, case B; ——, case C. Symbols: (□), ACOUFAT (Tougard, 1995); (○), Hudy et al. (2003); (△), Castro and Haque (1987); (∗), Roshko and Lau (1965). See Fig. 12 for the different geometries used in other studies than the present work.

As a complement to the mean streamlines in Fig. 5, Fig. 6 shows the mean velocities in the streamwise direction. In the bottom of Fig. 6c, the increased velocity due to the contraction under the table is clearly seen. In contrast, in Fig. 6b, the velocity is nearly unchanged from the incoming freestream velocity.

4.2. Mean pressure and mean reattachment length

The streamwise distribution, normalised by the mean reattachment length x_r, of the mean pressure coefficient C_p^* on the surface downstream of the fence is shown in Fig. 7, together with some

Table 1
Mean reattachment length x_r.

	Re_h	x_r	Num./Exp.
Case A	$1.6 \cdot 10^6$	$19h$	Num.
Case B	$1.6 \cdot 10^6$	$21h$	Num.
Case C	$1.6 \cdot 10^6$	$17h$	Num.
ACOUFAT (Tougard, 1995)	$1.6 \cdot 10^6$	$15h$	Exp.
Hudy et al. (2003)	$7.9 \cdot 10^3$	$26h$	Exp.
Castro and Haque (1987)	$2.2 \cdot 10^4$	$19h$	Exp.
Roshko and Lau (1965)	$1.4 \cdot 10^4$	$34h$	Exp.
Orellano and Wengle (2001)	$3.0 \cdot 10^3$	$13h$	Num.
Pascarelli et al. (2001)	$5.6 \cdot 10^3$	$10h$	Num.

earlier investigations on fence flow. The pressure coefficient is defined as

$$C_p^* = \frac{C_p - C_{p,\min}}{1 - C_{p,\min}}, \quad C_p = \frac{p_s - p_r}{\frac{1}{2}\rho U_\infty^2}$$

where p_s is the mean surface pressure, p_r is a reference pressure, ρ is the fluid density and $C_{p,\min}$ is the minimum C_p. This pressure coefficient was first proposed by Roshko and Lau (1965). The simulations of case A and case B are nearly indistinguishable and also follow the study by Roshko and Lau (1965) closely. However, case C is slightly different from cases A and B. In addition to some sensitivity to the mesh resolution, the x_r value is also sensitive to the geometrical difference of the simulated cases. However, note that the curves for cases A and B in Fig. 7, which are nearly indistinguishable, are scaled with x_r. This illustrates the usefulness of x_r as scaling parameter. The x_r value for the ACOUFAT (Tougard, 1995) study was never measured. Instead, it was estimated using the same method as the one used by Hudy et al. (2003). They determined that the value of C_p^* is approximately $C_p^* = 0.35$ at mean reattachment. The measured C_p^* curve was then extrapolated to find the streamwise coordinate that would intersect with the value $C_p^* = 0.35$. Table 1 gives the mean reattachment lengths
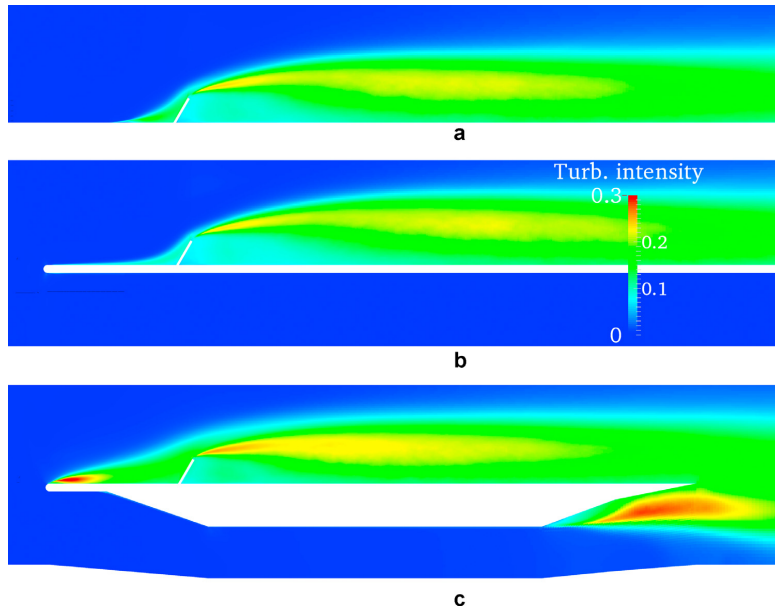
Fig. 8. Turbulence intensity defined as $I = \sqrt{(1/3)(u_x'^2 + u_y'^2 + u_z'^2)}/U_\infty$, where u_i' is the i-component of the velocity fluctuations. Cases A, B and C correspond to (a), (b) and (c), respectively.

x_r for the same studies shown in Fig. 7 as well as the study by Orellano and Wengle (2001) and Pascarelli et al. (2001). Finally, it should be noted that there is a large spread between the different studies, and that the present numerical results fits inside the range from earlier studies regardless of the mesh density tested in the mesh independence study.

4.3. Turbulence intensity

The turbulence intensity is shown in Fig. 8. For all three cases there is a zone of high intensity turbulence originating from the tip of the fence. The zone starts as a thin layer that widens further downstream. This zone is the location of the highest intensities for cases A and B, with the magnitude of the fluctuations being similar for cases A and B. Case C, however, has two more zones of high turbulence as well as a higher intensity near the fence tip. The first additional zone is located right behind the leading edge of the table. The intensity of this zone reduces quicker than the zone from the fence tip, but produces a larger turbulent boundary layer at the fence than is the case for cases A and B. The second additional high intensity zone is located under the downstream edge of the table.

In order to visualise the turbulent structures, isosurfaces of the Q-criterion are shown in Fig. 9. In all three cases, there are long streamwise Kelvin–Helmholtz vortices formed at the fence tip. However, they quickly start to break down as they convect downstream. While all three cases have similar structures downstream of the fence, there are differences upstream of the fence. Case A has nearly no structures visible in the Q-criterion until about one fence height upstream of the fence where there is some separation. Case B has a fairly uniform distribution of small vortices upstream of the fence. There is a slight increase in size just near the fence, but still much less and smaller in size than case A. Finally, case C has a lot of turbulent structures downstream the leading edge. However, the intensity decreases rapidly in the region

closest to the fence. Within one fence height upstream of the fence, case A has arguably higher intensity of turbulent structures visible through the Q-criterion than case C, despite the massive difference just upstream of this region. Fig. 10 shows the turbulence profiles near the fence. As expected from the larger amount of coherent structures found for cases A and C compared to case B in Fig. 9, case B has lower levels of turbulence in Fig. 10. These observations suggest that vortices generated upstream in cases B and C suppress the formation of large-scale vortices in the immediate vicinity of the fence, where the streamlines are deflected. This means that in similar flow situations it is crucial to account for any geometrical details which might influence the turbulent flowfield. Furthermore, details about upstream velocity profiles and turbulent stresses are equally important for an accurate prediction of the flowfield.

4.4. Root-mean-square pressure

Fig. 11 shows the streamwise distribution of the r.m.s. surface pressure. Also included in Fig. 11 are the experimental studies by ACOUFAT (Tougard, 1995), Hudy et al. (2003) and Cherry et al. (1984) as well as the numerical study on backward-facing step flow by Ji and Wang (2012). From the study by Ji and Wang (2012), the configuration with the smallest boundary layer thickness is used. In all cases shown in Fig. 11, except for the ACOUFAT study, the maximum $C_{p'}$ ($C_{p'} = p_{rms}'/0.5\rho U_\infty^2$) value is found near, or just upstream of, the mean reattachment point x_r. The present simulations have a peak value of $C_{p'} = 0.058$ which can be compared to the $C_{p'} = 0.047$ for the only measurement point near reattachment for the ACOUFAT study. The studies by Hudy et al. (2003) and Cherry et al. (1984) indicate peak values of about $C_{p'} = 0.16$ and $C_{p'} = 0.125$ respectively, which is much higher than the results from the present study. Since our simulations agree reasonably well with the experiments performed in the ACOUFAT study
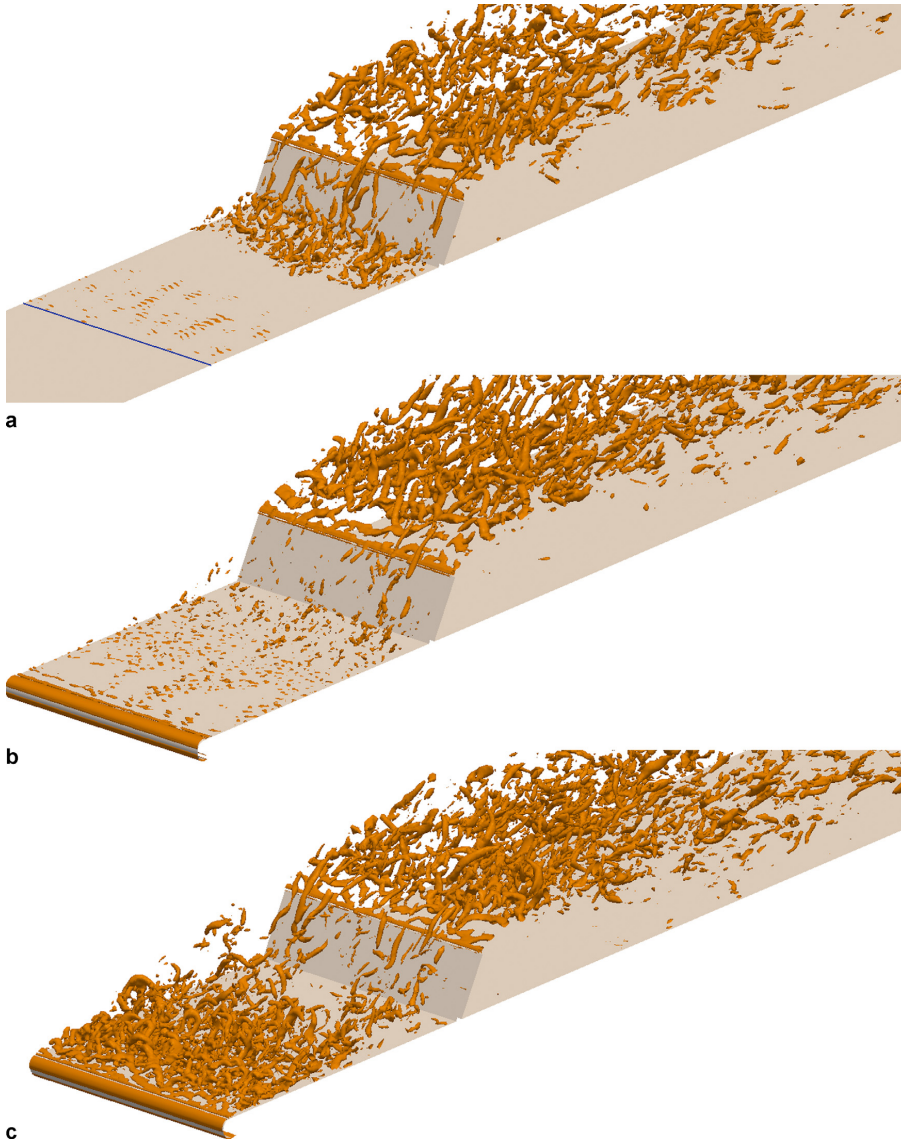
Fig. 9. Visualisation of the vortices through isosurfaces of the Q-criterion ($Q = 3000U_\infty^2/x_t^2$). Cases A, B and C correspond to (a), (b) and (c), respectively. The upstream line in (a) marks the change from slip to no-slip BC.

(Tougard, 1995), it is assumed that the lower r.m.s. values are due to the geometry. As can be seen in Fig. 11, the level of pressure fluctuations in the present configuration is closer to the backward-facing step than the other reported studies on fence flow. An explanation to this could be found in the upstream conditions of the fence. In the studies by Hudy et al. (2003) and Cherry et al. (1984), there is no solid surface upstream of the fence at all. The different configurations are illustrated in Fig. 12. While the fence deflects the flow, there is no structure there to trigger transition to turbulent flow upstream of the fence as in the present simulations where the leading edge of the table is the first solid

surface the flow encounters (see Section 4.3). In contrast, the studies on backward-facing step flow typically have a thick and well developed turbulent boundary layer on the surface upstream of the step. Aider et al. (2007) studied the effect of different inlet BC for the backward-facing step flow. They demonstrated that the turbulence in the boundary layer increased the break-up rate of the K–H vortices that are shed from the step. They found that this would then reduce the velocity fluctuations near mean reattachment when a BC that produced realistic turbulence was used, compared to a BC which did not produce any significant turbulence at the inlet. While the study by Aider et al. (2007)
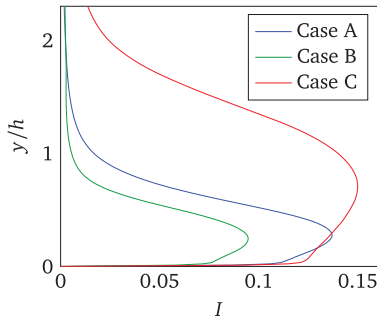
Fig. 10. Turbulence intensity I along a wall-normal line at $x = -0.5h$ ($I = \sqrt{(1/3)(u_x'^2 + u_y'^2 + u_z'^2)}/U_\infty$, where u_i' is the i-component of the velocity fluctuations).
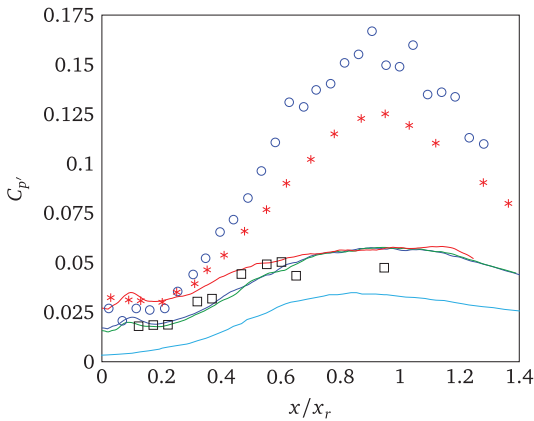

Fig. 11. Streamwise distribution of $C_{p'}$. Curves:——, case A; ——, case B; ——, case C; ——, Ji and Wang (2012). Symbols: (□), ACOUFAT (Tougard, 1995); (○), Hudy et al. (2003); (∗), Cherry et al. (1984). See Fig. 12 for the different geometries used in other studies than the present work.

does not look at the pressure fluctuations directly, a recent study by Nilsson et al. (2015) confirmed that the effect of having no turbulence in the incoming boundary layer would indeed give higher $C_{p'}$ levels in comparison to having real turbulence in the incoming boundary layer for backward-facing step flow. In summary, the lower $C_{p'}$ values for the present simulations compared to the studies by Hudy et al. (2003) and Cherry et al. (1984), may be caused by the turbulence generated by the table structure that is upstream of the fence. However, the boundary layer is still thin compared to the backward-facing step study by Ji and Wang (2012) (and most backward-facing step flow studies in general) plotted in Fig. 11, which could explain why the $C_{p'}$ levels are still significantly higher than the $C_{p'}$ values found by Ji and Wang (2012).

For the ACOUFAT study the maximum measured value occurs in a hump at around $x = 0.6x_r$. This hump does not appear on any of the other curves in Fig. 11. The hump is caused by tonal components that are discussed in Section 4.5. The cases A and B curve is once again nearly indistinguishable, but the case C curve is higher in the region $x \le 0.6x_r$.

In the region immediately downstream of the fence and about $x = 0.2x_r$ all curves, except for the backward-facing step study by Ji and Wang (2012), have a plateau. This plateau coincides approximately with the region underneath the secondary recirculation bubble. All configurations of the present simulations have a small hump in the upstream plateau. This hump does not appear in any of the experimental studies plotted in Fig. 11. However, it is present in most other flow configurations studied in the ACOUFAT measurements (Tougard, 1995). These configurations are not plotted in Fig. 11 for brevity. In particular, this hump appears in the configurations with a higher Mach number.

4.5. Power spectra

The power spectrum of the surface pressure is computed in the form of Power Spectral Densities (PSD) using Welch's method. Figs. 13–15 show the PSDs from equally spaced microphones in cases A, B and C, respectively. Each spectrum, except for the most upstream spectrum, is shifted along the ordinate by an integer times 10^4 in order to avoid clutter. The spectra are plotted with the most upstream spectrum at the bottom and the most downstream spectrum at the top. For case A (Fig. 13), all spectra except for the two most downstream ones have a strong low frequency amplitude in the region $St_{x_r} < 0.2$. Indeed, the three most upstream spectra are nearly flat in the region $St_{x_r} > 0.2$. In the literature, the flapping frequency is typically found to be in the range of $0.12 < St_{x_r} < 0.18$, which corresponds well with the low frequency peak observed in Fig. 13. See for example the fence flow study by Hudy et al. (2003) and the compilation in Table 1 of Dandois et al. (2007). However, the poor spectral resolution in the low frequencies only permits the conclusion that there is
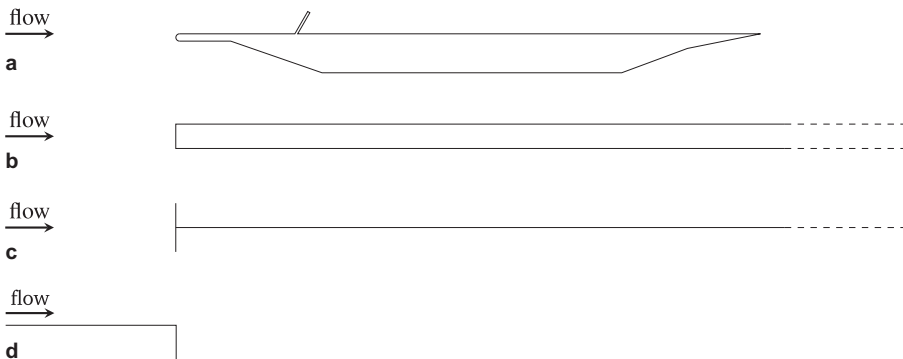

Fig. 12. The geometry of different related studies. (a) ACOUFAT (Tougard, 1995), (b) Cherry et al. (1984), (c) Hudy et al. (2003), Castro and Haque (1987) and Roshko and Lau (1965) and (d) Ji and Wang (2012).
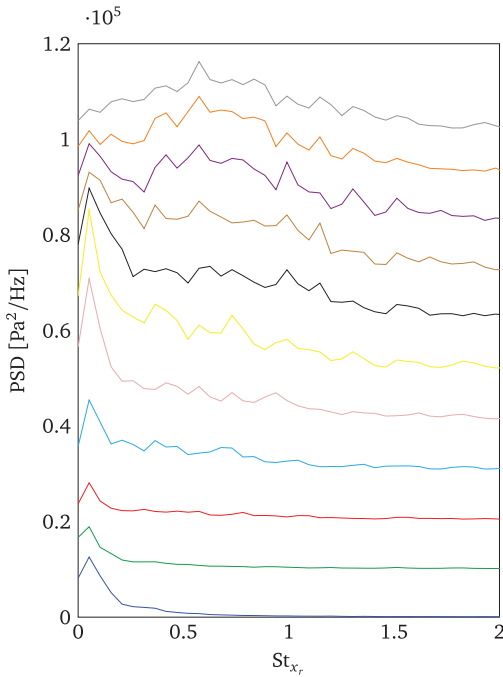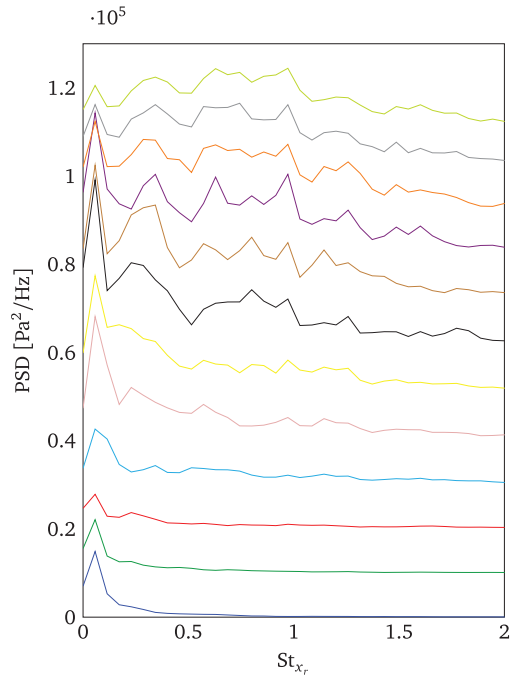
Fig. 13. PSD of the surface pressure from case A at 11 evenly spaced streamwise locations in successive order from bottom to top. Each spectrum is shifted along the ordinate by an integer times 10^4 in order to avoid clutter. Curves: ——, $x = 0.06x_r$; ——, $x = 0.18x_r$; ——, $x = 0.30x_r$; ——, $x = 0.43x_r$; ——, $x = 0.54x_r$; ——, $x = 0.67x_r$; ——, $x = 0.79x_r$; ——, $x = 0.91x_r$; ——, $x = 1.04x_r$; ——, $x = 1.16x_r$; ——, $x = 1.28x_r$.

Fig. 14. PSD of the surface pressure from case B at 12 evenly spaced streamwise locations in successive order from bottom to top. Each spectrum is shifted along the ordinate by an integer times 10^4 in order to avoid clutter. Curves: ——, $x = 0.06x_r$; ——, $x = 0.17x_r$; ——, $x = 0.28x_r$; ——, $x = 0.39x_r$; ——, $x = 0.50x_r$; ——, $x = 0.61x_r$; ——, $x = 0.72x_r$; ——, $x = 0.83x_r$; ——, $x = 0.95x_r$; ——, $x = 1.06x_r$; ——, $x = 1.16x_r$; ——, $x = 1.28x_r$.

a peak in the region of $0 < St_{x_r} < 0.2$. As the spectrum location moves downstream, the energy in the frequencies above $St_{x_r} = 0.2$ increases and in the most downstream spectra the highest energy is around $St_{x_r} = 0.6$, which corresponds well with the shedding frequency reported in the literature (for example Dandois et al., 2007; Hudy et al., 2003). The general behaviour for case A, i.e. most of the energy is in the low frequencies around the flapping frequency in the upstream part of the recirculation bubble and then a gradual shift in energy towards the shedding frequency moving further downstream towards the recirculation bubble, is consistent with the study performed by Hudy et al. (2003). However, for case A, the low frequencies remain relatively strong much further downstream compared to the study by Hudy et al. (2003).

For case B (Fig. 14), the spectra closest to the step is similar to case A. Also, further downstream there is the same gradual shift in energy towards higher frequencies with a centre in the region of $0.5 < St_{x_r} < 1.0$. In comparison to case A, there is no clear energy maximum at a frequency, but rather a range with the maximum energy. There is some indication of a peak around $St_{x_r} = 0.3$ between $0.7x_r < x < 1.1x_r$, but it is a bit uncertain.

Case C (Fig. 15) has two strong components of tonal character in its spectra. The first tone appears around $St_{x_r} = 0.3$ in the region between $0.6x_r < x < 1.2x_r$ and the second tone appears at approximately $St_{x_r} = 1.0$ in the vicinity of $x = 1.2x_r$. Neither case A nor case B has any clear tones in their spectra. Although, the peak at $St_{x_r} = 0.3$ is noticeable in case B. Apart from the tonal features, case C can be said to be qualitatively similar to case B.

The power spectra measured by Hudy et al. (2003) for fence flow have the discussed peak at the flapping frequency and the shedding frequency. Their spectra, however, are broadband with a maximum at a certain frequency rather than tonal peaks. As an example, see the shedding frequency peak in the most downstream spectra for case A (Fig. 13). Efimtsov et al. (2000) studied the surface pressure power spectra on the related case of backward-facing step flow. They found that the spectrum was essentially flat up until the shedding frequency and a sharp decrease in the energy above the shedding frequency. There was no peak to speak of at all. This behaviour was also found in the numerical study on the backward-facing step flow by Ji and Wang (2012). In contrast, the ACOUFAT study (Tougard, 1995) found a strong tonal peak at around $St_{x_r} = 0.5$ and also a clear but smaller peak at about $St_{x_r} = 0.8$.

Some trends in the spectra of both case C and the ACOUFAT study (Tougard, 1995) are illustrated in Fig. 16. Before interpreting the plots, two things should be noted about Fig. 16. First, the actual streamwise coordinates for the two curves inside each subfigure are different which means that two different tones appear on different locations in the streamwise direction. The relative spacing, however, is similar. Second, the values on the ordinate have been normalised by the maximum value in order to make a comparison easier. The purpose of Fig. 16 is to demonstrate the qualitative similarities rather than the differences that exists. In Fig. 16a, the most upstream of the subfigures, both curves show a strong tone; the frequency in the ACOUFAT case is $St_{x_r} = 0.5$ and for case C it is $St_{x_r} = 0.3$. Moving downstream to Fig. 16b there is an additional
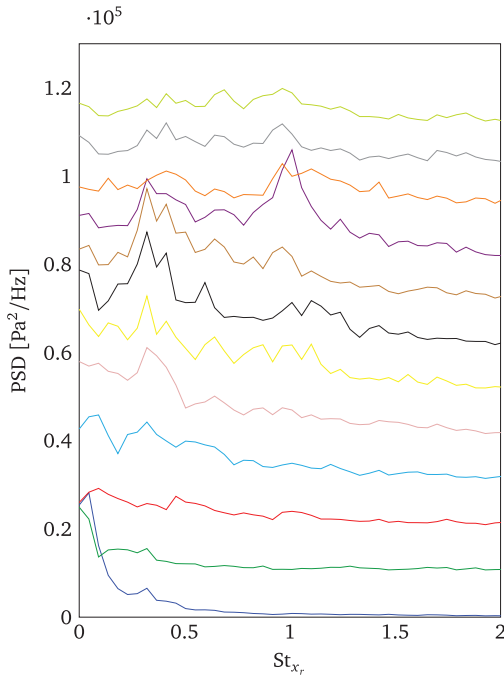
Fig. 15. PSD of the surface pressure from case C at 12 evenly spaced streamwise locations in successive order from bottom to top. Each spectrum is shifted along the ordinate by an integer times 10^4 in order to avoid clutter. Note that the curves corresponding to locations $x = 1.45x_r$ and $x = 1.59x_r$ are located downstream of the table edge placing them in mid-air rather than on the table surface. Curves: ——, $x = 0.07x_r$; ——, $x = 0.21x_r$; ——, $x = 0.35x_r$; ——, $x = 0.48x_r$; ——, $x = 0.62x_r$; ——, $x = 0.76x_r$; ——, $x = 0.90x_r$; ——, $x = 1.04x_r$; ——, $x = 1.18x_r$; ——, $x = 1.32x_r$; ——, $x = 1.45x_r$; ——, $x = 1.59x_r$.

Fig. 16. Normalised PSD of the surface pressure in (a) —— case C, $x = 0.80x_r$, —— ACOUFAT (Tougard, 1995), $x = 0.32x_r$, (b) —— case C, $x = 1.11x_r$, —— ACOUFAT (Tougard, 1995), $x = 0.55x_r$ and (c) —— case C, $x = 1.84x_r$, —— ACOUFAT (Tougard, 1995), $x = 0.92x_r$.

strong tone at $St_{x_r} = 1.0$ for case C. The ACOUFAT study also has a clear second tone, but it is weaker. In Fig. 16c, the tones have a more broadband distribution with a maximum near the first distinct tone.

In summary, the most similar configuration to the study by Hudy et al. (2003), case A, show qualitatively similar behaviour in the surface pressure power spectra. In the intermediate configuration, case B, the leading edge is added, and the power spectra has a possible weak tone at a similar frequency that is later found to be a strong tone in case C. Also the general broadband behaviour has also shifted towards case C. Finally, when more detail is added in the case C configuration, two tones appear in the spectra. These tones have different frequencies and appear at different streamwise locations than in the ACOUFAT study (Tougard, 1995), but there is also a strong similarity.

4.6. Autocorrelation

To investigate the time scales present in the surface pressure load, the autocorrelation was computed. Fig. 17 shows the autocorrelation map of the pressure time signal along the streamwise direction. The autocorrelation has been normalised by the square of the r.m.s. value of the signal in order to show the autocorrelation coefficient. In all three cases, there is a region closest to the fence where the time signal remains correlated several times longer than further downstream. This means that the long correlation time near the fence indicate that this region is dominated by
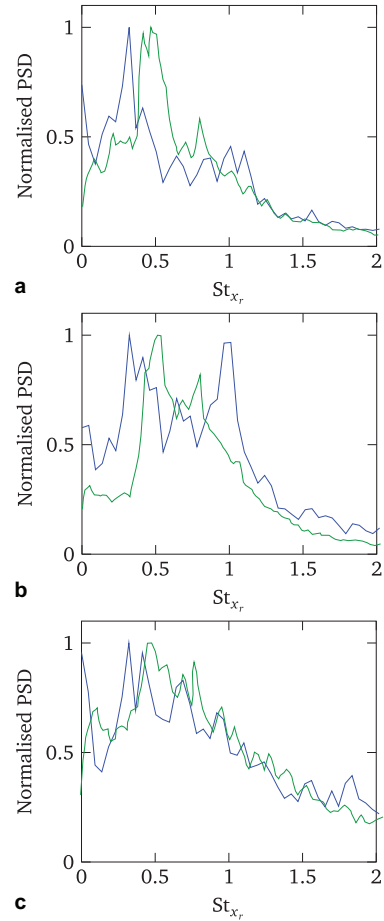
low-frequency disturbances and the opposite for the downstream region. The streamwise coordinate where the change-over occurs is approximately at $x = 0.2x_r$ for cases A and B, and $x = 0.15x_r$ for case C. The normalised correlation time $\tau U_0/x_r$ is somewhat longer closer to the fence in case B than in the other two cases. Both the correlation time length and the streamwise distribution are similar to that found by Hudy et al. (2003). In case C, however, both sides of the $\tau U_0/x_r = 0$ line has a dark diagonal line that is not found in neither cases A and B nor in the findings by Hudy et al. (2003).

4.7. Cross-correlation

Cross-correlation maps with correlation time on the ordinate and streamwise distance to the fence on the abscissa is shown in Figs. 18 and 19. The cross-correlation has been scaled in a similar way to the autocorrelation to obtain the cross-correlation coefficient. Fig. 18 uses a microphone close to reattachment as reference and Fig. 19 uses a microphone in the region where
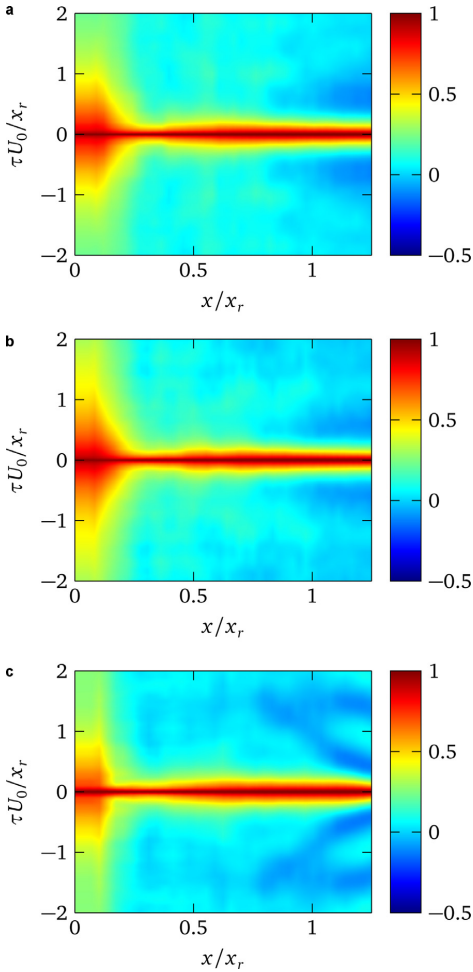
Fig. 17. Autocorrelation coefficient map. (a), (b) and (c) corresponds to cases A, B and C, respectively.

Fig. 18. Cross-correlation coefficient map for (a) case A with $x_{ref} = 1.01x_r$, (b) case B with $x_{ref} = 1.00x_r$ and (c) case C with $x_{ref} = 1.00x_r$, where x_{ref} is the streamwise location of the reference microphone.

the correlation time of the autocorrelation decreases rapidly (see Fig. 17).

In all three cross-correlation maps in Fig. 18, there is one main feature: a high correlation ridge with a negative slope. The time corresponding to the maximum value, or the peak of the ridge, gives the time delay for which the cross-correlation is the highest at each streamwise location. This time delay is the average time that it takes for pressure disturbances to travel to the reference microphone (at $x = x_r$). Therefore, the average convection speed of the dominant flow structures can be estimated by computing the slope of the ridge. A negative slope corresponds to a downstream motion. By fitting the ridge to a straight line through $x = x_r$, an average velocity of about $0.50U_\infty < U_c < 0.54U_\infty$ can be approximated from all three cases in Fig. 18. The present results are compared to different studies found in the literature in Table 2. The values determined from the present simulations are in line with the published literature. The ACOUFAT report (Tougard, 1995), which used the geometry that the present simulations are based
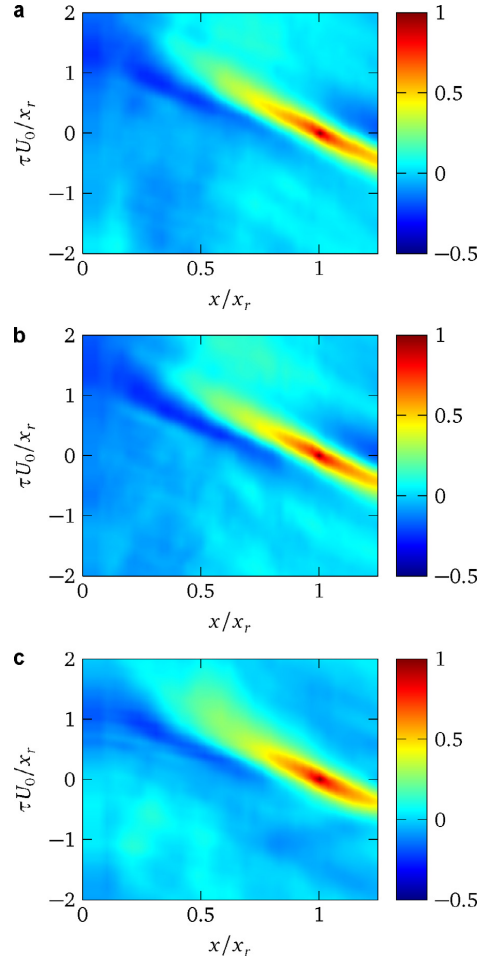
upon, gives an estimate value for this downstream velocity of just below $U_c = 0.4U_\infty$. However, this value appears to have been estimated using phase angle analysis which will give a different value for different frequencies. Phase angle analysis will be discussed in Section 4.9. In Fig. 18, the slope of the ridge appears to decrease slightly as x increases. This means that the velocity increases with x. This effect is strongest for case C. The same can be observed in the corresponding figure in the paper by Hudy et al. (2003). Heenan and Morrison (1998) also observed a slight increase in velocity as x increased. The three cross-correlation maps in Fig. 18 are overall very similar to the corresponding figure in the paper by Hudy et al. (2003).

Fig. 19 has its maximum at the location of the reference microphone, located at $x = 0.24x_r$ for cases A and C, and for $x = 0.28x_r$ for case B. From this maximum location, there are two lines visible. First, the stronger of the two lines has a negative slope and is mainly found downstream of the reference microphone. The slope is a bit smaller than in the corresponding slope in Fig. 18 indicating

Table 2

Average downstream convection velocity U_c downstream of $x \approx 0.5x_r$. BLE means blunt leading edge flow and BFS means backward-facing step flow. For cases where different U_c are reported for different frequencies, the value reported for the shedding frequency or high frequencies are used.

	Re_h	U_c	Geom.	Num./Exp.
Case A	$1.6 \cdot 10^6$	$0.50U_\infty$	Fence	Numerical
Case B	$1.6 \cdot 10^6$	$0.51U_\infty$	Fence	Numerical
Case C	$1.6 \cdot 10^6$	$0.54U_\infty$	Fence	Numerical
ACOUFAT (Tougard, 1995)	$1.6 \cdot 10^6$	$0.38U_\infty$	Fence	Experimental
Hudy et al. (2003)	$7.9 \cdot 10^3$	$0.57U_\infty$	Fence	Experimental
Cherry et al. (1984)	$3.2 \cdot 10^4$	$0.5U_\infty$	BLE	Experimental
Heenan and Morrison (1998)	$1.9 \cdot 10^5$	$0.5U_\infty < U_c < 0.6U_\infty$	BFS	Experimental
Lee and Sung (2001)	$3.3 \cdot 10^4$	$0.6U_\infty$	BFS	Experimental
Ji and Wang (2012)	$2.6 \cdot 10^4$	$0.37U_\infty$	BFS	Numerical

Table 3

Average upstream convection velocity U_c upstream of $x \approx 0.3x_r$. BFS means backward-facing step flow.

	Re_h	U_c	Geom.	Num./Exp.
Case A	$1.6 \cdot 10^6$	$0.10U_\infty$	Fence	Numerical
Case B	$1.6 \cdot 10^6$	$0.15U_\infty$	Fence	Numerical
Case C	$1.6 \cdot 10^6$	$0.13U_\infty$	Fence	Numerical
Hudy et al. (2003)	$7.9 \cdot 10^3$	$0.21U_\infty$	Fence	Experimental
Heenan and Morrison (1998)	$1.9 \cdot 10^5$	$0.20U_\infty$	BFS	Experimental
Ji and Wang (2012)	$2.6 \cdot 10^4$	$0.10U_\infty$	BFS	Numerical

increasing U_c of the downstream convection of the pressure disturbances in the upstream half of the recirculation bubble.

The second line in Fig. 19 is much less distinct than the previously discussed ones. It has a high positive slope intersecting the maximum location of each cross-correlation map and is indicated with a black dashed line. It is arguably strongest for case B. A positive slope indicates an upstream motion. The same line is found in the corresponding figure in the study by Hudy et al. (2003), where the line is also more distinct. The presence of upstream convection velocities in the upstream part of the recirculation bubble has been found experimentally for fence flow in the ACOUFAT study (Tougard, 1995) and by Hudy et al. (2003), experimentally for backward-facing step flow by Heenan and Morrison (1998) and numerically for backward-facing step flow by Ji and Wang (2012). However, the experimental studies on the backward-facing step flow by Farabee and Casarella (1984) and Lee and Sung (2001) found no evidence for upstream convection velocities. From the positive slopes in Fig. 19, the upstream convection velocity can be estimated. This estimate is given in Table 3 together with the reported values of other studies. While the ACOUFAT study (Tougard, 1995) reports that there is upstream convection of pressure disturbances, the report does not give any convection velocity and is therefore missing in Table 3.

4.8. Cross-correlation spectra

Campos et al. (1999) managed to improve the response prediction of a flexible surface panel structure mounted downstream of the fence by taking the cross-correlation spectrum into consideration. As their response prediction was remarkably good when the correct cross-correlations were used it is of interest to see how well the simulations capture this aspect. The cross-correlation spectra were computed using Welch's method and is normalised as $\tilde{S}_{pq}(f) = S_{pq}(f)/\sqrt{S_{pp}(f)S_{qq}(f)}$, where $S_{pq}(f)$ is the cross-correlation spectrum for microphones p and q.

Fig. 20 shows the cross-correlation spectra for six pairs of microphones. Fig. 20a–c depict pairs in the streamwise direction, while Fig. 20d–f depict pairs in the spanwise direction. The phase relation between all pairs is well captured with all simulated configurations, with the exception for case B and case C in Fig. 20a. The straight line in Fig. 20a from the ACOUFAT (Tougard, 1995)
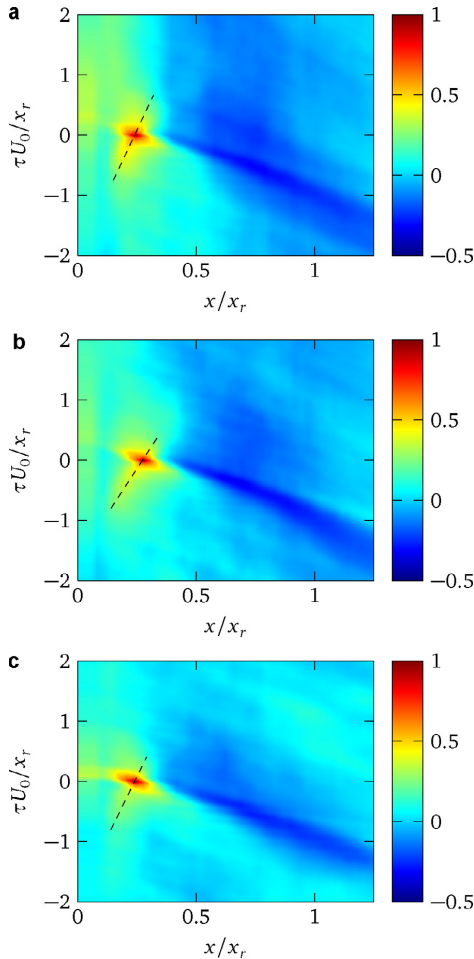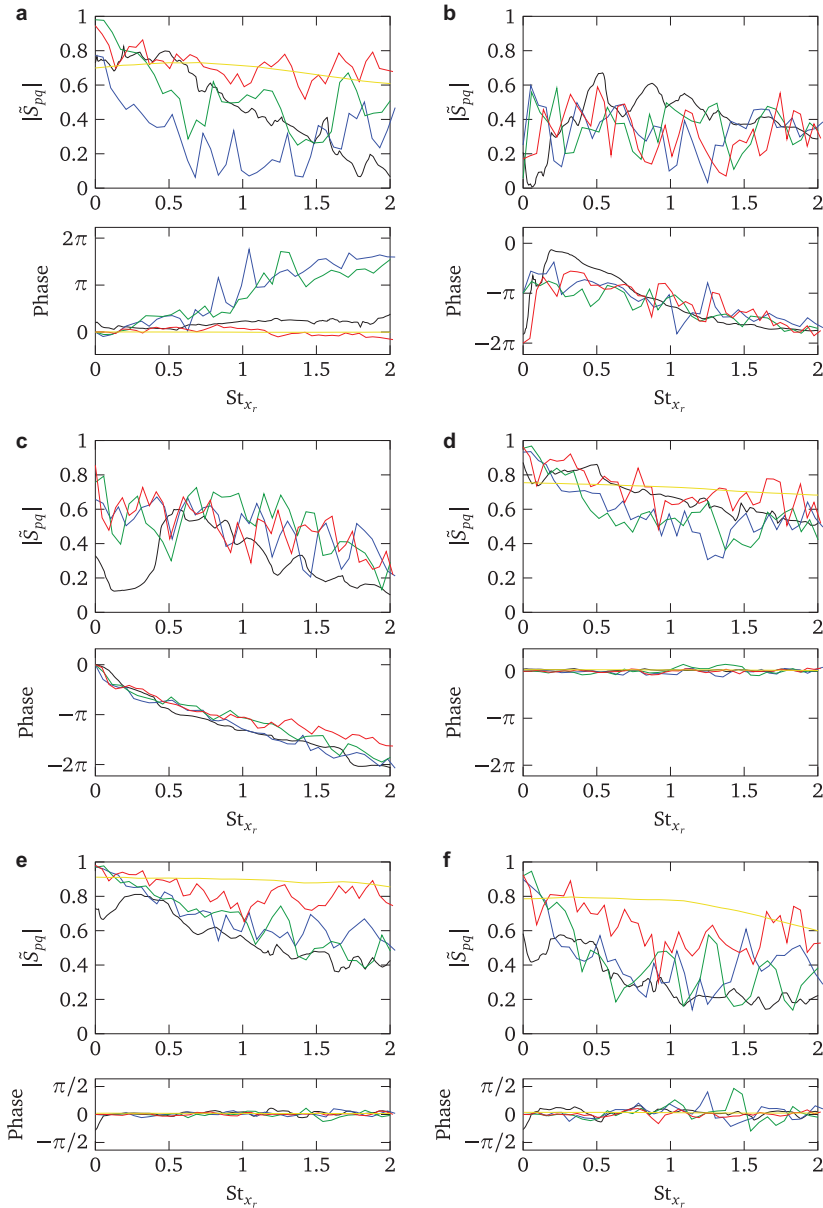
Fig. 19. Cross-correlation coefficient map for (a) case A with $x_{ref} = 0.24x_r$, (b) case B with $x_{ref} = 0.28x_r$ and (c) case C with $x_{ref} = 0.24x_r$, where x_{ref} is the streamwise location of the reference microphone.

a higher downstream velocity. The convection velocity U_c appears to be in the vicinity of $U_c = 0.6U_\infty$. However, the slope is less well defined compared to the corresponding ridge in Fig. 18 resulting in higher uncertainty. Heenan and Morrison (1998) also reports of

Fig. 20. Cross-correlation spectra for four pairs of microphones. Curves: ——, ACOUFAT (Tougard, 1995); ——, case A; ——, case B; ——, case C; ——, Campos et al. (1999). (a) is between microphones at $x = 0.12x_r$ and $x = 0.17x_r$, (b) is between microphones at $x = 0.22x_r$ and $x = 0.47x_r$, (c) is between microphones at $x = 0.65x_r$ and $x = 0.95x_r$. The pairs in (d), (e) and (f) are in the spanwise direction with the distance of $\Delta z = 0.75h$, $\Delta z = 0.75h$ and $\Delta z = 1.5h$, respectively. Both (e) and (f) are located at the streamwise position of $x = 0.17x_r$ while (d) is located at $x = 0.22x_r$.

measurements and case C indicate that the fluctuations are in phase between the two microphones. In contrast, the increase in phase with increasing frequency indicates that the pressure fluctuations are traveling upstream in cases A and B. This is believed to be related to a slight difference in the location and size of the secondary recirculation bubble closest to the fence.

The amplitude of the cross-spectrum varies slightly more. In Fig. 20b–f, all configurations have a similar behaviour as the ACOUFAT (Tougard, 1995) measurements, except for $St_{x_r} < 0.5$ in Fig. 20c. In Fig. 20a, the three configurations have rather different behaviour. As already stated, there are discrepancies in the phase relations as well. However, the region of poor prediction is limited

Table 4

Downstream convection velocity U_c in the vicinity of $x = x_r$ for three different frequencies.

St_{x_r}	0.4	0.6	0.8
Case A	$0.37U_\infty$	$0.43U_\infty$	$0.50U_\infty$
Case B	$0.35U_\infty$	$0.43U_\infty$	$0.51U_\infty$
Case C	$0.42U_\infty$	$0.49U_\infty$	$0.53U_\infty$

to the streamwise direction in the region of $x < 0.2x_r$. The other two streamwise pairs in Fig. 20b and c further downstream provides a much better agreement between the simulations and the ACOUFAT (Tougard, 1995) measurements.

A key point in the study by Campos et al. (1999) was that the fit between the 'semi-empirical' model produced cross-correlation spectra and the measured ones were mixed. Despite this, the response prediction of the downstream flexible panel structure was very good. The results from this 'semi-empirical' model have been included in four of the microphone pairs in Fig. 20 for comparison (the data for the remaining two microphone pairs are not available). In Fig. 20a, the decreasing correlation with frequency is not captured by Campos' model. Interestingly, case C produces similar results as Campos' model. In Fig. 20d, Campos model as well as the present simulations match the ACOUFAT (Tougard, 1995) measurements closely. In Fig. 20e and f, the present simulations are clearly closer to the ACOUFAT (Tougard, 1995) measurements than Campos' model.

Applying the simulated spectra and cross-correlation spectra produced in this work to a model of the flexible structure in order to generate a response prediction is out of scope for this work. However, it appears that the cross-correlation spectra produced by the simulations have a similar accuracy as the cross-correlation spectra produced 'semi-empirical' model produced by Campos et al. (1999), which is certainly encouraging.

4.9. Phase angle analysis

Figs. 21 and 22 shows the phase angle from the cross-spectrum densities against streamwise distance to the fence. Fig. 21 uses a microphone located near reattachment ($x = x_r$) as reference and the frequencies investigated are chosen to be centred on the shedding frequency $St_{x_r} = 0.6$. For all three cases, Fig. 21 shows essentially linear curves indicating that the pressure disturbances travels with a nearly constant velocity. The convection velocity U_c is then computed by

$$U_c = \frac{2\pi f}{\frac{\Delta\phi}{\Delta x}},$$

where ϕ is the phase angle in radians. The computed frequency dependent convection velocities given in Table 4 show that the higher frequencies travel at a higher velocity than lower frequencies. This is in-line with the experimental findings in both the ACOUFAT study (Tougard, 1995) and the study by Hudy et al. (2003).

Fig. 22 shows phase angle plots in the region where upstream convection of pressure disturbances was detected from Fig. 19. Around the reference microphone at around $x = 0.14x_r$ the blue squares and green circles form a negative slope for all cases. A negative slope indicates upstream motion. The red triangles representing a high frequency, $St_{x_r} = 1.8$, however, does not have a negative slope at all (with the possible exception for the short more or less flat section for case B around $x = 0.14x_r$). This indicates that the upstream motion is much stronger for the lower frequencies than for the higher frequencies. The computed upstream convection velocity for $St_{x_r} = 0.2$ is $U_c = 0.33U_\infty$, $U_c = 0.24U_\infty$ and $U_c = 0.25U_\infty$ for cases A, B and C, respectively. These values are significantly
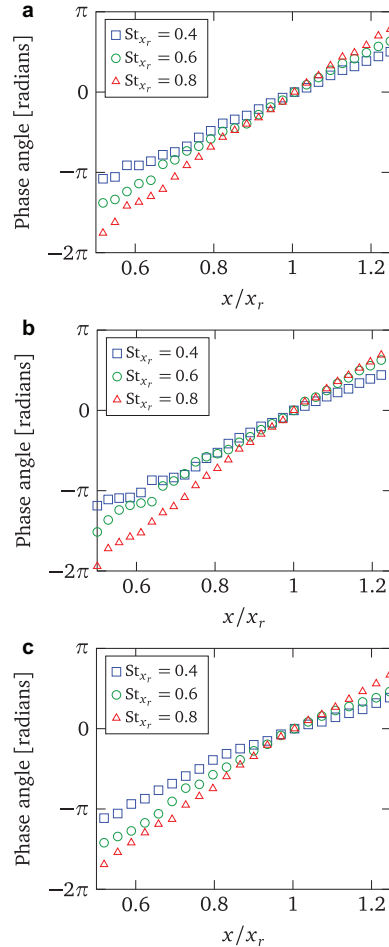

Fig. 21. Phase angle analysis. (a) is case A with $x = 1.01x_r$, (b) is case B with $x = 1.00x_r$, and (c) is case C with $x = 1.00x_r$.

higher than those found in Table 3. The reason for this is likely that the downstream convection for the same frequency is superimposed in the phase analysis and masks the upstream convection velocity. For $St_{x_r} = 0.6$ in Fig. 22a and for $St_{x_r} = 0.2$ in Fig. 22b, there is a sudden jump in the phase. Note that this jump is not just a simple lack of phase unwrapping as this would cause a phase shift of 2π.

4.10. Frequency–wave-number spectra

To further investigate the relations between frequency and convection velocity, frequency–wave-number maps were computed and the result is shown in Fig. 23. The map shows the magnitude of the estimated two-dimensional space-time Fourier transform of the autocorrelation of the microphone signals. The space dimension is in the streamwise direction, x. The spectra in Fig. 23 shows the energy content for different frequency–wave-number combinations.
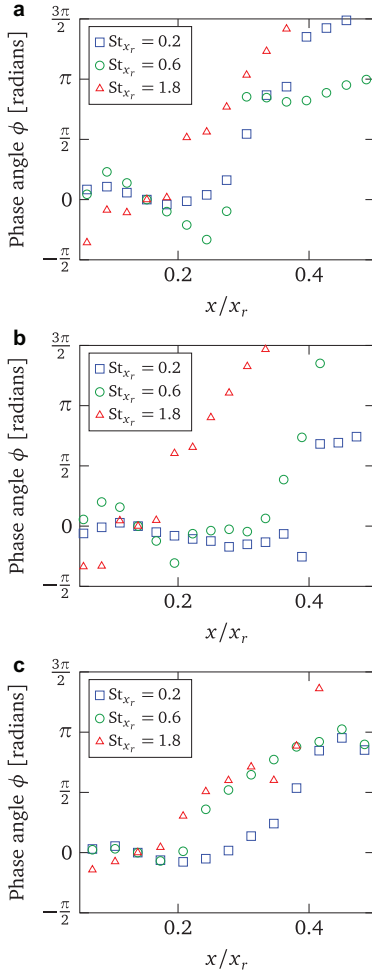
Fig. 22. Phase angle analysis. (a) is case A with $x = 0.15x_r$, (b) is case B with $x = 0.14x_r$ and (c) is case C with $x = 0.14x_r$. (For interpretation of the references to colour in this figure, the reader is referred to the web version of this article.)

Fig. 23. Frequency–wave-number map where (a), (b) and (c) correspond to cases A, B and C, respectively. The streamwise range of the microphones used is (a) $0 < x < 1.74x_r$, (b) $0 < x < 1.58x_r$ and (c) $0 < x < 1.97x_r$.

For all three spectra in Fig. 23, the main feature is the ridge in the right half of the plane ($k_x x_r > 0$). It has a high positive slope and is basically a straight line that nearly intersects the origin. This is the dominant downstream motion of pressure disturbances seen in Figs. 18, 19 and 21. As the velocity of a frequency–wave-number pair is the slope of a straight line to the point of the pair from the origin, the small offset to the origin results in different convection velocities as found in Table 4.

For negative wave-numbers which correspond to upstream motion, the three subfigures of Fig. 23 differ a bit. For case C (Fig. 23c), there appears to be a second, weaker, ridge with approximately the same (but negative) slope as the main ridge in the right half. The reason for this is likely related to the flow coming in from underneath the table. As seen in Section 4.1, there is separation in the flow coming from underneath the table close to the downstream edge of the table. This causes the flow to move upstream of the general flow direction in this region. Due to the
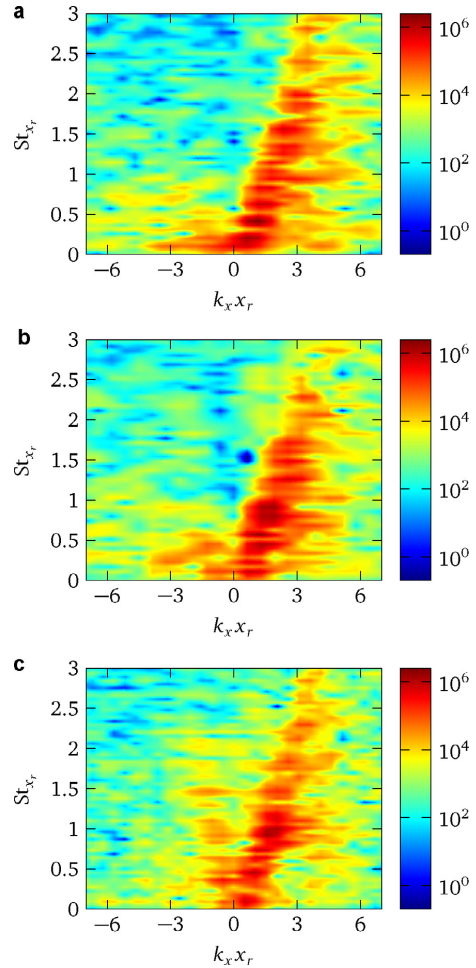
geometry in the other two configurations, this phenomenon does not, and cannot, appear in those configurations. For low frequencies ($St_{x_r} < 1$), cases A and B still have significant energy in the left half with negative wave-numbers. This appears to be the case for case C as well, but it is masked by the aforementioned second ridge. For case A, the energy in the left half of Fig. 23a is highest at frequencies around the typical flapping frequency ($0.1 < St_{x_r} < 0.2$), while for case B the range is a bit wider ($0 < St_{x_r} < 0.5$). However, for both cases A and B, it is clear that upstream motions occur at low frequencies only while the downstream motions also occur at higher frequencies as well.

5. Conclusions

Surface pressure fluctuations downstream of an inclined fence are studied numerically for conditions realistic for the aircraft and aerospace industry ($Re_h = 1.6 \cdot 10^6$, $Ma_\infty = 0.7$). The main goal has been to assess the ability of detailed (LES) simulations to predict

acoustic loads. The set-up corresponds to the configuration in the ACOUFAT measurements (Tougard, 1995). Due to the lack of some input parameters and to check the consistency of the data with existing findings, the results have been compared to other more basic flow configurations (fence and backward-facing step flows) as well.

The cross-correlation spectra, which was found to be a crucial parameter for load prediction by Campos et al. (1999), are found to match the ACOUFAT measurements (Tougard, 1995) on a level similar to the semi-empirical model developed by Campos et al. (1999). Since the suggested method is not based on empirical coefficients, it offers larger flexibility and robustness than previous approaches. Furthermore, the present method should be much more capable to deal with stronger variations and higher complexity in the basic geometry than the model by Campos et al. (1999).

Geometrical details often need to be simplified in computations, either to reduce the computing costs or because the limited details available about a given set-up. A geometrical sensitivity study, involving three different geometrical configurations, revealed that the flow is sensitive to the amount of detail in the description of the geometry. This illustrates the demand for proper documentation of measurements when numerical simulations of the same set-ups are planned.

Despite the sensitivity in the absolute value of the recirculation zone length, x_r, (both to geometry and mesh density), this was found to be a useful scaling parameter. The $C_{p'}$ values are found to be closer to values produced by backward-facing step flows rather than standard fence flows.

The power spectra revealed significant differences between the three present configurations. Case A, the most similar to the result reported by Hudy et al. (2003), has low frequencies around the flapping frequency dominating in the upstream half and a broadband distribution with a peak at the shedding frequency near mean reattachment. On the other end, case C produces two distinct tones similar to those found in the ACOUFAT project (Tougard, 1995). This demonstrates that the leading edge effects considered in cases B and C can have a strong influence on the pressure load spectrum.

The auto and cross-correlation figures, in agreement with both the ACOUFAT measurements (Tougard, 1995) and the results of Hudy et al. (2003), indicate the presence of two regions. In the upstream part there exists an upstream motion of pressure disturbances, whereas in the downstream part there is only downstream motion of these disturbances. Upstream motions of pressure fluctuations mainly occur at frequencies below the shedding frequency, while the downstream motion occurs also at frequencies above the shedding frequency. The upstream motion of the pressure disturbances appears to be strongest in case B.

In summary, the suggested approach has the ability to provide load predictions of the same accuracy as current semi-empirical models, without the need for empirical coefficients, thus offering larger flexibility. The results can be further improved by using more advanced turbulence models or if even finer mesh resolutions can be afforded.

Acknowledgments

References

Aider, J.-L., Danet, A., Lesieur, M., 2007. Large-eddy simulation applied to study the influence of upstream conditions on the time-dependant and averaged characteristics of a backward-facing step flow. J. Turbul. 8 (N51). doi:10.1080/14685240701701000.

Campos, L.M.B.C., Bourgine, A., Bonomi, B., 1999. Comparison of theory and experiment on aeroacoustic loads and deflections. J. Fluids Struct. 13 (1), 3–35. doi:10.1006/jfls.1998.0192.

Camussi, R., Guj, G., Ragni, A., 2006. Wall pressure fluctuations induced by turbulent boundary layers over surface discontinuities. J. Sound Vib. 294 (1–2), 177–204. doi:10.1016/j.jsv.2005.11.007.

Castro, I.P., Haque, A., 1987. The structure of a turbulent shear layer bounding a separation region. J. Fluid Mech. 179, 439–468. doi:10.1017/S0022112087001605.

Cherry, N.J., Hillier, R., Latour, M.E.M.P., 1984. Unsteady measurements in a separated and reattaching flow. J. Fluid Mech. 144, 13–46. doi:10.1017/S002211208400149X.

Cunningham, P.R., Langley, R.S., White, R.G., 2003. Dynamic response of doubly curved honeycomb sandwich panels to random acoustic excitation. Part 2: theoretical study. J. Sound Vib. 264 (3), 605–637. doi:10.1016/S0022-460X(02)01211-7.

Dandois, J., Garnier, E., Sagaut, P., 2007. Numerical simulation of active separation control by a synthetic jet. J. Fluid Mech. 574, 25–58. doi:10.1017/S0022112006003995.

Efimtsov, B., Kozlov, N., Kravchenko, S., Andersson, A., 2000. Wall pressure-fluctuation spectra at small backward-facing steps. In: Proceeding of 6th AIAA/CEAS Aeroacoustics Conferences Exhibit, Lahaina, Hawaii, AIAA-2000-2053 doi:10.2514/6.2000-2053.

Farabee, T.M., Casarella, M.J., 1984. Effects of surface irregularity on turbulent boundary layer wall pressure fluctuations. J. Vib. Acoust. 106 (3), 343–350. doi:10.1115/1.3269200.

Fureby, C., 1996. On subgrid scale modeling in large eddy simulations of compressible fluid flow. Phys. Fluids 8 (5), 1301–1311. doi:10.1063/1.868900.

Hasan, M.A.Z., 1992. The flow over a backward-facing step under controlled perturbation: laminar separation. J. Fluid Mech. 238, 73–96. doi:10.1017/S0022112092001642.

Heenan, A.F., Morrison, J.F., 1998. Passive control of pressure fluctuations generated by separated flow. AIAA J. 36, 1014–1022. doi:10.2514/2.474.

Hudy, L.M., Naguib, A.M., Humphreys, W.M., 2003. Wall-pressure-array measurements beneath a separating/reattaching flow region. Phys. Fluids 15 (3), 706–717. doi:10.1063/1.1540633.

Jasak, H., Weller, H., Gosman, A., 1999. High resolution NVD differencing scheme for arbitrarily unstructured meshes. Int. J. Numer. Methods Fluids 31 (2), 431–449. doi:10.1002/(SICI)1097-0363(19990930)31:2(431::AID-FLD884)3.0.CO;2-T.

Ji, M., Wang, M., 2012. Surface pressure fluctuations on steps immersed in turbulent boundary layers. J. Fluid Mech. 712, 471–504. doi:10.1017/jfm.2012.433.

Lee, I., Sung, H., 2001. Characteristics of wall pressure fluctuations in separated and reattaching flows over a backward-facing step: Part I. Time-mean statistics and cross-spectral analyses. Exp. Fluids 30 (3), 262–272. doi:10.1007/s003480000172.

di Mare, L., Jones, W., 2003. LES of turbulent flow past a swept fence. Int. J. Heat Fluid Flow 24 (4), 606–615. doi:10.1016/S0142-727X(03)00054-7.

Nilsson, J., Szász, R.-Z., Austrell, P.-E., Gutmark, E.J., 2015. Numerical simulation of a surface panel response to pressure loading from flow over a backward-facing step. J. Aircr. doi:10.2514/1.C033414. (in press)

OpenFOAM Foundation, 2012. OpenFOAM: The Open Source CFD Toolbox User Guide. Version 2.1.1, OpenFOAM Foundation.

Orellano, A., Wengle, H., 2001. POD analysis of coherent structures in forced turbulent flow over a fence. J. Turbul. 2 (N8). doi:10.1088/1468-5248/2/1/008.

Pascarelli, A., Marra, F., Piomelli, U., 2001. Large-eddy simulation of the flow over a wall-mounted fence. In: Geurts, B.J., Friedrich, R., Métais, O. (Eds.), Direct and Large-Eddy Simulation IV, Volume 8 of ERCOFTAC Series. Springer, Netherlands, pp. 419–426. doi:10.1007/978-94-017-1263-7_50.

Roshko, A., Lau, J.C., 1965. Some observations on transition and reattachment of a free shear layer in incompressible flow. Proc. Heat Transf. Fluid Mech. Inst. 1965, 157–167.

Ruderich, R., Fernholz, H.H., 1986. An experimental investigation of a turbulent shear flow with separation, reverse flow, and reattachment. J. Fluid Mech. 163, 283–322. doi:10.1017/S0022112086002306.

Spalding, D.B., 1961. A single formula for the "law of the wall". J. Appl. Mech. 28 (3), 455–458. doi:10.1115/1.3641728.

Tougard, D., 1995. Acoustic fatigue and related damage tolerance of advanced composite and metallic structures (ACOUFAT). In: Hernandez, J.M.M. (Ed.), Advances in Acoustics Technology. Wiley, Chichester, pp. 83–195.

Paper D

Three-dimensional aspects of fence flow

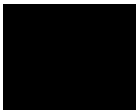Johan Nilsson[*], Robert-Zoltán Szász[†]

Abstract

This paper investigates three-dimensional aspects of the flow that are important for the surface pressure fluctuations downstream of an inclined fence. The investigation is based on numerical simulations that are performed at realistic Mach ($Ma_\infty = 0.7$) and Reynolds numbers ($Re_h = 1.6 \cdot 10^6$) for the aircraft industry. By using proper orthogonal decomposition, a key feature in the downstream surface pressure spectra is exposed that has a highly three-dimensional character and it is concluded that the phenomenon cannot be captured if only a segment of the fence flow is simulated using cyclic spanwise boundary conditions. In addition, a second phenomenon at very low frequencies that resembles the phenomenon known as wake meandering is also identified.

---

[*]Division of Structural Mechanics, Lund University, PO Box 118, SE-221 00, Lund, Sweden.
[†]Division of Fluid Mechanics, Lund University, PO Box 118, SE-221 00, Lund, Sweden.

Paper E

Numerical response simulation of a panel structure exposed to a numerically simulated load from separated flow

Johan Nilsson[*], Per-Erik Austrell[*], Robert-Zoltán Szász[†]

Abstract

Numerical simulations of the response of an aircraft skin surface panel exposed to a load induced from separated flow are performed. The panel response is simulated using finite element random response analysis. The load input to the response simulation is extracted from a computational fluid dynamics simulation. The flow conditions are realistic for aircraft operations and the test setup is relevant for acoustic fatigue, a problem for aircraft and aerospace industry. The numerical results are compared to existing measurements. Cross-correlation spectra of the load are well captured, but the load intensity is overestimated. Nevertheless, the panel response is found to be sensitive to the load cross-correlations. The predicted root-mean-square strains are within a factor two compared to existing measurements for all strain gauges but one. Thus, our predictions are at least of the same accuracy as the best expected accuracy of standard methods. However, the method suggested herein requires less empirical input.

[*]Division of Structural Mechanics, Lund University, PO Box 118, SE-221 00, Lund, Sweden.
[†]Division of Fluid Mechanics, Lund University, PO Box 118, SE-221 00, Lund, Sweden.